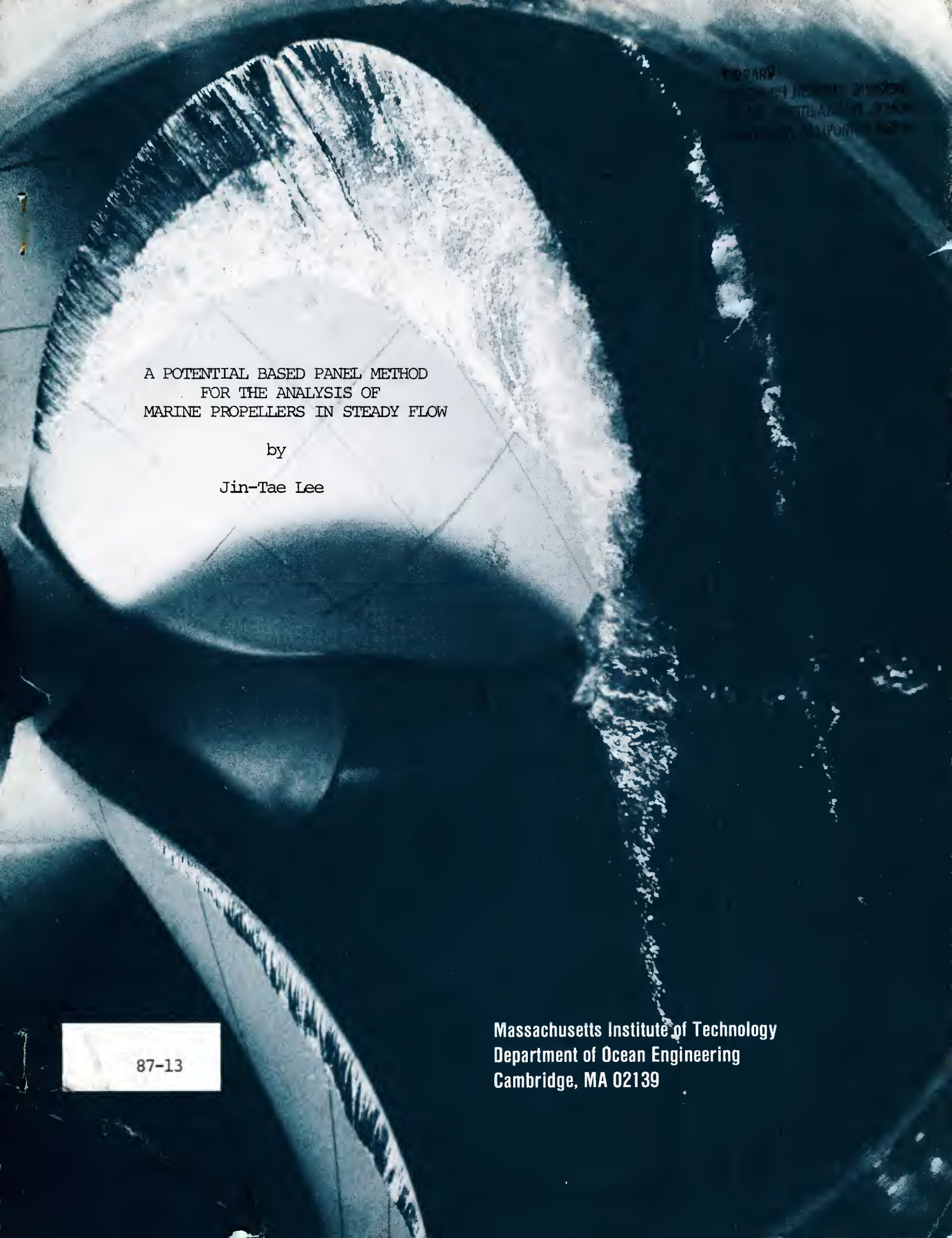


REPORT DOCUMENTATION PAGE

1a. REPORT SECURITY CLASSIFICATION Unclassified		1b. RESTRICTIVE MARKINGS	
2a. SECURITY CLASSIFICATION AUTHORITY		3. DISTRIBUTION/AVAILABILITY OF REPORT Approved for public release: Distribution unlimited:	
2b. DECLASSIFICATION/DOWNGRADING SCHEDULE			
4. PERFORMING ORGANIZATION REPORT NUMBER(S) MIT Dept. Of Ocean Eng. Report 87-13		5. MONITORING ORGANIZATION REPORT NUMBER(S)	
6a. NAME OF PERFORMING ORGANIZATION MIT Dept. of Ocean Eng.	6b. OFFICE SYMBOL (If applicable) 5-320	7a. NAME OF MONITORING ORGANIZATION Office of Naval Research	
6c. ADDRESS (City, State, and ZIP Code) Cambridge, MA 02139		7b. ADDRESS (City, State, and ZIP Code) 800 N. Quincy St. Arlington, VA 22217	
8a. NAME OF FUNDING SPONSORING ORGANIZATION Office of Naval Research	8b. OFFICE SYMBOL (If applicable)	9. PROCUREMENT INSTRUMENT IDENTIFICATION NUMBER N00014-82-K-0198	
8c. ADDRESS (City, State, and ZIP Code) 800 N. Quincy St Arlington, VA 22217		10. SOURCE OF FUNDING NUMBERS	
		PROGRAM ELEMENT NO.	PROJECT NO.
		TASK NO.	WORK UNIT ACCESSION NO.
11. TITLE (Include Security Classification) A Potential Based Panel Method for the Analysis of Marine Propellers in Steady Flow			
12. PERSONAL AUTHOR(S) Jin-Tae Lee			
13a. TYPE OF REPORT Technical Report	13b. TIME COVERED FROM _____ TO _____	14. DATE OF REPORT (Year, Month, Day) July 1987	15. PAGE COUNT 150
16. SUPPLEMENTARY NOTATION			
17. COSATI CODES		18. SUBJECT TERMS (Continue on reverse if necessary and identify by block number)	
FIELD	GROUP		
19. ABSTRACT (Continue on reverse if necessary and identify by block number) A surface panel method suitable for the analysis of marine propellers is developed and applied to various geometries to demonstrate its effectiveness. A reliable pressure distribution around a marine propeller, especially near the leading edge of the blade, is obtained. Hub effects are naturally included by distributing panels on the hub surface. Detailed study of the flows at the trailing edge near the tip suggests a pressure Kutta condition, which requires the pressures of the last panels at the trailing edge be equal. Due to the nonlinear aspect of the pressure Kutta condition, an iterative process is employed. An efficient approximation of the ultimate wake is achieved by replacing it with a sink disk at the beginning of the ultimate wake. The sample geometries include an ellipsoid at zero angle of attack, a circular planform wing, a rectangular planform wing with varying sweep angles, a wing-body configuration, a long axis-symmetric duct, and a marine propeller. Calculated pressure distributions around the wing-body configuration are in excellent agreement with the experimental data. Calculated thrust and torque for the propeller agree well with experimental results.			
20. DISTRIBUTION/AVAILABILITY OF ABSTRACT <input type="checkbox"/> UNCLASSIFIED/UNLIMITED <input checked="" type="checkbox"/> SAME AS RPT <input type="checkbox"/> DTIC USERS		21. ABSTRACT SECURITY CLASSIFICATION Unclassified	
22a. NAME OF RESPONSIBLE INDIVIDUAL Justin E. Kerwin		22b. TELEPHONE (Include Area Code) (617) 253-5139	22c. OFFICE SYMBOL MIT Room 5-320



A POTENTIAL BASED PANEL METHOD
FOR THE ANALYSIS OF
MARINE PROPELLERS IN STEADY FLOW

by

Jin-Tae Lee

87-13

Massachusetts Institute of Technology
Department of Ocean Engineering
Cambridge, MA 02139

Massachusetts Institute of Technology
Department of Ocean Engineering
Cambridge, Massachusetts 02139

Report 87-13

A Potential Based Panel Method
for the Analysis of
Marine Propellers in Steady Flow

by

Jin-Tae Lee

July 1987

©Massachusetts Institute of Technology, 1987

This research was sponsored by Office of Naval Research Accelerated Research Initiative (Special Focus) Program in Ship Hydrodynamics.

Office of Naval Research Contract No. N00014-82-K-0198. MIT OSP 91783.

A Potential Based Panel Method for the Analysis of Marine Propellers in Steady Flow

by

Jin-Tae Lee

This report is based on the author's thesis submitted to the Department of Ocean Engineering on July 14, 1987 in partial fulfillment of the requirements for the Degree of Doctor of Philosophy. The thesis advisor was Justin E. Kerwin, Professor of Naval Architecture.

Abstract

A surface panel method suitable for the analysis of marine propellers is developed and applied to various geometries to demonstrate its effectiveness. A reliable pressure distribution around a marine propeller, especially near the leading edge of the blade, is obtained. Hub effects are naturally included by distributing panels on the hub surface.

Detailed study of the flows at the trailing edge near the tip suggests a pressure Kutta condition, which requires the pressures of the last panels at the trailing edge be equal. Due to the nonlinear aspect of the pressure Kutta condition, an iterative process is employed. An efficient approximation of the ultimate wake is achieved by replacing it with a sink disk at the beginning of the ultimate wake.

The sample geometries include an ellipsoid at zero angle of attack, a circular planform wing, a rectangular planform wing with varying sweep angles, a wing-body configuration, a long axisymmetric duct, and a marine propeller. Calculated pressure distributions around the wing-body configuration are in excellent agreement with the experimental data. Calculated thrust and torque for the propeller agree well with experimental results.

Acknowledgements

I would like to express my sincere gratitude to my thesis advisor, Professor Justin E. Kerwin, for his constant support during my graduate studies. His insight during our discussion was invaluable. I extend my gratitude to my thesis committee members, Professor Paul D. Sclavounos and Professor Dick K.P. Yue, for their friendly comments.

Special thanks are extended to Dr. Spyros Kinnas for his friendship, talents and precious comments. All other propeller group members - Mr. Dean Lewis, Dr. Jean Luc Guermond, David Keenan, Wei-Zen Shih, William Coney, Ching-Yeh Hsin and others - made my stay at MIT challenging and also enjoyable. I will always remember the way how vague ideas become more concrete through discussions at the propeller group meeting. Neal Fine devoted his time unselfishly to proof-read my thesis. I thank Dr. David Greeley and Dr. James Uhlman for their interest and encouragements.

Financial support for the first part of my studies at MIT was provided by the Korean Science Foundation. Later support was provided by the Office of Naval Research. All are greatly acknowledged here.

I thank all the Korean students in O.E. dept., especially Chang-Ho and Moo-Hyun, for never letting me forget my mother tongue.

Finally, I would like to thank my wife, Eun-Hee, for her endless encouragement and support during my stay at MIT. A special thanks goes to my son, Sang-Jun, and to my parents for their continuous support throughout my education.

Contents

1	Introduction	12
2	Fundamentals of the panel methods	15
2.1	Introduction	15
2.2	Statement of the problem	16
2.3	Potential field formulation	19
2.4	Velocity Field Formulation	21
2.5	Comparison of the characteristics of the various panel methods	23
3	Numerical formulation	36
3.1	Blade geometry	37
3.2	Hub geometry	39
3.3	Geometry of the trailing wake	46
3.4	Approximation for the induced potential of the ultimate wake	47
3.5	Discretization of the singularity distribution.	52
3.6	Kutta condition	54
3.7	Linear system solution	59
3.8	Calculation of velocities, pressures, forces and moments.	61
4	Numerical results	64

I Wing problem	65
4.1 Ellipsoid at zero angle of attack	66
4.2 Circular wing at finite angle of attack	68
4.3 Rectangular wings with different sweep angles	81
4.4 Wing-body configuration	97
II Duct problem	112
4.5 Axisymmetric duct	113
III Propeller problem	118
4.6 Propeller performance analysis in steady flow	119
5 Conclusions	129
A Numerical formulation of the various panel methods for two-dimensional problems	135
A.1 Perturbation potential method	135
A.2 Total potential method	139
A.3 Mixed source and vortex method	140
A.4 Vortex method	143
B Equivalence of dipole and vorticity distribution	144
C Potential and velocities on the surface of an ellipsoid	148

List of Figures

2.1	Notation for a general body for the application of Green's theorem.	17
2.2	Panel arrangement of a typical foil section. (NACA 66 mod. + $a=0.8$ mean camber line, $t/c=0.04$, $f/c=0.02$)	26
2.3	Convergence characteristics of the perturbation potential distribution calculated by the perturbation potential method. (NACA 66 + $a=0.8$, $t/c=0.04$, $f/c=0.02$, $\alpha=1.5$ deg)	27
2.4	Convergence characteristics of the pressure distribution calculated by the perturbation potential method. (NACA 66 + $a=0.8$, $t/c=0.04$, $f/c=0.02$, $\alpha=1.5$ deg)	28
2.5	Convergence characteristics of the total potential distribution calcu- lated by the total potential method. (NACA 66 + $a=0.8$, $t/c=0.04$, $f/c=0.02$, $\alpha=1.5$ deg)	30
2.6	Convergence characteristics of the pressure distribution calculated by the total potential method. (NACA 66 + $a=0.8$, $t/c=0.04$, $f/c=0.02$, $\alpha=1.5$ deg)	31
2.7	Comparison of the pressure distributions by potential method and the velocity methods. (NACA 66 + $a=0.8$, $t/c=0.04$, $f/c=0.02$, $\alpha=1.5$ deg)	33
3.1	Propeller blade geometry notation.	38
3.2	Panel arrangement viewed from upstream for a three bladed propeller with a hub. ($N_c=40$, $M_r=10$, $N_u + N_b + N_d + N_t=39$, $M_\theta=8$)	40

3.3	Panel arrangement viewed from downstream for a three bladed propeller with a hub. ($N_c=40, M_r=10, N_u + N_b + N_d + N_t=39, M_\theta=8$)	41
3.4	Geometry notation of the hub.	42
3.5	Expanded plan view of the hub panel arrangement.	45
3.6	Radii of the trailing vortex lines. ($M_r=10, R_w=0.83, R_{wh}=0.1, X_{tw}=1.5, \delta_c=15$ deg.)	48
3.7	Far-field approximation of the ultimate wake.	50
3.8	Perturbation potential distribution for a circular cylinder at 90 degree angle of attack.	56
3.9	Pressure distribution for a circular cylinder at 90 degree angle of attack.	57
3.10	Magnified flow at the trailing edge near the tip.	58
3.11	Summation of the velocity component.	62
4.1	Coordinate system and panel arrangement of the ellipsoid.	67
4.2	Chordwise potential distribution of the ellipsoid. ($a=b=1, c=0.1$)	69
4.3	Chordwise distribution of the u-velocity component of the ellipsoid. ($a=b=1, c=0.1$)	70
4.4	Spanwise potential distribution of the ellipsoid. ($a=b=1, c=0.1$)	71
4.5	Spanwise distribution of the v-velocity component of the ellipsoid. ($a=b=1, c=0.1$)	72
4.6	Chordwise pressure distribution of the ellipsoid. ($a=b=1, c=0.1$)	73
4.7	Chordwise pressure distribution of the ellipsoid. ($a=b=1, c=0.1$)	74
4.8	Effect of the chordwise number of panels on the circulation distribution of the circular wing. ($t/c=0.01, \alpha=5.73$ deg.)	76
4.9	Effect of the spanwise number of panels on the circulation distribution of the circular wing. ($t/c=0.01, \alpha=5.73$ deg.)	77

4.10 Effect of the pressure Kutta condition on the chordwise distribution of the pressure difference of the circular wing. ($t/c=0.01$, $\alpha=5.73$ deg., $r/R=0.916$)	78
4.11 Effect of the pressure Kutta condition on the chordwise distribution of the pressure difference of the circular wing. ($t/c=0.05$, $\alpha=5.73$ deg., $r/R=0.916$)	79
4.12 Magnified flow at the trailing edge near the tip.	80
4.13 Thickness effect on the radial circulation distribution of the circular wing. ($\alpha=5.73$ deg.)	82
4.14 Chordwise distribution of the pressure difference of the circular wing at $r/R=0.098$	83
4.15 Chordwise distribution of the pressure difference of the circular wing at $r/R=0.693$	84
4.16 Chordwise distribution of the pressure difference of the circular wing at $r/R=0.916$	85
4.17 Chordwise distribution of the pressure difference of the circular wing at $r/R=0.977$	86
4.18 Panel arrangements of the rectangular wings with -45, 0, and +45 degree sweep angles. (Aspect ratio=5.9, $t/c=0.01$, 0.05 and 0.12, $\alpha=8$ deg.)	88
4.19 Effect of the chordwise number of panels on the circulation distribution of the unswept rectangular wing. (Aspect ratio=5.9, $t/c=0.12$, $\alpha=8$ deg.)	89
4.20 Effect of the spanwise number of panels on the circulation distribution of the unswept rectangular wing. (Aspect ratio=5.9, $t/c=0.12$, $\alpha=8$ deg.)	90
4.21 Effect of the thickness on the spanwise circulation of the unswept wing. (Aspect ratio=5.9, $\alpha=8$ deg.)	91

4.22 Chordwise distribution of the pressure difference of the unswept rectangular wing. (Aspect ratio=5.9, $t/c=0.05$, $\alpha=8$ deg.)	93
4.23 Chordwise distribution of the pressure difference of the unswept rectangular wing. (Aspect ratio=5.9, $t/c=0.12$, $\alpha=8$ deg.)	94
4.24 Spanwise vorticity distribution of the unswept rectangular wing. (Aspect ratio=5.9, $t/c=0.05$, $\alpha=8$ deg.)	95
4.25 Spanwise vorticity distribution of the unswept rectangular wing. (Aspect ratio=5.9, $t/c=0.12$, $\alpha=8$ deg.)	96
4.26 Radial circulation distribution for the -45 degree swept wing. (Aspect ratio=5.9, $\alpha=8$ deg.)	98
4.27 Radial circulation distribution for the +45 degree swept wing. (Aspect ratio=5.9, $\alpha=8$ deg.)	99
4.28 Spanwise local lift coefficient distribution for the unswept rectangular wing. (Aspect ratio=5.9, $t/c=0.12$, $\alpha=8$ deg.)	100
4.29 Spanwise local lift coefficient distribution for the +20 degree swept rectangular wing. (Aspect ratio=5.9, $t/c=0.12$, $\alpha=8$ deg.)	101
4.30 RAE wing-body configuration.	103
4.31 Panel arrangement of the half wing-body configuration.	104
4.32 Wing-body chordwise pressure distribution at $r/R=0.25$	105
4.33 Wing-body chordwise pressure distribution at $r/R=0.60$	106
4.34 Wing-body chordwise pressure distribution at $r/R=0.925$	107
4.35 Fuselage pressure distribution in the presence of wing. ($\varphi=\pm 15$ deg.)	109
4.36 Fuselage pressure distribution in the presence of wing. ($\varphi=\pm 45$ deg.)	110
4.37 Fuselage pressure distribution in the presence of wing. ($\varphi=\pm 75$ deg.)	111
4.38 Panel arrangement for an axisymmetric duct formed from a NACA 0010 section with a chord/mean radius ratio of ten. ($N_c=36$, $M_\theta=18$)	114

4.39 Pressure distribution for the axisymmetric duct with the present method with different number of panels.	116
4.40 Pressure distribution for the axisymmetric duct by different panel method as presented by Miranda [19].	117
4.41 Panel arrangement of one third of the propeller.	120
4.42 Panel arrangement for the wake.	122
4.43 Measured and calculated open water characteristics of NSRDC propeller 4118.	123
4.44 Perturbation potential distribution on the blade for NSRDC propeller 4118 operating at an advance coefficient $J=0.833$	124
4.45 Computed chordwise pressure distributions for NSRDC propeller 4118 operating at an advance coefficient $J=0.833$	125
A.1 Nomenclature of the potential methods for a two-dimensional foil . . .	137
A.2 Nomenclature of the velocity method for a two-dimensional foil.	142
B.1 Notation for a general surface.	145

List of Tables

2.1	Effect of the number of chordwise panels on computed lift and drag coefficient for the two-dimensional foil section. (NACA 66 mod. + $a=0.8$, $t/c=0.04$, $f/c=0.02$, $\alpha=1.5$ deg.)	32
3.1	Comparison of the induced potential due to the helical dipole strips and that due to the sink disk on the capping surface.	51
3.2	Comparison of the computing times of the influence function calculation and the matrix solver.	61
4.1	Effect of the number of panels on the lift and drag coefficients of the unswept rectangular wing. (Aspect ratio=5.9, $t/c=0.12$, $\alpha=8$ deg.) . .	92

Chapter 1

Introduction

Calculation of the pressure distribution around a marine propeller is a fundamental goal of many naval architects, yet a successful calculation of a reliable pressure distribution, especially near the leading edge and the blade tip, has not been reported. Not only should the thrust and the torque, which are calculated by the integration of the pressure distribution on the blade surface, be accurate, but the local minimum pressure at the leading edge of the blade should also be accurate to calculate cavitation inception and extent. Moreover, the locations of the local stagnation point and the minimum pressure point at the leading edge of the blade are essential inputs to the calculation of the boundary layer on the blade surface.

Most of the design and analysis of marine propellers rely heavily on lifting surface theory. Many lifting surface codes, which use a discrete vortex/source line representation of the blade on the mean camber surface, have been developed and used in the prediction of the steady/unsteady performance of marine propellers [14],[5]. As a consequence of the linear superposition of the thickness and the lifting problem in lifting surface theory, the prediction of the pressure distribution at the leading edge is not valid. Lighthill's correction may be applied to the local flow around the leading edge, however the validity is questionable for general three-dimensional flows. Moreover the complete exclusion of the hub in the numerical model of the lifting surface

theory has been questioned. Recent research on the effect of the hub on the performance of a propeller by Wang [23] showed that the effect could be significant in those propellers with a large hub radius or a small number of blades. These difficulties can be resolved naturally by adopting a surface panel method and distributing panels on the exact propeller surface including the hub surface. This becomes possible as high speed computers, with large capacity, become more commonly available.

Many kinds of panel methods have been in use for aerodynamic/hydrodynamic applications since Hess [8] proposed the surface source method. Although all the properly formulated panel methods are exact in the sense that the numerical solutions converge to the common solution as the number of panels is increased, this does not imply that all the panel methods are equally successful. Indeed, vast differences exist with respect to the prediction accuracy versus computational effort and the reliability for extreme geometries.

In the present paper, the characteristics of the various panel methods are reviewed and compared. As a result, a low order panel method based on the perturbation potential is chosen because of its robustness with respect to extreme geometries, and its relatively smaller computational effort.

Extreme geometry of the blade of marine propeller had prevented the surface panel method from being applied to the marine propellers. To the author's knowledge, only two attempts have been made to apply the panel method. Hess [9] extended his surface source method to this problem. But the surface source method suffers as the thickness of the blade becomes small, and the results toward the thin blade tip become questionable. Koyama et. al. [15] applied a Morino type low order panel method to marine propellers. But his pressure distribution near the tip showed a spurious positive loading at the trailing edge. This is due to the failure of the Morino's Kutta condition which does not account for the three dimensional cross flow effects. In the present work, extensive attention is given to the three dimensional trailing edge flow.

As a result, a pressure Kutta condition, which requires the pressures of the last panels at the trailing edge be equal, is suggested. Due to the nonlinear aspect of the pressure Kutta condition, an iterative solution procedure is employed.

Numerical calculation is performed for various geometries using the selected panel method with the pressure Kutta condition. The examples selected in the present work include an ellipsoid at zero angle of attack, a circular planform wing with varying thickness, a rectangular planform wing with different sweep angles, a wing-body configuration, a long axisymmetric duct, and a marine propeller.

Chapter 2

Fundamentals of the panel methods

2.1 Introduction

Panel methods have been in use for certain aerodynamic/hydrodynamic applications since Hess [8] proposed the surface source method in 1964. Since then, various other formulations have appeared which offer advantages in terms of accuracy, computational efficiency or versatility. Although all the properly formulated panel methods are exact in the sense that the numerical solutions converge to the common solution as the number of panels is increased, this does not imply that all the panel methods are equally successful. Indeed, vast differences exist with respect to the prediction accuracy versus computational effort, reliability and simplicity.

In this chapter, the basic mathematical theory behind the various panel methods is reviewed and the characteristics of each method are compared in order to determine the most suitable method for the analysis of marine propellers. The common basis of the apparently different panel methods will then be evident, suggesting the following grouping of the panel methods.

- Potential field formulation.
 - Perturbation potential method.
 - Total potential method.

- Velocity field formulation.
 - Mixed source and dipole method
 - Dipole method. (Equivalently, vorticity method)
 - Source based method.

2.2 Statement of the problem

Consider a closed three dimensional domain V with boundary S , the unit normal vector \vec{n} to S being oriented into V , as shown in Figure 2.1. The boundary S is composed of the body surface S_B , the wake surface S_W , and the outer control surface S_∞ surrounding the body and wake surface. The body is subject to the inflow velocity \vec{U}_∞ . With the assumptions that the fluid in V is incompressible, inviscid, and irrotational, there exists a perturbation velocity potential ϕ which satisfies the Laplace equation,

$$\nabla^2 \phi = 0. \quad (2.1)$$

A boundary value problem can be constructed by specifying boundary conditions on the boundary S as follows:

- The kinematic boundary condition should be satisfied on the solid body surface S_B ,

$$\frac{\partial \phi}{\partial n} = -\vec{U}_\infty \cdot \vec{n}. \quad (2.2)$$

- The wake surface S_W is assumed to have zero thickness. The normal velocity jump and the pressure jump across S_W is zero, while a jump in the potential is allowed.

$$(\Delta p)_{on S_W} = p^+ - p^- = 0, \quad (2.3)$$

$$(\Delta \frac{\partial \phi}{\partial n})_{on S_W} = (\frac{\partial \phi}{\partial n})^+ - (\frac{\partial \phi}{\partial n})^- = 0. \quad (2.4)$$

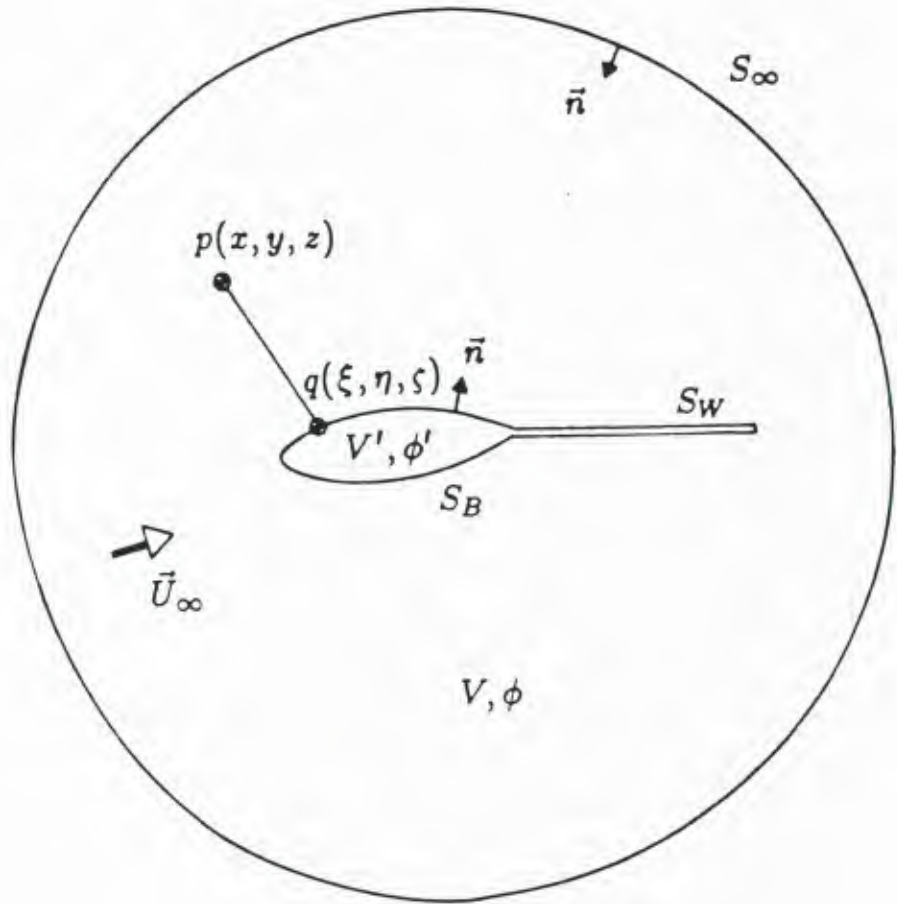


Figure 2.1: Notation for a general body for the application of Green's theorem.

For the steady lifting problem, the potential jump across the wake surface is the same as the circulation around the body, and is constant in the streamwise direction on S_w .

$$(\Delta\phi)_{on S_w} = \phi^+ - \phi^- = \Gamma. \quad (2.5)$$

- A Kutta condition is required at the trailing edge to uniquely specify the circulation. In its most general form, it states that the flow velocity at the trailing edge remains bounded: i.e.,

$$|\nabla\phi|_{T.E.} < \infty. \quad (2.6)$$

- On the outer control surface S_∞ , the perturbation velocity due to the body should vanish in the limit where this surface is an infinite distance from the body.

$$\nabla\phi \rightarrow 0, \text{ as } S_\infty \rightarrow \infty \quad (2.7)$$

According to Lamb [16], this boundary value problem for the velocity potential outside the body surface can be transformed into an integral equation, upon consideration of a fictitious fluid in V' , which is the domain internal to the body surface S_B . Thus for the field point p in V

$$\begin{aligned} 4\pi\phi(p) &= \iint_{S_B} \left[(\phi(q) - \phi'(q)) \frac{\partial}{\partial n_q} \frac{1}{R(p; q)} - \left(\frac{\partial\phi(q)}{\partial n_q} - \frac{\partial\phi'(q)}{\partial n_q} \right) \frac{1}{R(p; q)} \right] dS \\ &\quad + \iint_{S_w} \Delta\phi(q) \frac{\partial}{\partial n_q} \frac{1}{R(p; q)} dS, \end{aligned} \quad (2.8)$$

- where ϕ = perturbation velocity potential in V ,
 ϕ' = perturbation velocity potential in V' ,
 $p(x, y, z)$ = field point where induced potential is calculated,
 $q(\xi, \eta, \varsigma)$ = source point where singularity is located,
 $R(p; q)$ = distance between point p and q ,
 $= \sqrt{(x - \xi)^2 + (y - \eta)^2 + (z - \varsigma)^2}$,

$$\frac{\partial}{\partial n_q} = \text{normal derivative with respect to the point } q.$$

This equation may be regarded as a representation of the velocity potential in terms of a normal dipole distribution of strength $(\phi - \phi')$ on the body surface S_B , a source distribution of strength $(\frac{\partial \phi}{\partial n} - \frac{\partial \phi'}{\partial n})$ on S_B , and a normal dipole distribution of strength $\Delta\phi$ on the wake surface S_W .

Since the fictitious fluid inside S_B does not have physical meaning, we can choose the internal velocity potential ϕ' to suit our convenience. Thus, by choosing an appropriate ϕ' in Equation 2.8, we can formulate various panel methods which use different sets of singularities.

2.3 Potential field formulation

If we choose the fictitious potential as $\phi' = 0$ on S_B , Equation 2.8 for the field point p on the body surface S_B becomes

$$2\pi\phi(p) = \iint_{S_B} \left[\phi(q) \frac{\partial}{\partial n_q} \frac{1}{R(p; q)} - \frac{\partial\phi(q)}{\partial n_q} \frac{1}{R(p; q)} \right] dS + \iint_{S_W} \Delta\phi(q) \frac{\partial}{\partial n_q} \frac{1}{R(p; q)} dS. \quad (2.9)$$

Here the surface integral on S_B must be defined to exclude the immediate vicinity of the singular point. By choosing the internal potential on S_B as $\phi' = 0$, the internal flow can be shown to be an undisturbed flow of $\Phi' = \phi_\infty$, where the total internal velocity potential is defined as $\Phi' = \phi_\infty + \phi'$.

Because $\frac{\partial\phi}{\partial n}$ is known on S_B from the boundary condition (Equation 2.2), Equation 2.9 is a Fredholm integral equation of the second kind for the dipole strength ϕ , which is also the potential value on the body surface S_B . The potential jump across the wake surface can be set equal to the difference between the potential values of the upper and lower surfaces at the trailing edge, which replaces the Kutta condition. Discretization of Equation 2.9 will lead to a linear system of equations for the

unknown ϕ . The surface velocity, hence the pressure, on S_B can be calculated by a numerical differentiation of the potential distribution. This form of panel method was introduced by Morino [20], and adopted in the present paper. We will refer to this as Morino's method or the perturbation potential method.

If there exists an inflow velocity potential, ϕ_∞ , such that $\nabla\phi_\infty = \vec{U}_\infty$, we can formulate another form of the panel method by choosing the internal potential in Equation 2.8 as a negative of the inflow velocity potential, i.e., $\phi' = -\phi_\infty$. The source strength in Equation 2.8 becomes zero because of the boundary condition (Equation 2.2), while the dipole strength, which is the difference between ϕ and ϕ' , becomes the total potential,

$$\phi - \phi' = \phi + \phi_\infty \equiv \Phi. \quad (2.10)$$

As the point p approaches the body surface S_B , the contribution from the immediate surface S_ϵ on S_B in the first term of Equation 2.8 is

$$\lim_{S_\epsilon \rightarrow 0} \lim_{p \rightarrow S_B} \iint_{S_\epsilon} (\phi - \phi') \frac{\partial}{\partial n_q} \frac{1}{R(p; q)} dS = 2\pi(\phi - \phi') = 2\pi \Phi. \quad (2.11)$$

The resulting equation is

$$\begin{aligned} 2\pi \Phi(p) &= 4\pi \phi_\infty(p) + \iint_{S_B} \Phi(q) \frac{\partial}{\partial n_q} \frac{1}{R(p; q)} dS \\ &\quad + \iint_{S_W} \Delta\Phi(q) \frac{\partial}{\partial n_q} \frac{1}{R(p; q)} dS. \end{aligned} \quad (2.12)$$

This equation can be regarded as a representation of the total velocity potential in terms of a normal dipole distribution only on the body surface S_B and the wake surface S_W . Given the inflow velocity potential values, this is also a Fredholm integral equation of the second kind for the total potential Φ . Discretization of this equation gives another form of panel method, which we will refer to as the total potential method.

2.4 Velocity Field Formulation

Instead of forming an integral equation in the potential field, we can alternatively construct one in the velocity field. Taking the normal derivative of Equation 2.8 with respect to the field point p , the resulting equation, when the field point p is on S_B , is

$$\begin{aligned} 4\pi \frac{\partial \phi(p)}{\partial n_p} &= 2\pi \sigma(p) + \iint_{S_B} \sigma(q) \frac{\partial}{\partial n_p} \left(\frac{-1}{R(p; q)} \right) dS + \iint_{S_B} \mu(q) \frac{\partial^2}{\partial n_p \partial n_q} \frac{1}{R(p; q)} dS \\ &\quad + \iint_{S_W} \Delta \phi(q) \frac{\partial^2}{\partial n_p \partial n_q} \frac{1}{R(p; q)} dS, \end{aligned} \quad (2.13)$$

where $\sigma = \frac{\partial \phi}{\partial n} - \frac{\partial \phi'}{\partial n}$ and $\mu = \phi - \phi'$.

It can be shown that a dipole distribution on a closed body surface is equivalent to a vorticity distribution with strength $\vec{\gamma}$, which is calculated as a vector product of the local surface gradient of the dipole strength and the normal vector. (see Appendix B) Thus we can alternatively write Equation 2.13 as

$$\begin{aligned} 4\pi \frac{\partial \phi(p)}{\partial n_p} &= 2\pi \sigma(p) + \iint_{S_B} \sigma(q) \frac{\partial}{\partial n_q} \left(\frac{-1}{R} \right) dS + \iint_{S_B} \vec{n}_p \cdot \vec{\gamma}(q) \times \nabla_p \frac{-1}{R} dS \\ &\quad + \iint_{S_W} \vec{n}_p \cdot \vec{\gamma}(q) \times \nabla_p \frac{-1}{R} dS, \end{aligned} \quad (2.14)$$

where $\vec{\gamma} = \vec{n}_q \times \nabla_{2-d}(\phi - \phi')$.

Here again, by choosing different values for the internal potential ϕ' , we can express the normal velocity on S_B in terms of different sets of singularities.

If we choose the internal potential in Equation 2.13 as $\phi' = 0$, it can be shown that $\frac{\partial \phi'}{\partial n_p} = 0$ on S_B . Then,

$$\begin{aligned} 2\pi \frac{\partial \phi(p)}{\partial n_p} &= \iint_{S_B} \sigma(q) \frac{\partial}{\partial n_p} \left(\frac{-1}{R} \right) dS + \iint_{S_B} \mu(q) \frac{\partial^2}{\partial n_p \partial n_q} \frac{1}{R} dS \\ &\quad + \iint_{S_W} \Delta \phi(q) \frac{\partial^2}{\partial n_p \partial n_q} \frac{1}{R} dS, \end{aligned} \quad (2.15)$$

where $\sigma = \frac{\partial \phi}{\partial n}$ and $\mu = \phi$.

The right hand side of the Equation 2.15 can be regarded as the normal induced velocity at p due to the mixed distribution of normal dipoles of strength ϕ on S_B , sources of strength $\frac{\partial \phi}{\partial n}$ on S_B , and normal dipoles of strength $\Delta\phi$ on S_W . The source strength and the left hand side of Equation 2.15 is given by the kinematic boundary condition on the body surface. Thus Equation 2.15 is an integral equation of the first kind for the unknown dipole strength μ .

Discretization of Equation 2.15 gives another form of panel method, which we will refer to as the mixed source and dipole method. This can be regarded as the velocity field formulation of the perturbation potential method.

An equivalent formulation derived from Equation 2.14 leads to a mixed distribution of sources and vortices instead of dipoles.

$$2\pi \frac{\partial \phi(p)}{\partial n_p} = \iint_{S_B} \sigma(q) \frac{\partial}{\partial n_p} \left(\frac{-1}{R} \right) dS + \iint_{S_B} \vec{n}_p \cdot \vec{\gamma}(q) \times \nabla_p \frac{-1}{R} dS \\ + \iint_{S_W} \vec{n}_p \cdot \vec{\gamma}(q) \times \nabla_p \frac{-1}{R} dS, \quad (2.16)$$

where $\sigma = \frac{\partial \phi}{\partial n}$ and $\vec{\gamma} = \vec{n}_q \times \nabla_{2-d}\phi$.

If we choose the internal potential on S_B as $\frac{\partial \phi'}{\partial n} = \frac{\partial \phi}{\partial n}$, then ϕ' can be shown to be equal to $-\phi_\infty$ throughout the inside of the body. Then the source strength becomes zero and Equation 2.13 becomes

$$4\pi \frac{\partial \phi(p)}{\partial n_p} = \iint_{S_B} \mu(q) \frac{\partial^2}{\partial n_p \partial n_q} \frac{1}{R} dS + \iint_{S_W} \Delta\mu(q) \frac{\partial^2}{\partial n_p \partial n_q} \frac{1}{R} dS, \quad (2.17)$$

where $\mu = \phi + \phi_\infty \equiv \Phi$.

This is also an integral equation of the first kind for the unknown dipole strength μ . The panel method derived from Equation 2.17 will be referred to as the dipole method. This can be regarded as the velocity field formulation of the total potential method.

Due to the equivalence between dipoles and vortices, Equation 2.17 can be written in a different form,

$$4\pi \frac{\partial \phi(p)}{\partial n_p} = \iint_{S_B} \vec{n}_p \cdot \vec{\gamma}(q) \times \nabla_p \frac{-1}{R} dS + \iint_{S_W} \vec{n}_p \cdot \vec{\gamma}(q) \times \nabla_p \frac{-1}{R} dS, \quad (2.18)$$

where $\vec{\gamma} = \vec{n}_q \times \nabla_{2-d}\Phi$. We will refer to the panel method derived from this equation as the vorticity method.

If we choose the vorticity strength in Equation 2.14, such that it has a given shape function $g(t)$ along the chordwise panels and the spanwise circulation $\Gamma(s)$ is yet to be determined, then

$$\begin{aligned} 4\pi \frac{\partial \phi(p)}{\partial n_p} &= 2\pi\sigma(p) + \iint_{S_B} \sigma(q) \frac{\partial}{\partial n_p} \left(\frac{-1}{R} \right) dS + \iint_{S_B} \vec{n}_p \cdot \vec{\gamma} \times \nabla_p \frac{-1}{R} dS \\ &\quad + \iint_{S_W} \vec{n}_p \cdot \vec{\gamma} \times \nabla_p \frac{-1}{R} dS, \end{aligned} \quad (2.19)$$

where $\vec{\gamma} = \Gamma(s)g(t)\vec{t}_\gamma$, \vec{t}_γ is the direction of the vorticity, and s and t are the spanwise and chordwise coordinates. Given the vorticity shape function $g(t)$ and the normal velocity on S_B from the boundary condition, this is a Fredholm integral equation of the second kind for the unknown source strength σ and the spanwise circulation distribution $\Gamma(s)$. This is the form of the original surface source method by Hess [8]. We will refer to this form as the source based method.

2.5 Comparison of the characteristics of the various panel methods

To compare the characteristics of each panel method, the above described methods are implemented as numerical codes for the analysis of the two-dimensional flow around a hydrofoil. It is assumed that the characteristics of each panel method are preserved for the two-dimensional case, even though the principal objective of the present study is to compare those for the three dimensional case.

Numerical implementation of the panel methods involves approximations of various sorts and inevitably introduces discretization errors which would decrease as the number of panels is increased. The principal approximations involved with any panel methods can be summarized as follows:

- Discretization of the geometry,
- Discretization of the singularity distributions,
- Boundary conditions are satisfied at discrete collocation points,
- A numerical Kutta condition must be imposed.

The simplest discretization will be used in the numerical implementation of the panel methods in order to compare the characteristics of each method.

Of the five different panel methods which were described in the previous sections, the source based method has been used most widely and is known to be accurate for most geometries. However, the source based method is also known to be inaccurate for relatively thin foil sections. For marine propeller applications this is a severe disadvantage because a typical thickness/chord ratio is as little as two percent near the tip. Moreover, the source based method is known to be inaccurate for internal flows, such as the flow inside a long duct.

Because the characteristics of the source based panel method are relatively well known, four other panel methods are actually implemented. They are the perturbation potential method, the total potential method, the mixed vortex and source method, and the vortex method. A brief description of each method will be given, and the more detailed numerical implementation is included in Appendix A.

In the perturbation potential method, the foil geometry is replaced by an N -faced polygon, where N is the number of panels. The singularity strength on each panel is assumed to be piecewise constant. The collocation point, where the discretized

integral equation is satisfied, is selected as a midpoint of each panel. A numerical Kutta condition is satisfied by requiring that the potential jump in the wake be the difference between the potential values of the upper and lower trailing edge panels. The above treatment results in a system of linear equations for the unknown dipole strengths.

The surface velocity, hence the pressure, is calculated by a second order differentiation of the resulting perturbation potential. Finally, the lift and drag are obtained by summing the element pressure forces which are calculated by multiplying the pressure at the midpoint by the arc-length of each panel. Alternatively, the lift can be calculated from Kutta-Joukowsky's law as $\rho U \Gamma$, where Γ is given as the potential jump on the wake surface, and the drag should be zero.

The computer code is applied for a typical hydrofoil section with a thickness/chord ratio of four percent and a camber/chord ratio of two percent. The thickness form is chosen as the NACA 66 mod. form and the camber distribution is chosen as the $a=0.8$ mean camber line, which is widely used in marine propeller blades because of its good performance with respect to cavitation inception. The panel arrangement for 40 elements is illustrated in Figure 2.2.

Convergence characteristics of the perturbation velocity potential distribution and the pressure distribution obtained by the perturbation potential method are shown in Figure 2.3 and 2.4, where number of panels is increased as 20, 40, 80 and 160. The results with 40 panels, which is a typical number of the chordwise panels in three-dimensional application, are shown to be very close to those with 160 panels. The pressure distribution with 160 panels is considered converged and will be used as a standard datum for comparison with the other panel methods.

Geometric discretization for the total potential method is the same as that for the perturbation potential method. Instead of distributing sources and normal dipoles, only normal dipoles are distributed on the foil surface. Since the kernel of Equa-

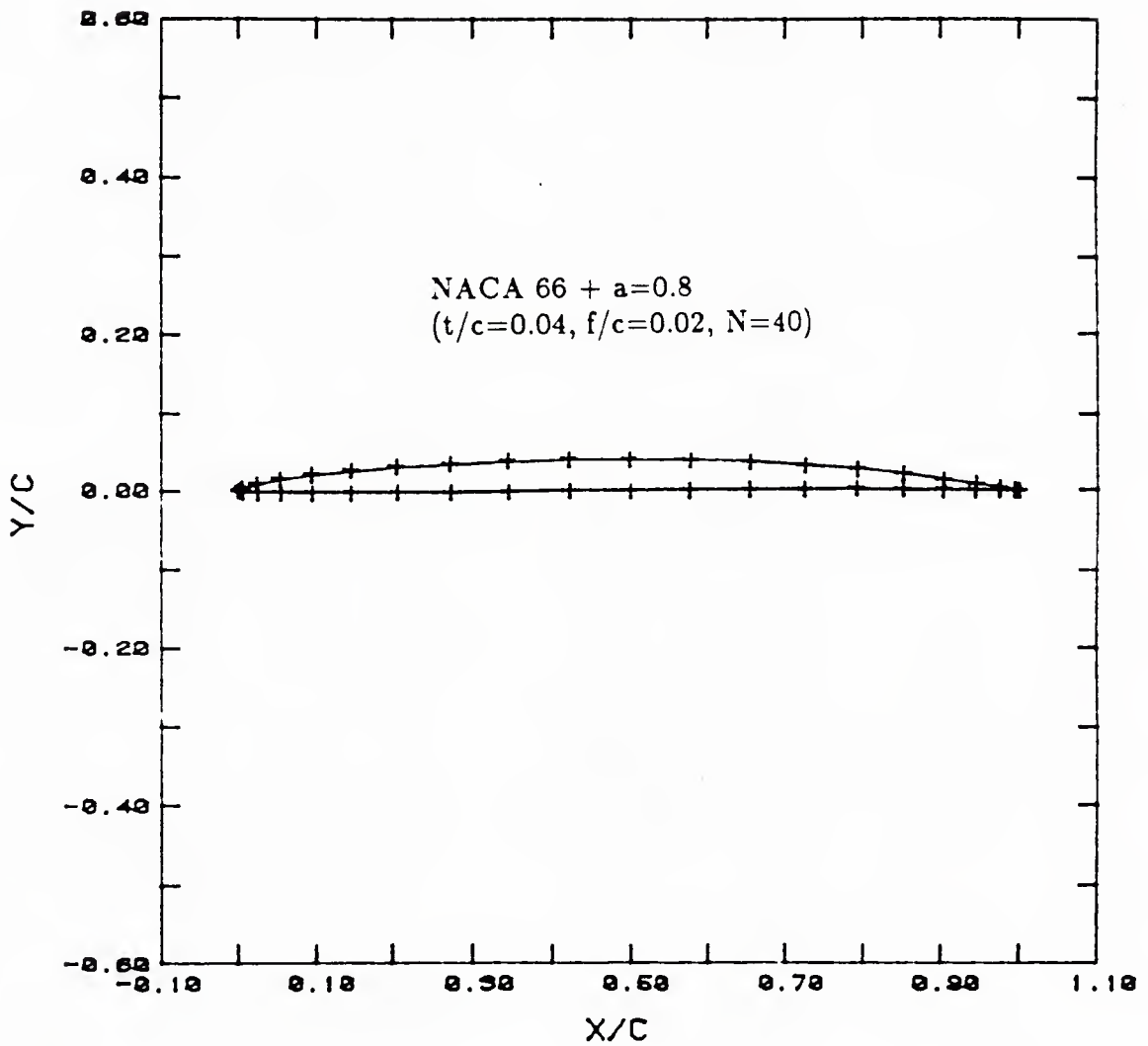


Figure 2.2: Panel arrangement of a typical foil section. (NACA 66 mod. + $a=0.8$ mean camber line, $t/c=0.04, f/c=0.02$)

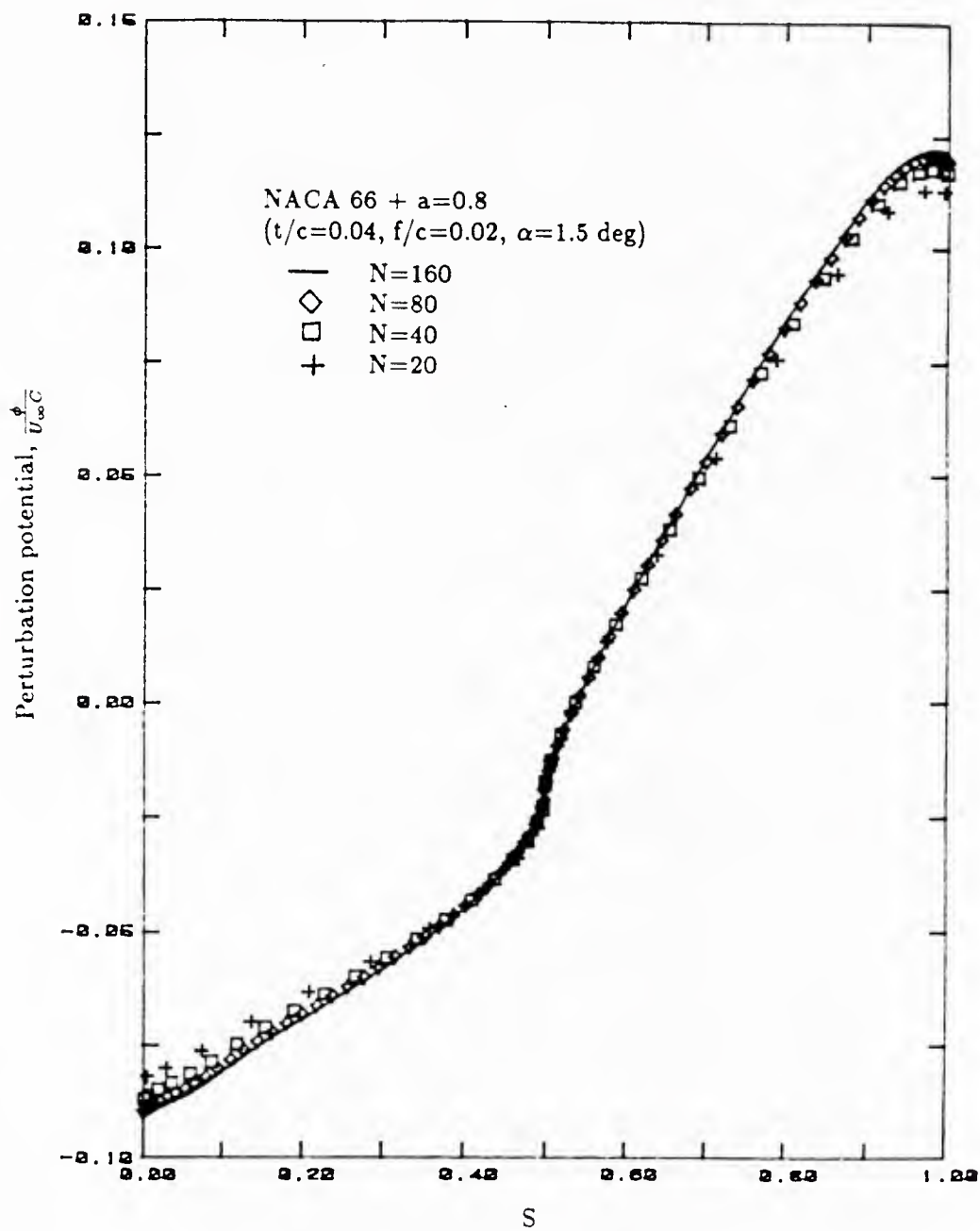


Figure 2.3: Convergence characteristics of the perturbation potential distribution calculated by the perturbation potential method. (NACA 66 + $a=0.8$, $t/c=0.04$, $f/c=0.02$, $\alpha=1.5$ deg)

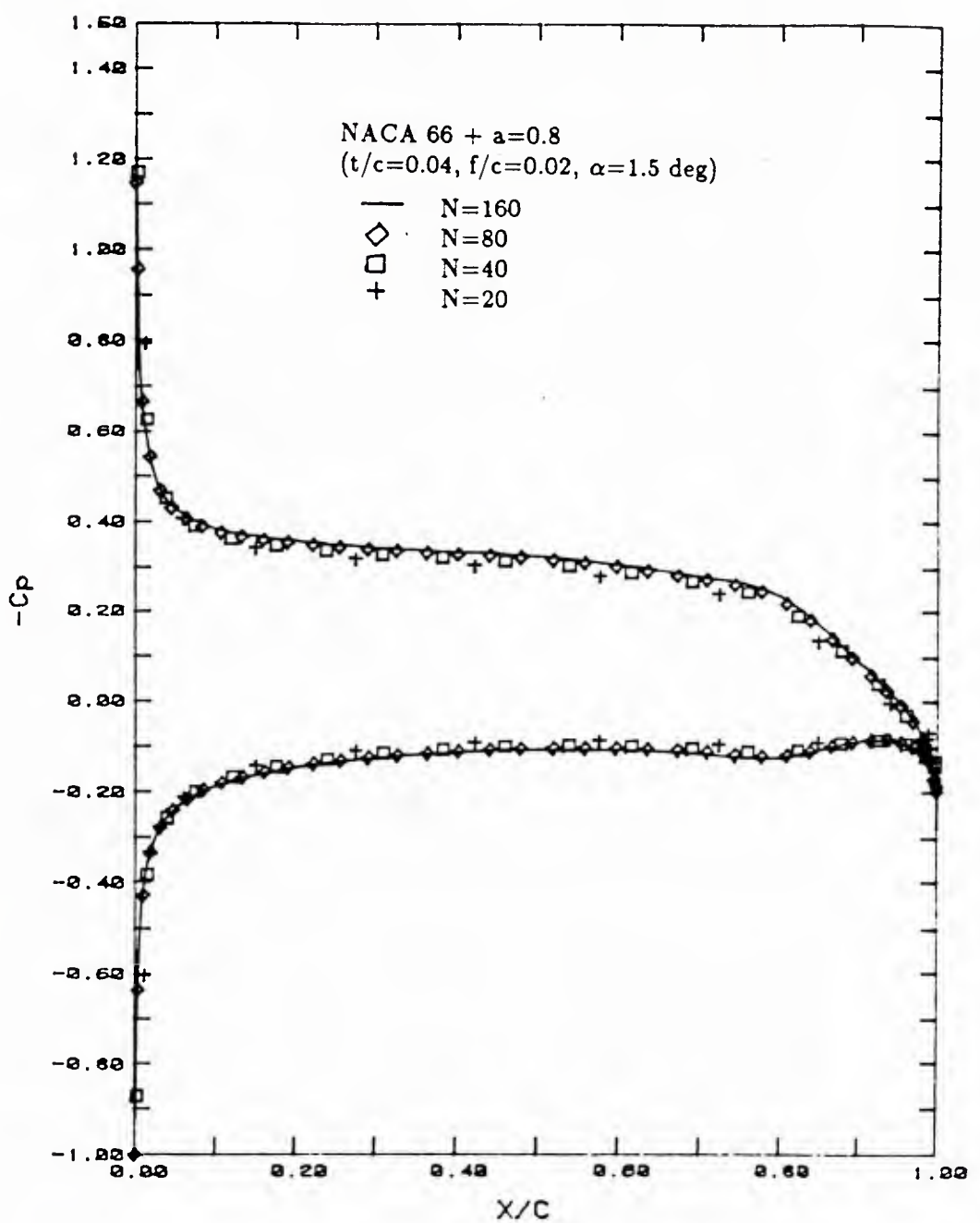


Figure 2.4: Convergence characteristics of the pressure distribution calculated by the perturbation potential method. (NACA 66 + $a=0.8$, $t/c=0.04$, $f/c=0.02$, $\alpha=1.5$ deg)

tion 2.12 is the same as that of the Equation 2.9, the influence coefficient matrix, which is the left-hand side of the linear system of equations, is identical to that of the perturbation potential method. Only the right-hand side of the linear system is different and the unknown is the total potential rather than the perturbation potential. The potential jump on the wake surface is equal to the difference of the total potential values of the upper and lower trailing edge panels.

Convergence characteristics of the total velocity potential distribution and the pressure distribution by the total potential method are shown in Figures 2.5 and 2.6. Comparing Figures 2.3 and 2.5 we notice that the convergence of the total potential method is much faster than that of the perturbation potential results. However, the potential jump in the wake, or the circulation around the foil, by the total potential method converges at the same rate as that of the perturbation potential method. The fast convergence of the total potential in Figure 2.5 is attributable to the fact that the inflow potential is included in the total potential. The disadvantage of the total potential method is that for a non-uniform inflow velocity, the inflow velocity potential is either not defined or difficult to define. In such a case this method can not be applied.

Table 2.1 provides a comparison of the computed values of lift and drag coefficients obtained by an integration of the pressure distribution, with the lift coefficient calculated by Kutta-Joukowsky's law.

The velocity field panel methods are also implemented as numerical codes. Since a constant strength normal dipole is equivalent to a pair of point vortices at the panel edges, a distribution of point vortices is used instead of the piecewise constant dipole distribution. In the mixed source and vortex method, point sources are also distributed on the same location as the vortices. The collocation point is selected on the exact foil surface instead of the midpoint of each panel. An explicit Kutta condition is imposed at the trailing edge by setting the tangential velocity equal to

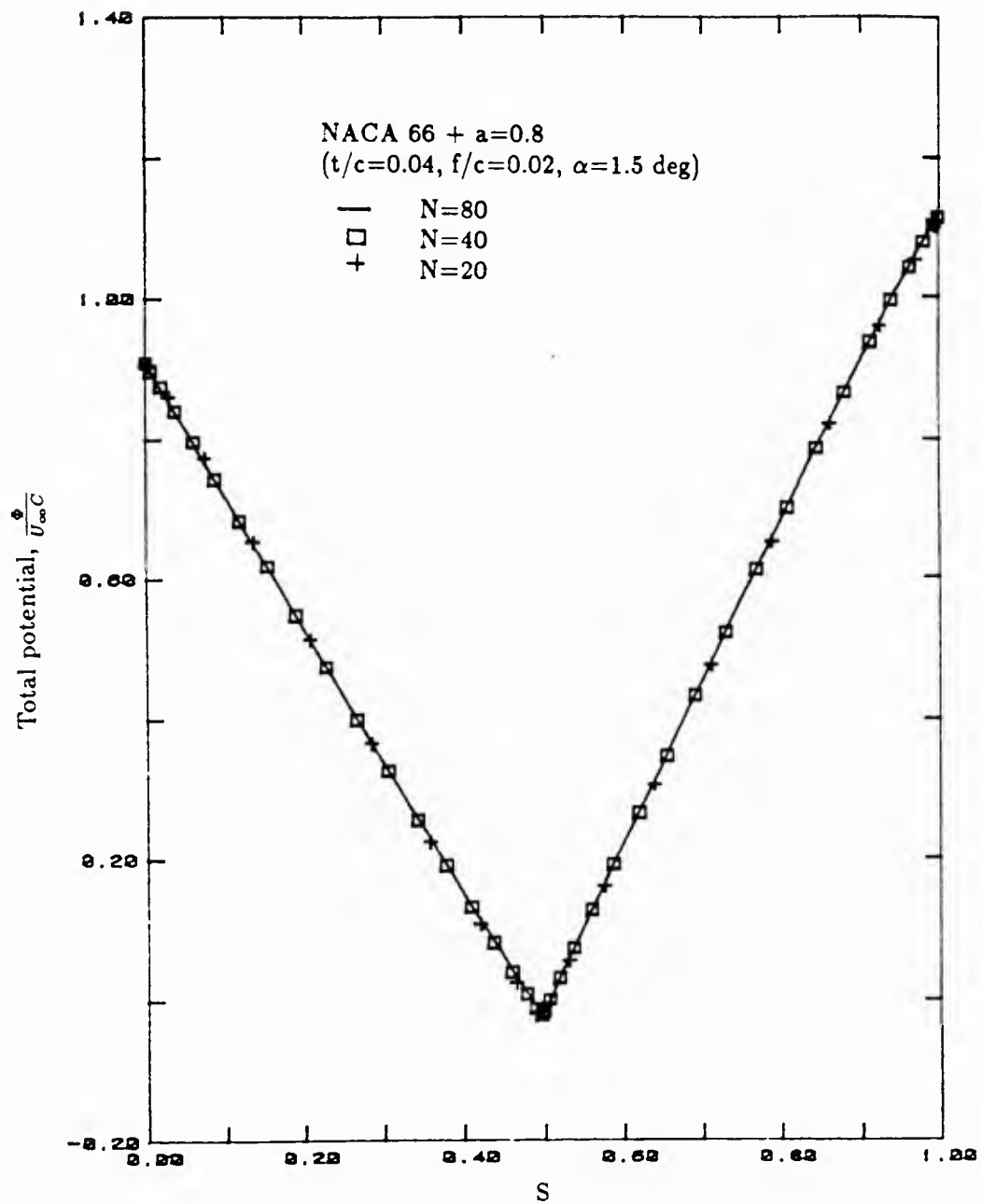


Figure 2.5: Convergence characteristics of the total potential distribution calculated by the total potential method. (NACA 66 + $a=0.8$, $t/c=0.04$, $f/c=0.02$, $\alpha=1.5$ deg)

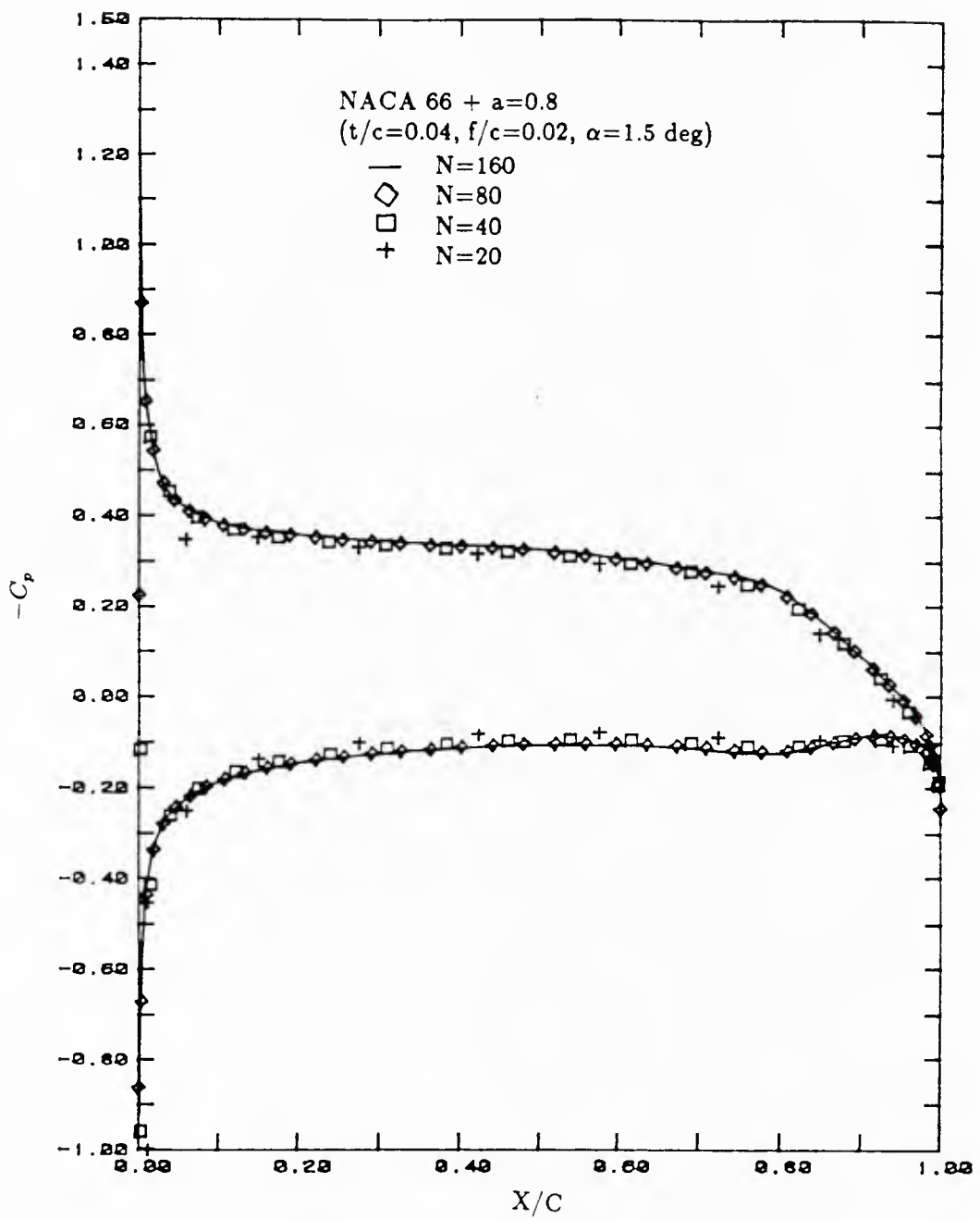


Figure 2.6: Convergence characteristics of the pressure distribution calculated by the total potential method. (NACA 66 + a=0.8, $t/c=0.04$, $f/c=0.02$, $\alpha=1.5$ deg)

Table 2.1: Effect of the number of chordwise panels on computed lift and drag coefficient for the two-dimensional foil section. (NACA 66 mod. + $a=0.8$, $t/c=0.04$, $f/c=0.02$, $\alpha=1.5$ deg.)

N	Pert. potential			Total potential	
	C_L	C_D	$(C_L)_T$	C_L	$(C_L)_T$
20	0.394	0.0027	0.389	0.374	0.395
40	0.410	0.0019	0.407	0.407	0.413
80	0.420	0.0006	0.419	0.401	0.422
160	0.425	0.0002	0.425		

zero. The direction of the tangential velocity is defined to be normal to the bisector of the upper and lower surface at the trailing edge. With this arrangement of point vortices and sources, both methods give exact pressure values at the collocation points for a circular section, regardless of the number of panels. But for a thin section the pressure distributions by both methods give erroneous results.

Pressure distributions by the velocity field panel methods are shown in Figure 2.7 with 40 panels for the same foil geometry. Both the vortex method and the mixed vortex and source method give erroneous pressure distributions, even though those results converge to the correct pressure distribution as the number of the panels is increased. One reason for this erroneous result is that Equation 2.14 is a Fredholm integral equation of the first kind, and the influence coefficient matrix resulting from this equation is not diagonally dominant, which makes the solution unstable. Another explanation might be the fact that the kernel of the equation for the velocity field methods is one order more singular than that for the potential field methods.

From the comparison of the results by different panel methods, the following conclusions are made:

- While practically all methods work well for thick sections, the potential method is substantially more accurate for very thin sections. This is particularly im-

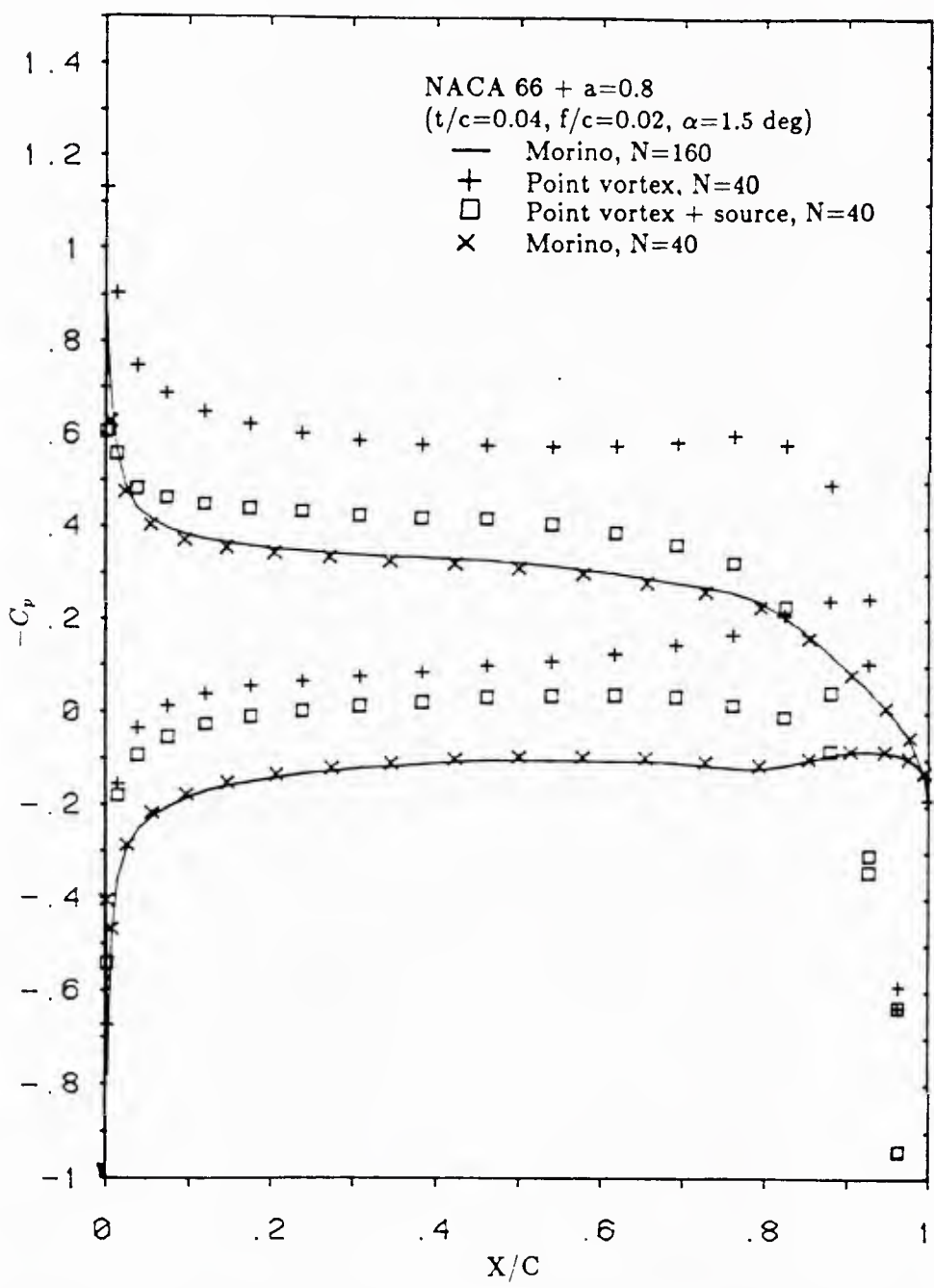


Figure 2.7: Comparison of the pressure distributions by potential method and the velocity methods. ($\text{NACA } 66 + a=0.8, t/c=0.04, f/c=0.02, \alpha=1.5 \text{ deg}$)

portant for marine propellers, where thickness/chord ratios typically vary from twenty percent at the root to as little as two percent near the tip.

- The influence coefficients for the potential induced by unit source and dipole distributions are one order less singular than the corresponding influence coefficients for the velocity. As a result, potential based methods are expected to be less sensitive to errors caused by irregular paneling.
- The computation of the panel influence coefficients, which is a major contributor to the total computing effort, is faster for a potential method than for a velocity method.
- Since the potential influence coefficients are scalar quantities, the required storage for the potential method is one third as great as the storage for a velocity method.
- Both the perturbation potential and the total potential methods give accurate results with similar convergence characteristics. However, in the case of non-uniform inflow velocity, the inflow velocity potential is difficult to define, hence making the total potential method difficult to apply.
- For a marine propeller application, the perturbation potential method is chosen and will be implemented for three dimensional cases in the following chapters.
- In principle a high-order panel method should be more accurate than a low-order method for a given number of elements. However a properly formulated low-order method can achieve similar accuracy by increasing the number of elements. Since the high-order method requires more computational cost per element, the choice is determined by the trade-off between the cost per element and the accuracy for a given number of elements. Youngren et. al. [24] claims

that a low-order potential based panel method is more efficient than a high-order potential method in the case of a subsonic flow and an incompressible flow.

Chapter 3

Numerical formulation

By comparing the characteristics of various panel methods, the perturbation potential method was chosen in Chapter 2 as the most suitable method for the application of the marine propeller problem. In this chapter, the detailed numerical implementation of the perturbation potential method for three dimensional problems will be presented.

A discretized form of the integral equation (Equation 2.9) can be applied to an arbitrary general body in potential flow. The body and wake surfaces are replaced by a large number of plane quadrilateral panels, and the singularity strength distribution on these surfaces is approximated by a piecewise constant distribution over the panels. The control point, where the discretized integral equation is satisfied, is selected as the centroid of each panel. This results in a system of linear algebraic equations for the unknown dipole strengths which are also potential values. From the solution of the linear system, any flow quantities of physical interest can be calculated.

Because our main object of interest is a marine propeller in steady flow, the numerical procedure in this chapter will be focused on the case of marine propeller. However the numerical procedure for a general body would be similar to this.

3.1 Blade geometry

The propeller consists of K identical blades and an axisymmetric hub. For the steady flow problem, both the geometry and the singularity distribution is repeated identically on each blade and on each inter-blade segment of the hub. In order to take advantage of the rotational symmetry of the propeller problem, only $\frac{1}{K}$ portion of the propeller, i.e., one blade and an inter-blade segment of the hub, is discretized. Effect of the other portion of the propeller is included in the calculation of the influence functions, as will be explained in section 3.5.

The propeller geometry problem consists of finding the Cartesian coordinates of points on the actual propeller surface, given the usual propeller geometric descriptions. The geometry is specified with respect to a right-handed, blade-fixed coordinate system, with the x -axis pointing downstream and the y -axis at some arbitrary angular orientation relative to the selected blade. The z -axis completes the right-handed system. Cylindrical coordinates (x, r, θ) are defined as usual, with

$$r = \sqrt{y^2 + z^2} \quad (3.1)$$

and θ being measured clockwise from the y -axis when viewed looking downstream.

The blade is formed starting with a midchord line, which is a space curve defined parametrically by the radial distribution of skew $\theta_m(r)$, and rake $x_m(r)$. By advancing a distance $\pm \frac{c(r)}{2}$ along a helix of pitch angle $\phi(r)$ passing through the midchord line, one obtains the blade leading and trailing edges. The nose-tail line is defined as a helical line between the leading and trailing edge at each radius. The blade mean camber surface may then be defined by adding the camber, $f(r)$, at right angle to the nose-tail line at each radius. Finally, thickness $t(r)$ is added symmetrically with respect to the mean camber line at each radius, again in a cylinder of radius r , and at right angles to f . The coordinate systems and the notations described above are illustrated in Figure 3.1.

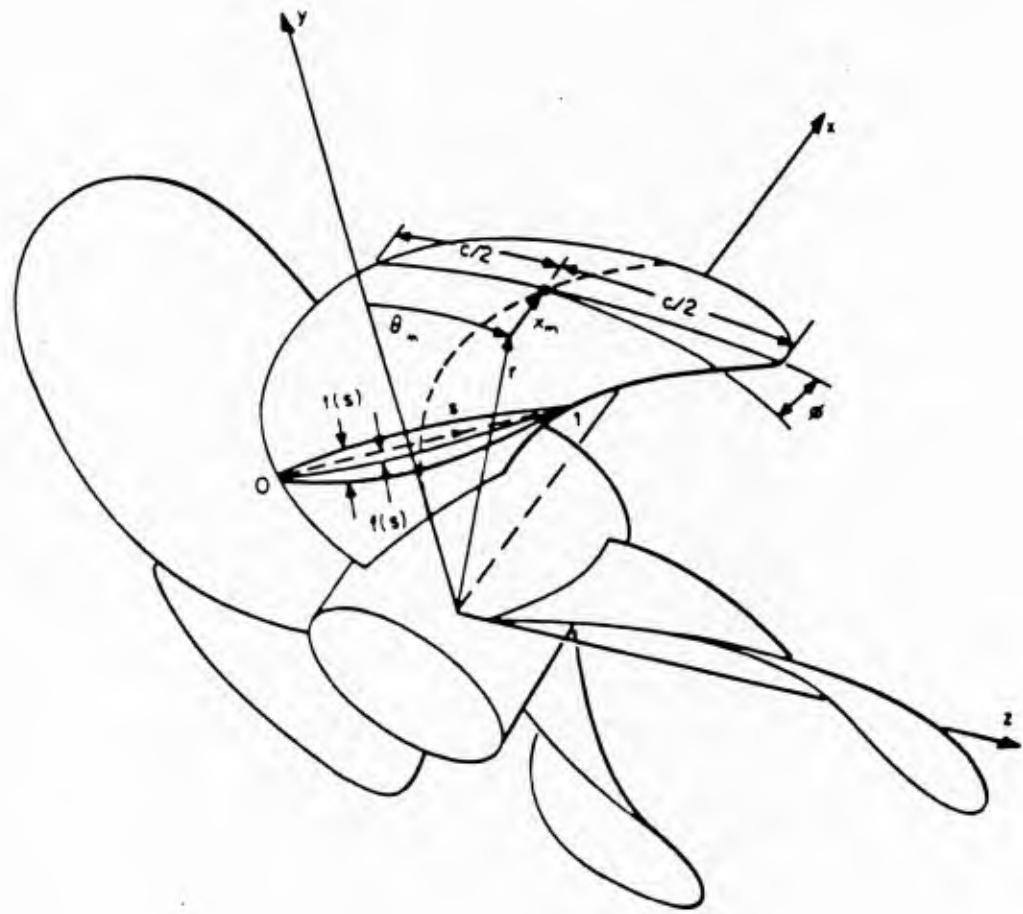


Figure 3.1: Propeller blade geometry notation.

N_c panels are distributed on each chordwise strip of the blade. The chordwise panel arrangement is the same as that of the two-dimensional hydrofoil, and cosine spacing is again adopted. The radial distribution of panel size is determined to concentrate the elements toward the tip. In this case, the radii for M_r panels are,

$$r_m = R_h + (R - R_h) \sin\left(\frac{\pi(m-1)}{2M_r}\right), \quad m = 1, 2, \dots, M_r + 1 \quad (3.2)$$

where R_h is the hub radius, R is the tip radius, and M_r is the number of panels over the radius. Panel arrangement for a three bladed propeller is illustrated in Figures 3.2 and 3.3, where panels are distributed over the full propeller.

3.2 Hub geometry

The geometry of the hub is defined by a profile curve, which can be anything from a constant diameter cylinder to a complete axisymmetric body on which the propeller is mounted. A realistic geometry may be a semi-infinite cylinder on the upstream side, with a given fairwater geometry downstream of the blades. The geometry of the hub which is used in the sample calculation in Chapter 4 is shown in Figure 3.4. Here the profile curve of the fairwater is given as a quartic function of the nondimensional distance from the tail of the hub.

The geometry of the hub can be determined by the following input parameters:

- Maximum hub radius, R_h .
- Computational axial distance in the upstream region, X_u .
- Axial distance from the trailing edge of the blade to the beginning of the fairwater, X_d .
- Axial length of the fairwater, X_t .

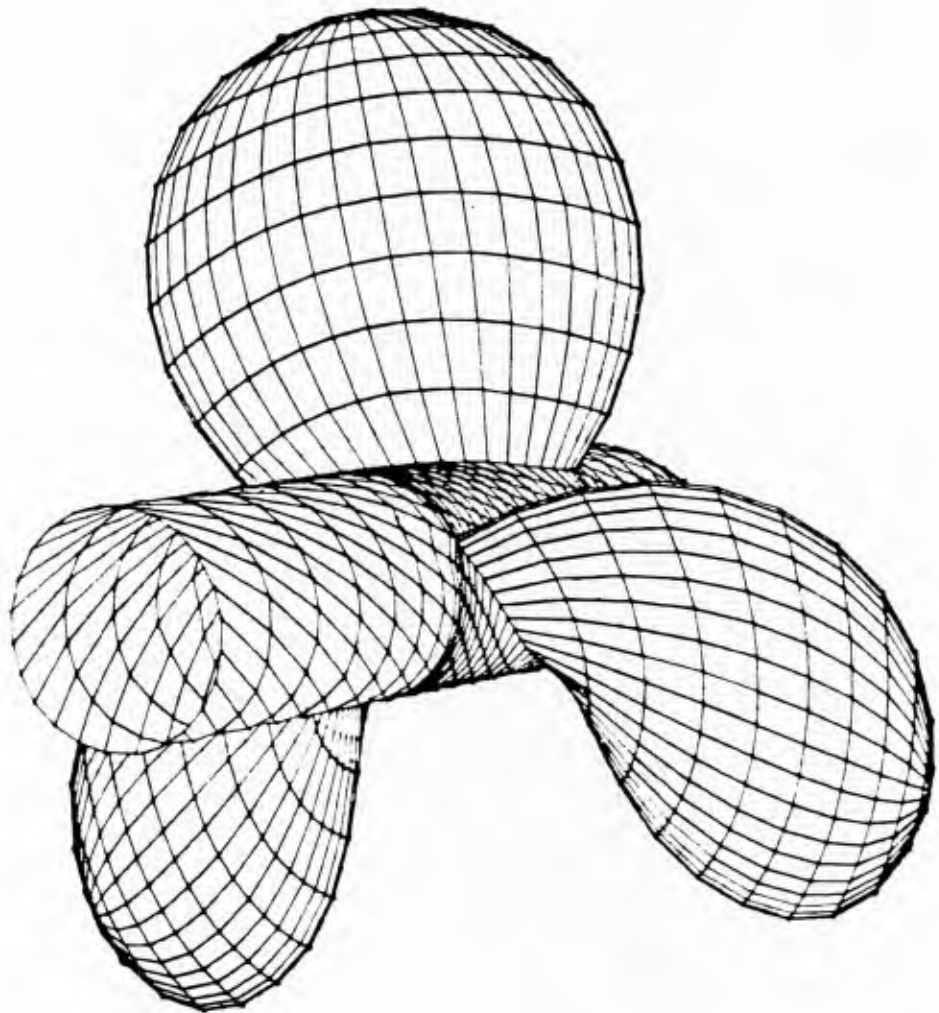


Figure 3.2: Panel arrangement viewed from upstream for a three bladed propeller with a hub. ($N_c=40$, $M_r=10$, $N_u + N_b + N_d + N_t = 39$, $M_\theta=8$)

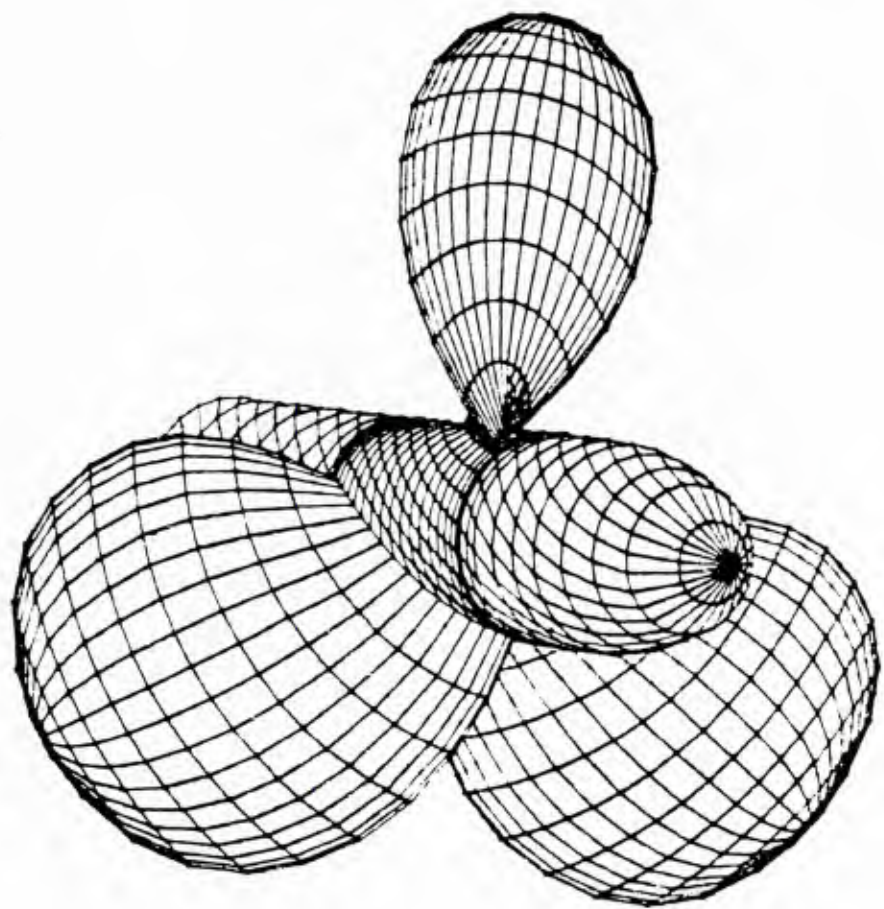


Figure 3.3: Panel arrangement viewed from downstream for a three bladed propeller with a hub. ($N_c=40$, $M_r=10$, $N_u + N_b + N_d + N_t=39$, $M_\theta=8$)

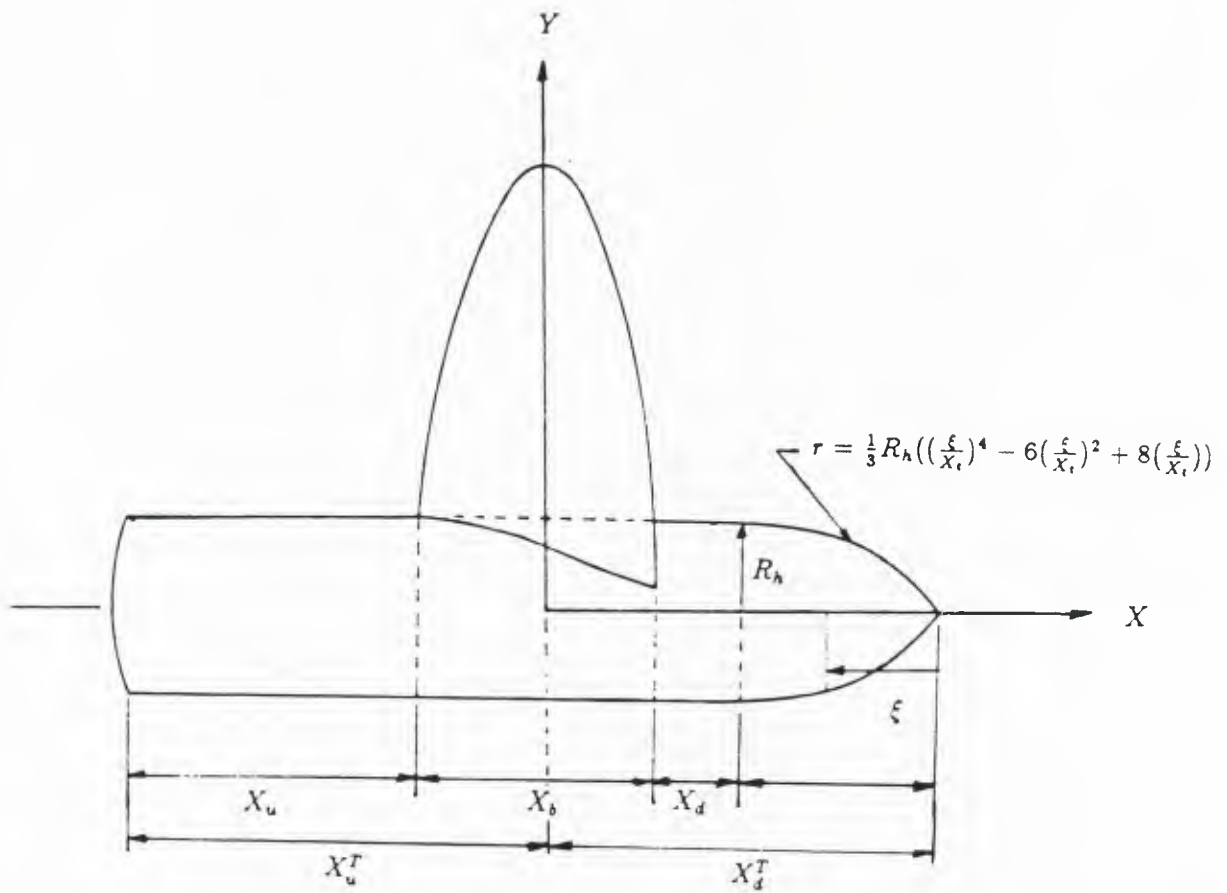


Figure 3.4: Geometry notation of the hub.

The axial distance between the leading and trailing edge, X_b in Figure 3.4, is determined from the geometry of the blade at the root section. X_u^T and X_d^T in Figure 3.4 are the distances from the origin to the upstream end and to the downstream end of the hub.

The number of panels on the hub can be determined by the following integers:

- Number of circumferential panels in the non-redundant region of the hub, M_θ .
- Number of axial panels in the upstream of the blades, N_u .
- Number of axial panels between the leading and trailing edge of the blade, N_b .
- Number of axial panels from the trailing edge to the beginning of the fairwater, N_d .
- Number of axial panels in the fairwater region, N_t .

Here, N_b is determined from the blade panel arrangement, N_d and N_t are determined from the wake panel arrangement, while M_θ and N_u are given as inputs.

The arrangement of hub panels is selected to minimize the possible discretization errors due to the mismatch of the hub panels and the blade or wake panels. Over the axial location between the leading and trailing edge, the hub panels are arranged to match the blade panels at the intersections, and the circumferential panels along the hub are selected to have an equal circumferential angle of $\frac{2\pi}{KM_\theta}$.

The panelling on the hub upstream of the propeller leading edge is purely helical, with a pitch matching the root section pitch of the propeller. The axial spacing is chosen to provide a fine spacing near the propeller and a coarse spacing upstream. In this case, the axial coordinates of the panel boundaries are,

$$x_n = -X_u^T + X_u \sin\left(\frac{\pi(n-1)}{N_u}\right), \quad n = 1, 2, \dots, N_u + 1. \quad (3.3)$$

The arrangement on the hub panels downstream of the trailing edge is similar, except that the pitch is required to match the corresponding pitch of the wake at the hub intersection.

The axial coordinates of the intermediate panels between the blades must be adjusted, particularly near the leading edge, in order to avoid badly shaped panels in this region. Since finite thickness is superimposed to the mean camberline, the axial coordinate of the panel vertex in the suction side of the leading edge can be less than that of the leading edge. If the axial coordinates of the upstream panels were required to be the same in the circumferential direction, panels near the leading edge could actually turn inside-out. To avoid this, the panel boundary, which intersects the suction side of the blade panel boundary and the upstream hub helix at the leading edge, is selected to be a bisector of the upstream helix and the blade panel boundary.

Once the vertex of the first panel at the leading edge is obtained by advancing the same circumferential interval, the axial coordinates of the intermediate panels along the hub are obtained in a smooth manner as illustrated in Figure 3.5, where the expanded plan view of the hub panel arrangement is shown.

The influence of the upstream hub with semi-infinite extent can be accounted for if X_u is increased until no significant change in the potential values near the blades is detected. However it is observed that the dipole strength on the far upstream hub becomes a constant as the value of X_u is increased. While the source panels in the far upstream hub have no influence because of their zero strength, the dipole panels of constant strength over the cylindrical surface of a semi-infinite circular cylinder can be replaced by dipole panels over the circular disk at the beginning of the cylinder. In this way, the computational axial distance of the upstream hub, X_u , can be reduced significantly.

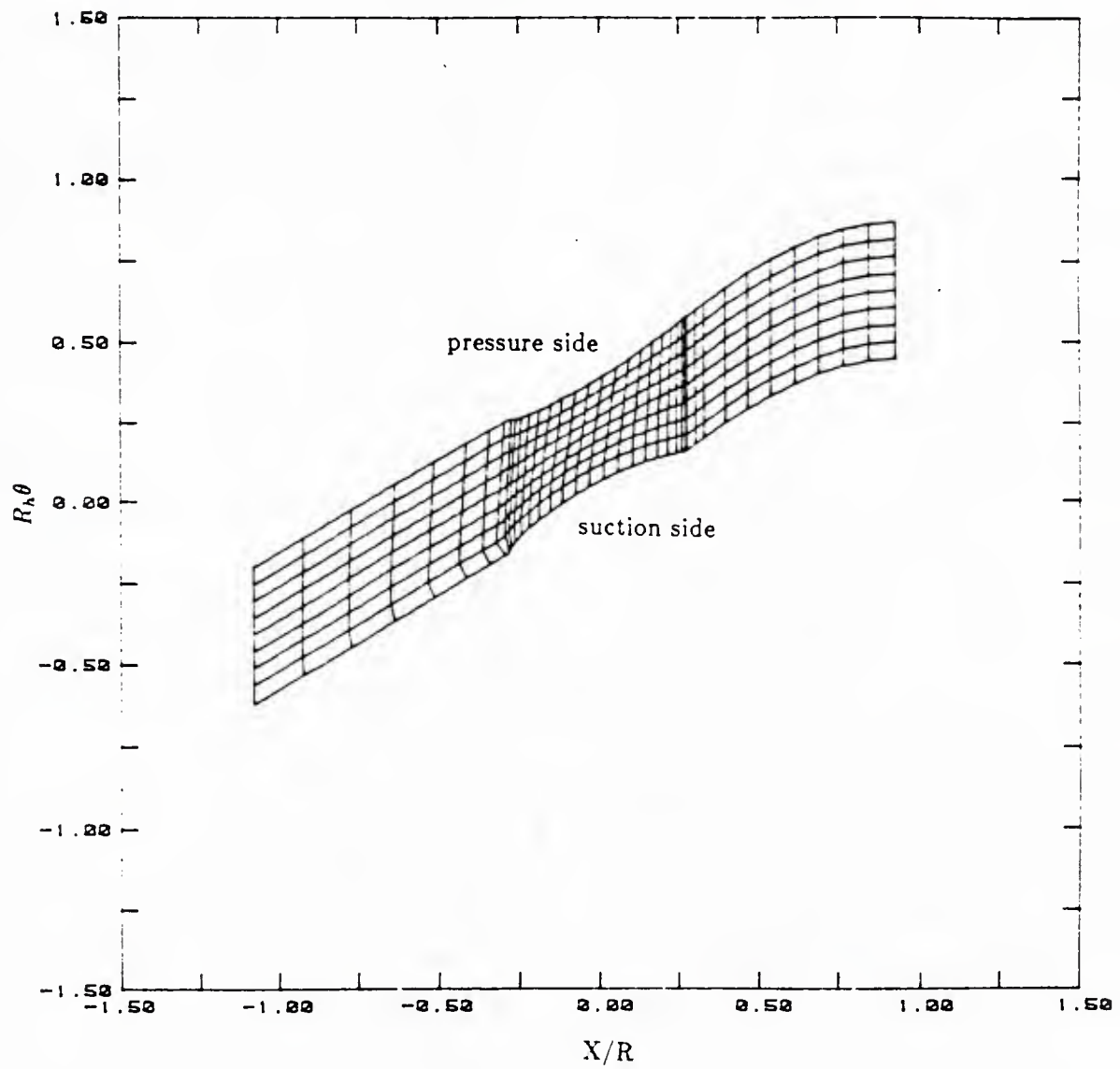


Figure 3.5: Expanded plan view of the hub panel arrangement.

3.3 Geometry of the trailing wake

The influence of the trailing wake on the blade potential is a function of both its strength and geometry. The strength can be related to the radial distribution of circulation on the blade. The geometry, however, follows in an indirect way from the requirement that each element of the trailing vorticity must be aligned with the local flow. Since this local flow depends on the trailing wake geometry in a nonlinear way, an iterative procedure must be employed. Greeley and Kerwin [5] developed a wake alignment scheme which is extremely fast, yet capable of providing the aligned wake geometry. The wake model in the present work follows that given in [5], and only a brief description will be given in this section.

The propeller wake is divided into two parts:

- A transition wake region where the contraction and deformation of the slipstream occurs.
- An ultimate wake region which is composed of K concentrated helical tip and hub vortices.

The axial variation of the radii of the trailing wake can be determined by a limited set of parameters, chosen in accordance with experimental data.

- The ultimate radius of the contracted slipstream, R_w .
- The radius of the hub vortex at the end of the transition wake, R_{wh} .
- The length of the transition wake region, X_{tw} .
- The contraction angle of the tip vortex as it leaves the blade tip, δ_c .

The radius of the outermost trailing vortex in the transition wake is set by a smooth curve consistent with the above wake descriptors.

The radius of the innermost vortex is set to that of the fairwater until it becomes smaller than R_{wh} . Near the apex of the hub where the radius of the fairwater is smaller than R_{wh} , the radius of the innermost trailing vortex is set to R_{wh} . The radii of intermediate trailers are obtained by an interpolation in the same manner as was described in [5]. Figure 3.6 illustrates the axial variation of radius of a set of trailing vortex elements derived by the above description.

The pitch of the transition wake must be allowed to vary to match the local fluid velocity calculated on the wake element. An iterative procedure is required at this stage since the convection velocities depend on the geometry of the wake. In the present work a fully converged wake geometry, obtained from the lifting surface code with the wake alignment scheme [5], is given as an input.

Since normal dipoles are employed to represent the wake, dipole panels, instead of vortex lines, are distributed on the wake surface in the present work.

3.4 Approximation for the induced potential of the ultimate wake

The concentrated tip and hub vortices in the ultimate wake region must, in principle, extend downstream to infinity. Because dipole panels, instead of vortex lines, are used to represent the wake surface, helical strips of dipole panels also must be extended to infinity.

Because the ultimate wake is located far downstream of the blades, the induced potential due to the ultimate wake panels can be approximated by that of a sink disk at the beginning of the ultimate wake region. This will save much computing effort, particularly for the present method which is based on the potential field formulation, since the induced potential due to a dipole panel goes to zero at a slower rate than the induced velocity as the distance between the field point and the panel becomes large.

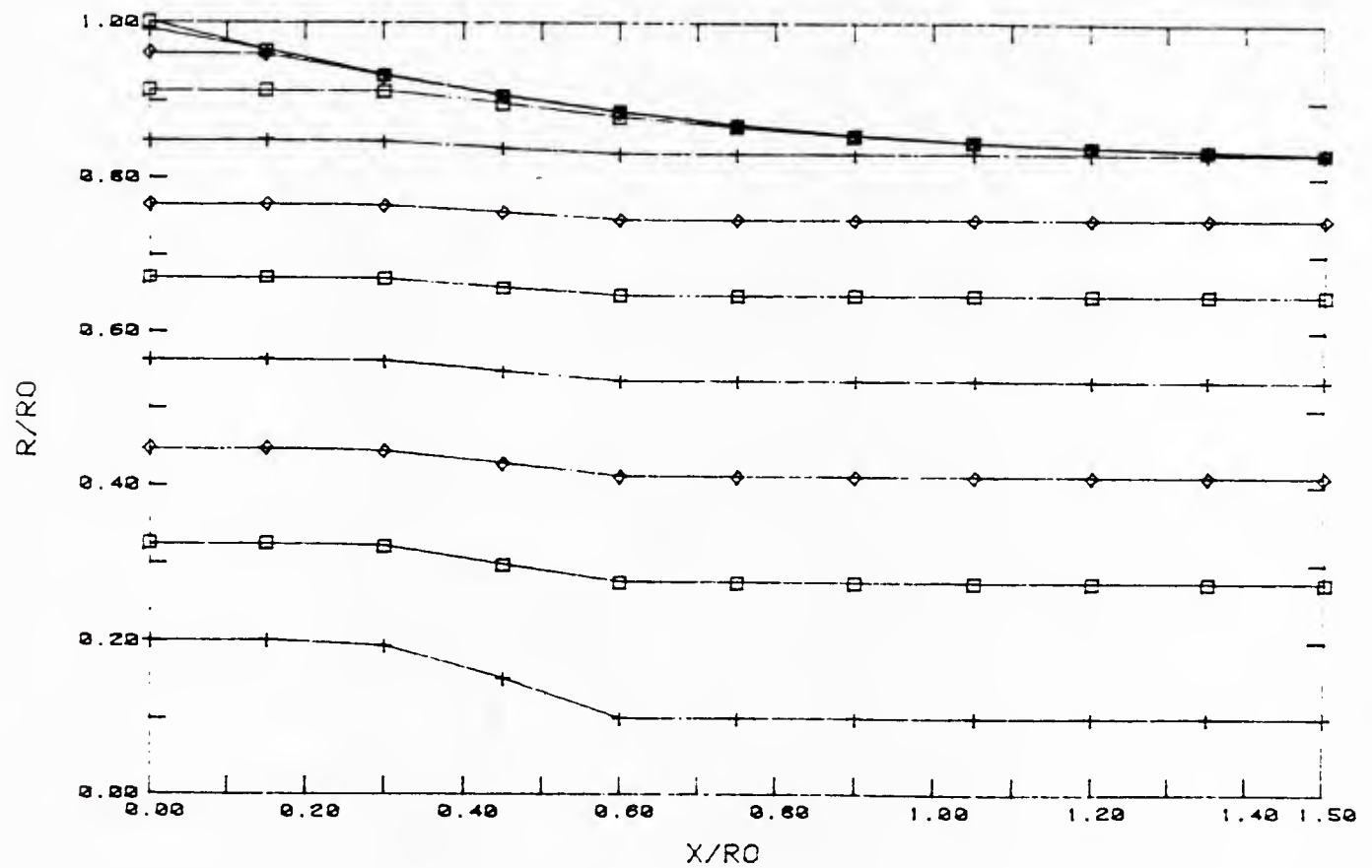


Figure 3.6: Radii of the trailing vortex lines. ($M_r=10$, $R_w=0.83$, $R_{wh}=0.1$, $X_{tw}=1.5$, $\delta_c=15$ deg.)

Consider K equally spaced identical helical vortex lines of semi-infinite extent with a strength Γ and a pitch angle ϕ on a circular cylindrical surface of radius R_w , as shown in Figure 3.7. These vortex lines are connected to the center line vortex via radial vortex lines at the capping surface of the cylinder and downstream at infinity. This system of vortex lines is equivalent to K helical strips of normal dipoles with their axis normal to the helical surface.

For a field point far upstream, the influence (i.e., the induced velocity or potential) due to the system of these vortex lines can be approximated as that of an axisymmetric distribution of helical vorticity on the cylindrical surface and a radial vorticity distribution on the capping surface of the circular cylinder, which is connected to the centerline vortex. This system of vorticity can be regarded as a vorticity representation of a propeller with infinite number of blades. The helical vorticity has the same pitch angle as the vortex lines and has strength $\gamma = \frac{K\Gamma}{2\pi R_w \sin \phi}$.

This system of the vorticity can be decomposed into two components (Figure 3.7):

1. A system of vorticity on the cylindrical surface with its direction chosen as parallel to the x -axis, the radial vorticity on the capping surface of the cylinder, and the centerline vortex. The strength of the helical vorticity is $\gamma \sin \phi$.
2. A distribution of ring vortices on the circular cylindrical surface with its strength $\gamma \cos \phi$.

The system of x -vorticity is equivalent to a distribution of dipoles, with their axis in the $-\theta$ direction, inside the circular cylinder. The induced potential at the upstream field point due to this dipole distribution is zero, because

$$\int_0^\infty dx \int_0^{R_w} dr \int_0^{2\pi} r d\theta \frac{1}{r} \frac{\partial}{\partial \theta} \frac{1}{R} = 0. \quad (3.4)$$

On the other hand, the distribution of ring vortices on the circular cylinder is equivalent to a distribution of x -directed dipoles inside the cylinder. The induced

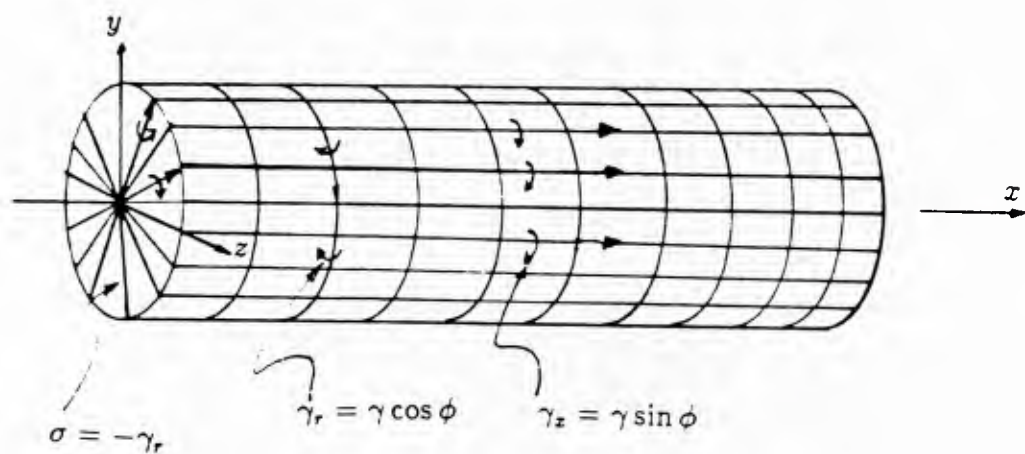
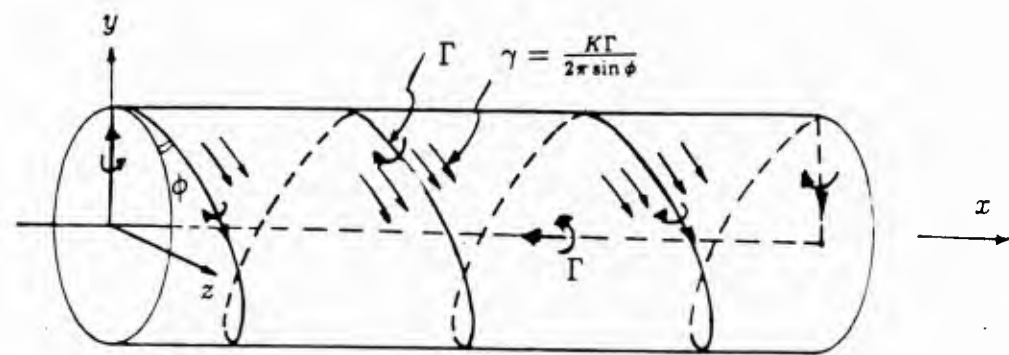


Figure 3.7: Far-field approximation of the ultimate wake.

potential due to this dipole distribution is equivalent to that due to a sink disk of the same strength at the capping surface of the cylinder, since

$$\int_0^{R_w} dr \int_0^{2\pi} r d\theta \int_0^\infty dx \frac{\partial}{\partial x} \frac{-1}{R} = \int_0^{R_w} dr \int_0^{2\pi} r d\theta \left[\frac{-1}{R} \right]_0^\infty = \int_{\text{capping surface}} \int \frac{1}{R} dA. \quad (3.5)$$

As a result, the ultimate wake surface is replaced by a sink disk at the beginning of the ultimate wake region.

A simple numerical verification of the above approximation was performed, and the results are summarized in Table 3.1.

Table 3.1: Comparison of the induced potential due to the helical dipole strips and that due to the sink disk on the capping surface.

Field point (x, y, z)	Helical dipole strip, $N_w \times N_{rev}$					Sink disk, N_s	
	20 × 10	80 × 10	40 × 10	40 × 20	40 × 40	20	Analytic
(-1.0,0,0)	3.703	3.748	3.739	3.848	3.905	3.849	3.902
(-1.0,1,0)	2.932	2.974	2.966	3.074	3.131	3.144	3.191

For the purpose of numerical verification, three helical strips are equally spaced inside the circular disk and the pitch/diameter of the outside helix is given as one. Each helical dipole strip is represented by $N_w \times N_{rev}$ panels, where N_w is the number of panels in one revolution of the helix, and N_{rev} is the number of revolutions of the helix. The sink disk is replaced by N_s triangular panels at the beginning of the helical strip. Axial distance between the field points and the beginning of ultimate wake is given as 1.0.

Induced potential due to the helical dipole strips are calculated by summing the individual contributions from each panel. The analytic result of the induced potential due to the sink disk of the strength $\frac{K\Gamma \cos \phi}{2\pi R_w \sin \phi}$, where $K = 3, \Gamma = 1, R_w = 1$, is also given as a reference.

The first field point is located on the extension of the center line of the helix. Since induced potential divided by the number of the helical strips is constant for any number of helical strips on the field points along the center line, the replacement of the ultimate wake by the sink disk does not involve any approximation. This is numerically confirmed in Table 3.1. The induced potential due to the helical dipole strip on the first field point converges to the analytic induced potential due to the sink disk as N_w and N_{rev} are increased. It is also shown that the result by 20 sink panels on the capping surface of the cylinder is as accurate as that by 40×20 dipole panels on each helical strip, which is equal to 2400 panels.

The second field point is located at the same radius as the wake cylinder, where error due to the farfield approximation is maximum. The difference between the result using 40×40 dipole panels and the analytic result from the sink disk may be regarded as an error introduced by the farfield approximation. Again, 20 sink panels on the capping surface of the cylinder is sufficient to give a very accurate result.

3.5 Discretization of the singularity distribution.

The solution of the boundary value problem consists of determining the strength of singularities representing the propeller and the trailing wake, so as to satisfy the integral equation (Equation 2.9). The continuous distribution of singularities on the propeller and wake surface is approximated by a stepwise distribution over the quadrilateral panels. Since the strengths of sources are prescribed by the kinematic boundary condition (Equation 2.2), only the dipole strengths are to be determined.

As described in section 3.1, surface panels are distributed only on the selected blade and the inter-blade segment of hub. Effects of the other portions of propeller are included by summing the influence functions calculated by rotating the control points an angle $\frac{2\pi}{K}$ about the propeller axis until all blades are accounted for. This is equivalent to having equal panelling on all blades.

The four vertices of the panel are located on the exact surface of the propeller and the wake, which in general are not on a plane. The vertices of the plane panel are constructed as follows. Assuming that four offset points are specified on the exact surface, adjacent offset pairs are connected by straight segments. Their midpoints can be shown to lie on a plane. The plane vertices are then obtained by projecting the offset points on that plane. This construction minimizes in a mean-square sense the distance of the offsets from the quadrilateral plane. In addition, the sides of adjacent panels only contact each other at a single point, so their interior surfaces do not intersect.

The influence functions for the quadrilateral source and dipole panels are computed using the formulation developed by Newman [21]. The induced potential is computed exactly for nearby panels, while it is approximated by a multipole expansion for more distant panels. Finally, the panels which are sufficiently distant are treated as point sources and dipoles. This is really the heart of any panel code, and it is essential that the computer code for the influence function be both robust and efficient.

The dipole strength of each panel, which is also a potential value on the panel, is determined by satisfying a discretized form of the integral equation (Equation 2.9) on the control point, which is chosen as the centroid of the panel. Adopting piecewise constant singularity strengths on the plane quadrilateral panel, the integral equation can be expressed as a system of linear equations.

$$\sum_{j=1}^{N_{panel}} D_{ij} \phi_j + \sum_{m=1}^{M_r} W_{im} (\Delta\phi)_m = \sum_{j=1}^{N_{panel}} S_{ij} \left(\frac{\partial \phi}{\partial n} \right)_j, \quad i = 1, 2, \dots, N_{panel}, \quad (3.6)$$

where N_{panel} is the total number of panels on the blade and the hub, M_r is the number of radial panels on the blade, D_{ij} is the induced potential at the i -th control point due to the j -th dipole panel of unit strength, S_{ij} is the induced potential at the i -th control point due to the j -th source panel of unit strength, W_{im} is the induced potential at the i -th control point due to the M -th streamwise dipole strip in the wake, and $\left(\frac{\partial \phi}{\partial n} \right)_j$

is the source strength at the j -th panel given by the boundary condition. Since the strength of the M -th streamwise dipole strip, $(\Delta\phi)_m$, can be related to the potential values on the blade by a numerical Kutta condition, Equation 3.6 is sufficient to determine the unknown potential values.

3.6 Kutta condition

A numerical Kutta condition must be imposed to specify the circulation around the body, which is equal to the potential jump in the wake surface. An approximate Kutta condition for the potential based panel method, which was first introduced by Morino [20], required that the strength of the dipole sheet in the wake be equal to the difference in the value of the dipole strengths of the two panels adjacent to the trailing edge.

Morino's Kutta condition gives accurate results for thin two-dimensional foil sections with small trailing edge angles. However, it is found that this form of Kutta condition contains a fundamental error when the free stream contains a component in the direction of a line connecting the control points of the two trailing edge panels. Therefore, for three dimensional problems with significant cross flows, a new form of Kutta condition is needed to satisfy the zero loading condition at the trailing edge.

For two-dimensional problems where no cross flow component exists, a Kutta condition can be the requirement that the potential jump in the wake should be equal to the difference in the total potential values, instead of the perturbation potential values, of the upper and lower panels at the trailing edge.

$$(\Delta\phi)_{wake} = \Phi^u - \Phi^l = \phi^u - \phi^l + \vec{U}_\infty \cdot \vec{r}_{t.e.} \quad (3.7)$$

where $\vec{r}_{t.e.}$ is the vector between the the control points of the two trailing edge panels. The correction term to Morino's Kutta condition, $\vec{U}_\infty \cdot \vec{r}_{t.e.}$, represents the potential jump between trailing edge control points due to the inflow velocity and vanishes for

cusped foil sections as the upper and lower control points approach the trailing edge.

Figures 3.8 and 3.9 show the perturbation potential and the pressure distribution for a circular cylinder at 90 degree angle of attack, calculated by the two-dimensional panel code with and without the additional correction for the potential jump. Without this correction, the circulation converges to about half the correct value regardless of the panel density. With the correction term, the potential and pressure distributions recover the analytic results. But it should be noted that the differences between the results obtained by the original Morino Kutta condition are very small for thin two-dimensional sections.

For three dimensional problems with significant cross flows, this is still not satisfactory. For the region near the tip, where the cross flow component around the tip from the pressure side to the suction side of the blade is prominent, the result by the modified Morino Kutta condition shows a spurious non-zero loading at the trailing edge. A new form of Kutta condition is required which enforces the zero loading condition, as explained below.

Figure 3.10 shows the flow at the trailing edge near the tip. Total velocity on the pressure (lower) side, \vec{V}^l , has an outward component, while that on the suction (upper) side, \vec{V}^u , has an inward component due to the cross flow around the tip. They should have the same magnitude to satisfy the zero loading condition, since the static pressure in steady flow is the same on the upper and the lower side of the wing at the trailing edge.

Define a local coordinate system, where s is chosen as the direction of mean velocities of the upper and lower surfaces, and n is chosen normal to s toward the tip. The trailing edge velocities can be decomposed into s , n directions, and for a zero loading at the trailing edge, the following equations must be satisfied.

$$V_s^u = V_s^l \quad (3.8)$$

$$V_n^u = -V_n^l \quad (3.9)$$

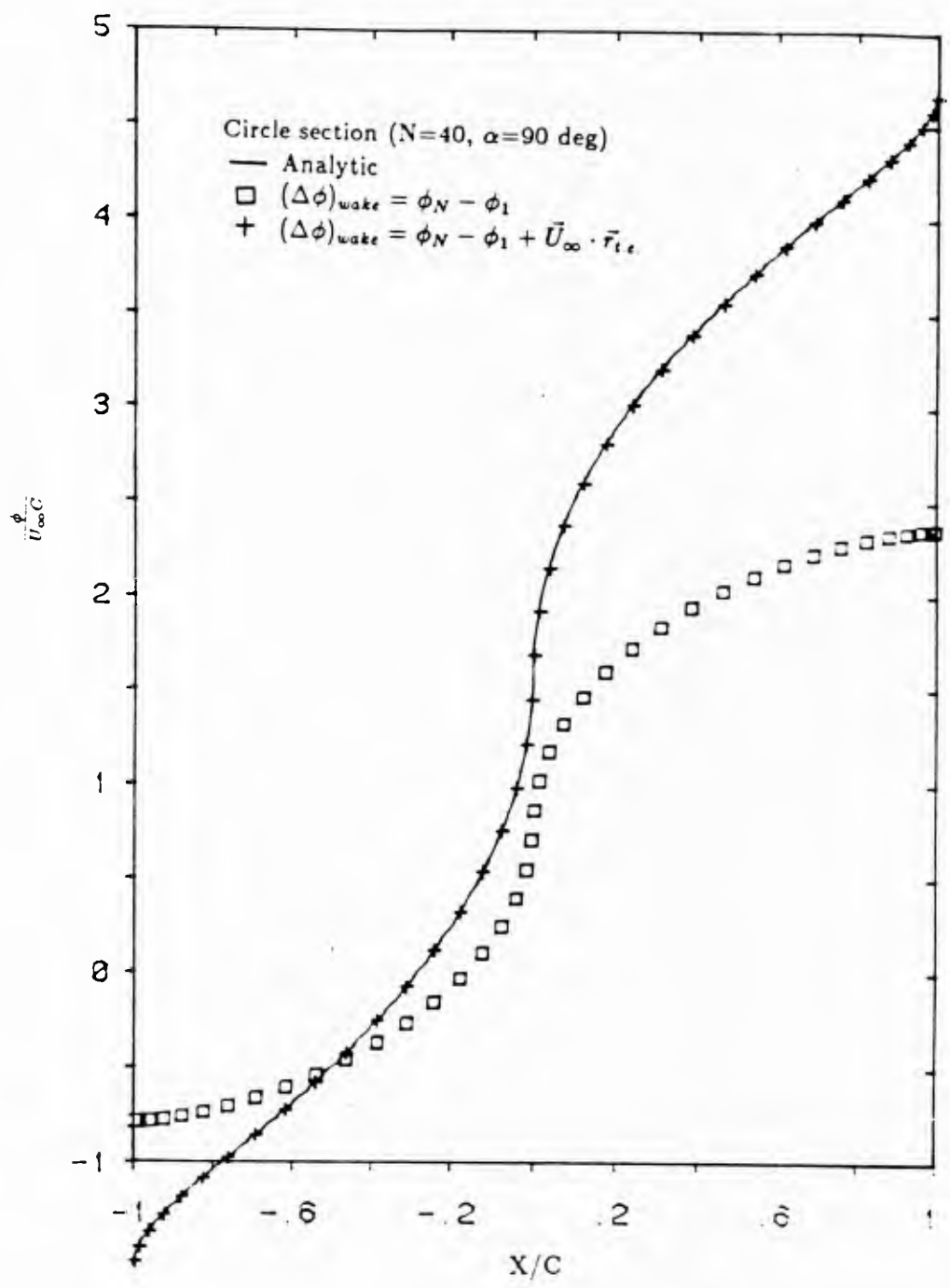


Figure 3.8: Perturbation potential distribution for a circular cylinder at 90 degree angle of attack.

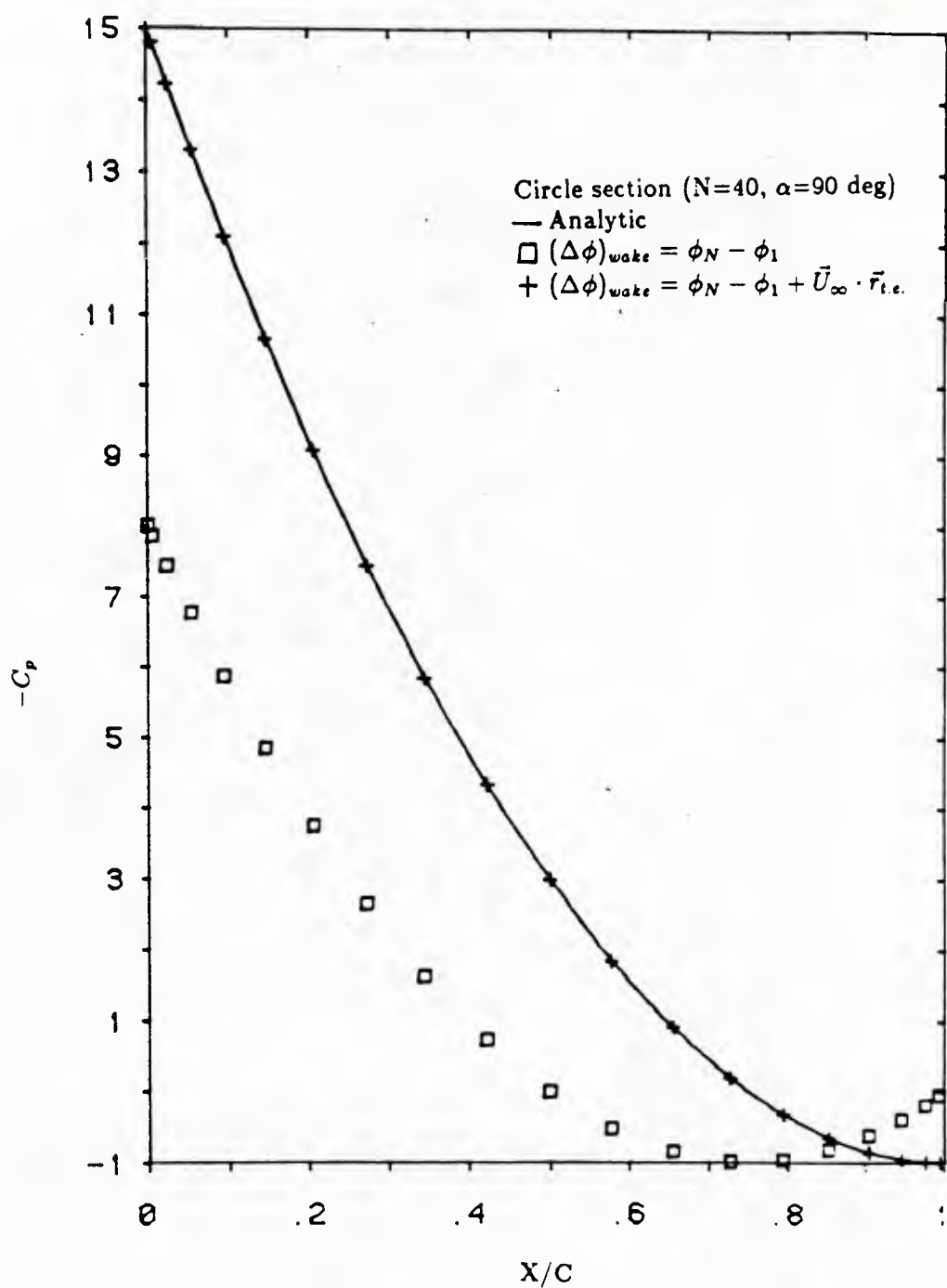


Figure 3.9: Pressure distribution for a circular cylinder at 90 degree angle of attack.

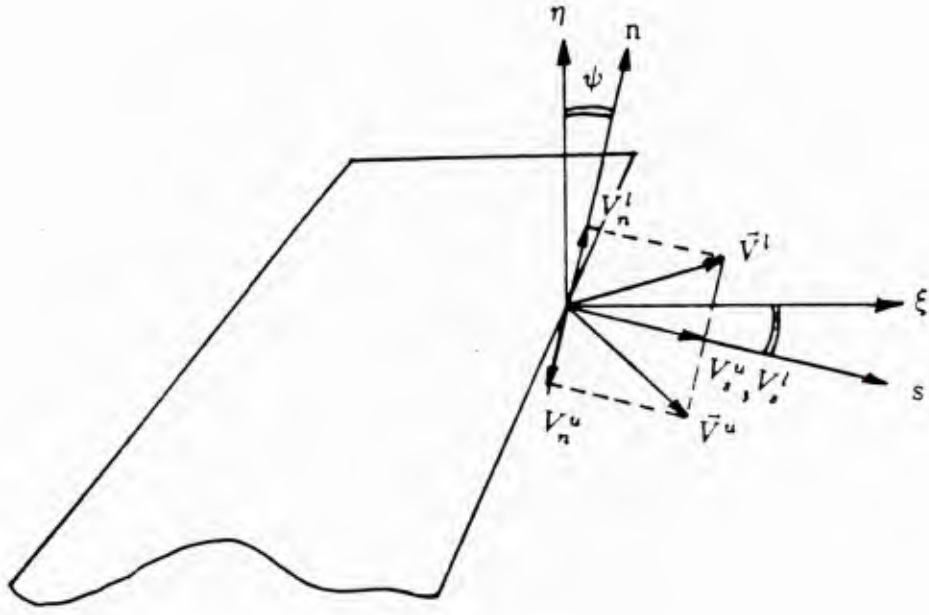


Figure 3.10: Magnified flow at the trailing edge near the tip.

where V_s^u, V_n^u, V_s^l , and V_n^l are s, n components of \bar{V}^u and \bar{V}^l , respectively.

In general, the calculated velocities at the trailing edge using the modified Morino Kutta condition do not have the same magnitude. As a result, the pressure values on the upper and lower surfaces do not match. This non-zero loading at the trailing edge becomes large toward the tip, where the three-dimensional cross flow component becomes large.

In the present work, an explicit pressure Kutta condition is employed, which requires the pressures on the last panels at the trailing edge be equal. The potential jump in the wake surface is expressed as,

$$(\Delta\phi)_{wake} = \phi_{t.e.}^u - \phi_{t.e.}^l + \bar{U}_\infty \cdot \vec{r}_{t.e.} + K(\Delta C_p)_{t.e.} \quad (3.10)$$

where $(\Delta C_p)_{t.e.}$ is the difference of the pressure values of the upper and lower panels at trailing edge and K is a parameter to be found to ensure the zero loading condition.

Due to the nonlinear aspect of the pressure Kutta condition, an iterative solution algorithm is employed.

In the numerical implementation, the potential jump at the m-th dipole wake strip is

$$(\Delta\phi)_m^{(k)} = (\phi_m^{N_c} - \phi_m^1)^{(k)} + (\vec{U}_\infty \cdot \vec{r}_{t.e.})_m^{(k)} + K(\Delta C_p)_m^{(k-1)}, \quad (3.11)$$

where $\phi_m^{N_c}$ and ϕ_m^1 are the potential values of the upper and lower panels at the trailing edge. Then Equation 3.6 becomes

$$\begin{aligned} \sum_{j=1}^{N_{panel}} D_{ij} \phi_j^{(k)} + \sum_{m=1}^{M_r} W_{im} (\phi_m^{N_c} - \phi_m^1)^{(k)} &= \sum_{j=1}^{N_{panel}} S_{ij} \left(\frac{\partial \phi}{\partial n} \right)_j \\ &\quad - \sum_{m=1}^{M_r} W_{im} [(\vec{U}_\infty \cdot \vec{r}_{t.e.})_m K(\Delta C_p)_m^{(k-1)}], \quad i = 1, 2, \dots, N_{par} \end{aligned} \quad (3.12)$$

During the iteration process, the value of ΔC_p is obtained from the previous iteration, and the value of K is determined by the Newton-Raphson method. However, the influence coefficient matrix is unchanged in the process. The initial guess, $(\Delta\phi)_m^{(0)}$, is taken by setting the value of K to zero.

On the other hand, the difference of the n-direction velocities at the trailing edge panels in Figure 3.10 is related to the magnitude of the trailing vorticity. The trailing vorticity is in the s-direction and the magnitude of it must be equal to the spanwise derivative of the circulation:

$$\gamma = |\vec{\gamma}| = |V_n^u - V_n^l| \cos \psi = - \frac{d\Gamma}{d\eta}, \quad (3.13)$$

where ψ is the angle between n - and η -coordinates. This is the compatibility condition, which is a measure of the consistency of the panel method.

3.7 Linear system solution

The unknown dipole strengths are determined by the solution of the system of linear equations. For a small number of unknowns, such as two-dimensional problems or

simple three-dimensional problems, Gauss reduction can be used at the outset to decompose the matrix into lower and upper triangular forms for subsequent solutions with different right hand sides. But for complex three-dimensional geometry, the time required for the Gauss reduction method would become prohibitive.

Since several iterations are required to satisfy the pressure Kutta condition, an efficient matrix solver is an essential feature of the present panel method. In the present work, an accelerated iterative matrix solver developed by Clark [4] is employed. This method is found to converge very rapidly for the kind of influence coefficient matrix encountered with the present potential method, and requires very small computing time compared to the Gauss reduction method even for a linear system with small number of unknowns.

As the number of unknowns becomes large, the computer memory to store the full influence coefficient matrix increases in proportion to N^2 , where N is the number of unknowns. Instead of storing all of the matrix elements into the computer memory, they are saved in the outside storage and retrieved when necessary. In this way, the computer memory required can be significantly reduced even though more computer time is required for storing and retrieving the matrix elements.

Table 3.2 provides a comparison of the computing times of the Gauss reduction method and the accelerated iterative method using a DEC Microvax 2. Here, the computing times required for memory resident Gauss reduction are given for the 424 and 724 panel cases, while those for 840 and 1680 panels include the time required for external storage and retrieval of the matrix elements. The computing time for the matrix solver is for one iteration of the pressure Kutta condition. The effectiveness of the iterative solver is clearly shown here. The accelerated matrix solver will be used for all the sample calculations in Chapter 4.

Table 3.2 also tabulates the required computing times for the calculation of the influence coefficient matrix. Here again the computing times for 840 and 1680 panel

cases include the time required to store the matrix elements.

Table 3.2: Comparison of the computing times of the influence function calculation and the matrix solver.

N	Inf. coefficient	Matrix solution	
		Gauss	Iterative
424	330 sec	330 sec	30 sec
704	800	1510	77
840	2100		180
1680	5300		670

3.8 Calculation of velocities, pressures, forces and moments.

Once the potential values have been determined, surface velocities can be calculated either by numerical differentiation of the potential or by direct calculation of the source and dipole panel influence functions. The latter approach is found to be not as successful since the velocity influence functions are more singular and therefore more sensitive to the position of the control point within each panel.

A local second order distribution of the perturbation potential is assumed on the five panel centers (i.e., a central panel and its immediate neighbors), and a local tangential perturbation velocity is obtained by differentiation. The total tangential velocity is obtained by a vector sum of the perturbation velocity and the undisturbed inflow velocity.

As shown in Figure 3.11, where u, v -coordinates are formed by connecting the midpoints of the sides of a panel and ξ, η -coordinates are chosen as local orthogonal coordinates, the calculated perturbation velocities in the u, v direction are not at right angles to each other. Each velocity component is a projection of the velocity vector

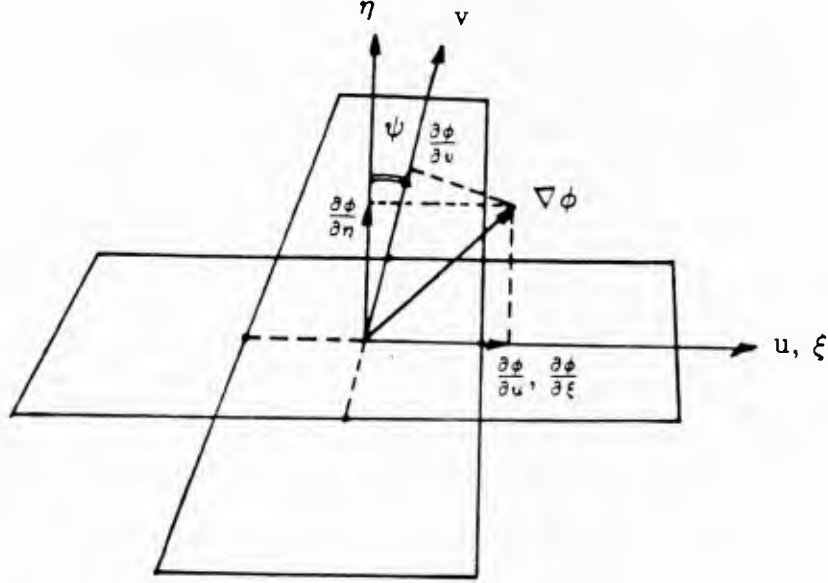


Figure 3.11: Summation of the velocity component.

onto the u, v directions, respectively. The η -velocity component is calculated as

$$\frac{\partial \phi}{\partial \eta} = \frac{\frac{\partial \phi}{\partial v} - \frac{\partial \phi}{\partial u} \sin \psi}{\cos \psi} \quad (3.14)$$

where ψ is the angle between the η and v -coordinate. The perturbation velocity and the inflow velocity are added in the local orthogonal coordinates.

The pressure coefficient is calculated using Bernoulli's equation, and the non-dimensional pressure coefficient is defined as,

$$C_p = \frac{p - p_\infty}{\frac{1}{2} \rho U_\infty^2} \quad (3.15)$$

Finally, total forces and moments are obtained by summation of individual panel force vectors. In order to obtain practically useful results which can be compared with experiments, a viscous drag correction is needed. On each panel, a viscous friction force is added in the direction of the inflow velocity. The viscous friction coefficient

is given as 0.003 for the calculation at the design condition and that at the off-design condition is determined from the two-dimensional section drag coefficient curves.

Integrated thrust and torque coefficients are calculated by

$$K_T = \frac{T}{\rho n^2 D^4} = \frac{J^2}{8} K \sum_i \frac{A_i}{R^2} (C_p)_i (n_z)_i, \quad (3.16)$$

$$K_Q = \frac{Q}{\rho n^2 D^5} = \frac{J^2}{16} K \sum_i \frac{A_i}{R^2} (C_p)_i [(n_y)_i \frac{z_i}{R} - (n_z)_i \frac{y_i}{R}], \quad (3.17)$$

where $x_i, y_i, z_i, (n_z)_i, (n_y)_i, (n_z)_i$ and A_i are, respectively, control point coordinates, unit normal vector components, and area for i -th panel. These sums can be performed separately over blades and hub. The propeller efficiency is defined as

$$\eta = \frac{J}{2\pi} \frac{K_T}{K_Q}. \quad (3.18)$$

Chapter 4

Numerical results

Three separate codes for different problems, i.e. a wing, an axisymmetric duct and a propeller problem, are implemented in order to verify the theory given in the previous chapters.

Instead of writing a general purpose code which would take coordinates of the panel vertices as inputs, each code is written for a specific geometry with specific inputs which are defined in a natural way for the geometry. In this way each code is kept to a reasonable size, and the possible occurrence of fatal errors due to inconsistent inputs can be minimized. A perspective view of the configuration with the hidden lines removed can also be plotted in order to check the geometry before calculating the influence coefficients.

Numerical results by each code will be presented in separate parts of this chapter.

Part I

Wing problem

The wing-body configuration is regarded as a two bladed propeller with infinite pitch, and accordingly the geometric part of the code for the wing problem is written as a special case for a propeller problem. An option for a fuselage is given in order to calculate the performance of the wing-body or wing-only configuration.

However, the wing problem possesses a lateral symmetry with respect to the center plane, while the propeller problem is rotationally symmetric with a separating angle of $\frac{2\pi}{K}$. Reduction of the system of equations is obtained by exploiting the symmetry. A frozen wake geometry is assumed on the surface formed by the extensions of the nose-tail lines of the wing sections.

4.1 Ellipsoid at zero angle of attack

The first example is chosen to verify the code by comparing the results with the known analytic results for a simple geometry. The example is an ellipsoid at zero angle of attack with semi-lengths of its axes given as $a=b=1$ and $c=0.1$. The coordinate system and the panel arrangement with 20 chordwise and 10 spanwise panels are shown in Figure 4.1, where cosine spacing is chosen in both directions to account for the rapid changes in the geometry and the singularity strength near the leading and trailing edges and the tip.

The analytic expression of the perturbation velocity potential on the surface of the ellipsoid is given in Lamb [16], and that of the surface velocities in the desired directions (u,v -directions in Figure 4.1) is given in Appendix C.

The chordwise potential and the u -velocity are compared with the analytic solutions in Figures 4.2 and 4.3 at four spanwise locations. The abscissa is taken as the nondimensional chordwise parameter s , which is zero at the lower trailing edge, 0.5 at the leading edge, and 1.0 at the upper trailing edge. The agreement is excellent except for the velocities at the leading and trailing edges.

Since the velocity is calculated by a difference formula from the velocity poten-

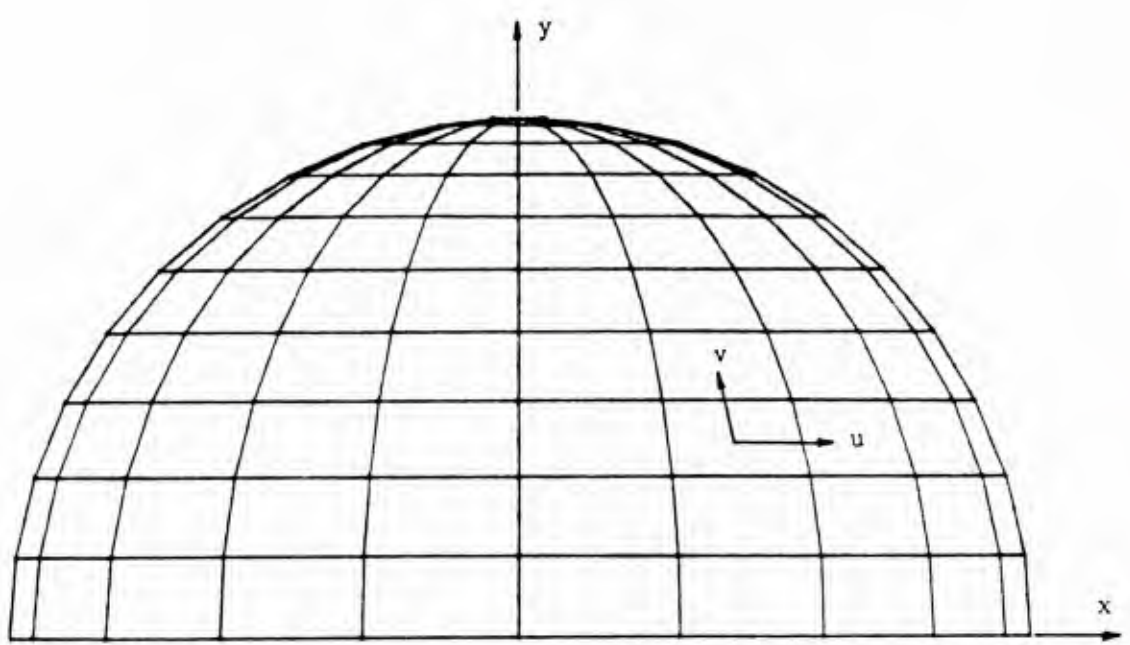


Figure 4.1: Coordinate system and panel arrangement of the ellipsoid.

tial, a small error in the potential distribution would be magnified in the velocity distribution. These magnified errors in the velocity distribution at $y/b=0.980$ are shown in Figure 4.3, but the effect of these errors is localized. The discrepancy at the leading and trailing edges is due to the error in calculating the distance between the control points, which increases near the rounded edges. This error would decrease at the trailing edge if a conventional section were chosen instead of the elliptic section. The velocity at the last panel at the trailing edge is linearly extrapolated from the previous two values.

The spanwise distribution of the potential and the v-velocity are illustrated in Figures 4.4 and 4.5 at three chordwise locations. The pressure distribution is calculated by Bernoulli's equation using the (u,v) velocities, as described in Chapter 3. Figures 4.6 and 4.7 provide a comparison of the chordwise pressure distributions by the present method with the analytic solution at four spanwise locations. Again, the agreement is excellent except for those very close to the tip.

4.2 Circular wing at finite angle of attack

The next example is a circular planform wing with an NACA four digit section at an angle of attack of 0.1 radian. Thickness effect for the wing is investigated for the cases of two different thickness/chord ratios of 0.01 and 0.05. The analytic result for the lifting circular wing with zero thickness was given by Jordan [12], which can be a standard of comparison for the present method as the thickness goes to zero.

The circular planform wing is particularly important for the propeller problem, because a magnified flow near the propeller tip is similar to the flow around the circular wing.

The coordinate system and panel arrangement are the same as those of the ellipsoid case in Figure 4.1, only the section shape is the NACA four digit series instead of the elliptic section. Both the chordwise and spanwise panelling are cosine spacing.

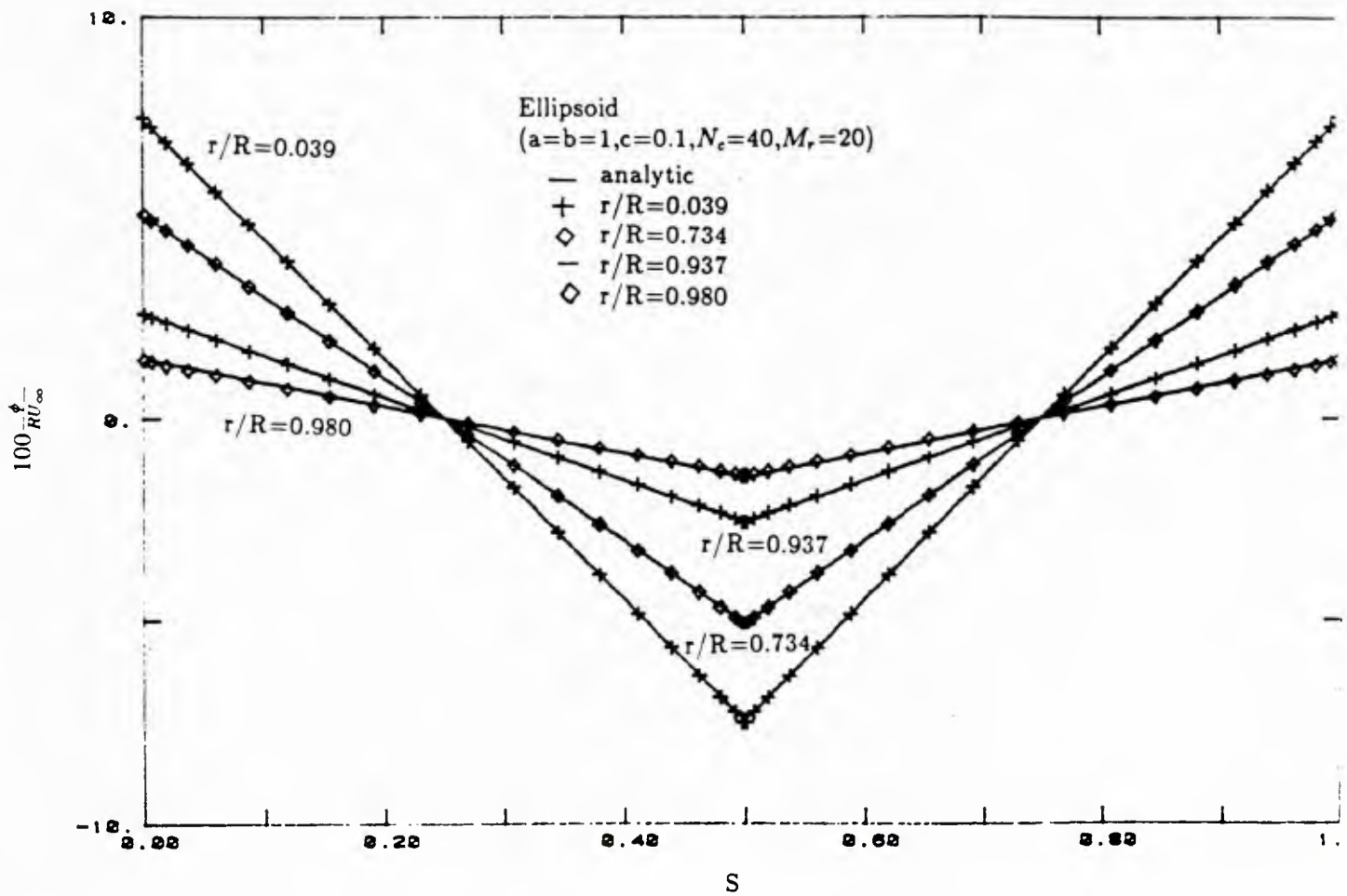


Figure 4.2: Chordwise potential distribution of the ellipsoid. ($a=b=1, c=0.1$)

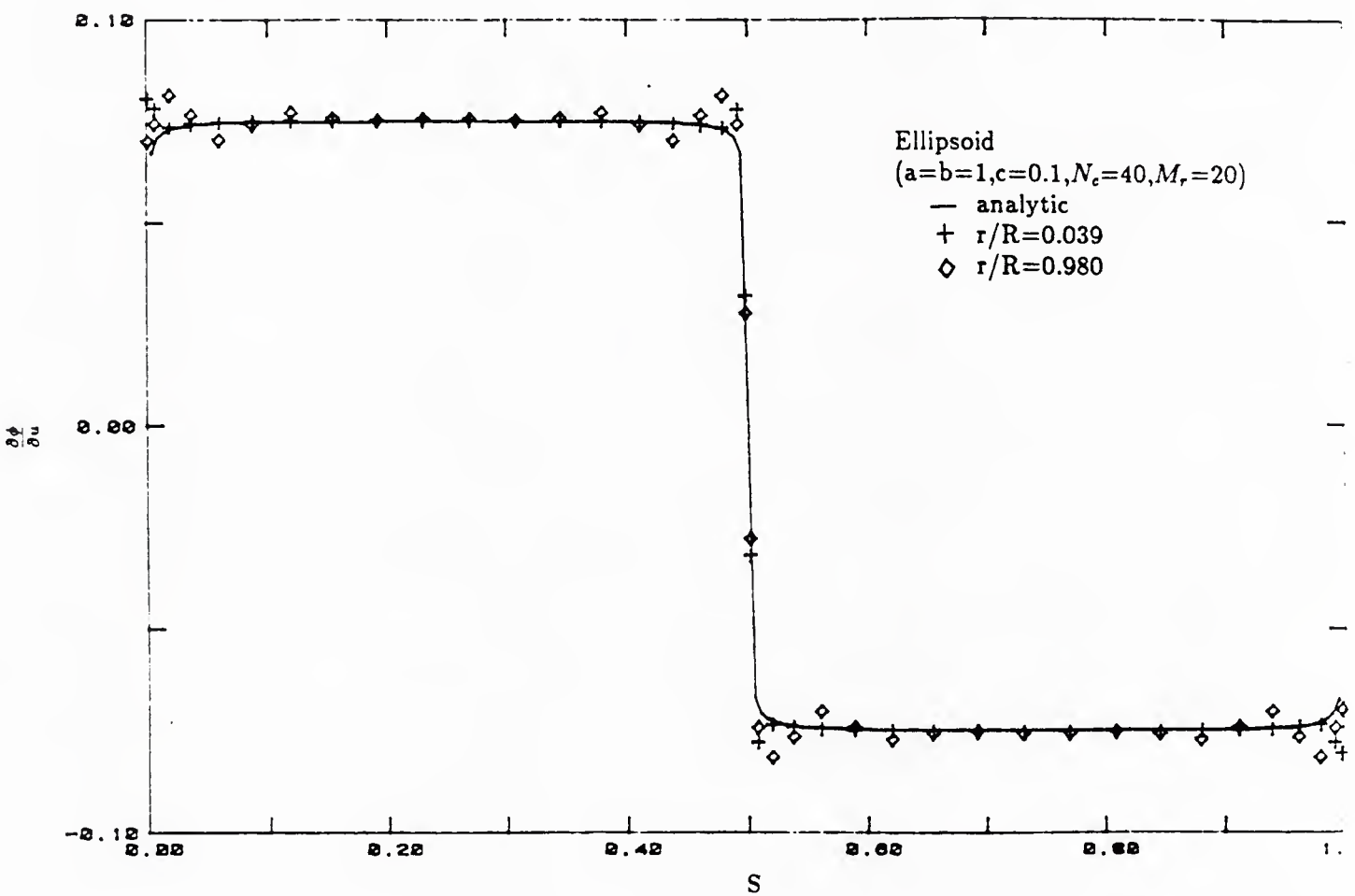


Figure 4.3: Chordwise distribution of the u -velocity component of the ellipsoid.
 $(a=b=1, c=0.1)$

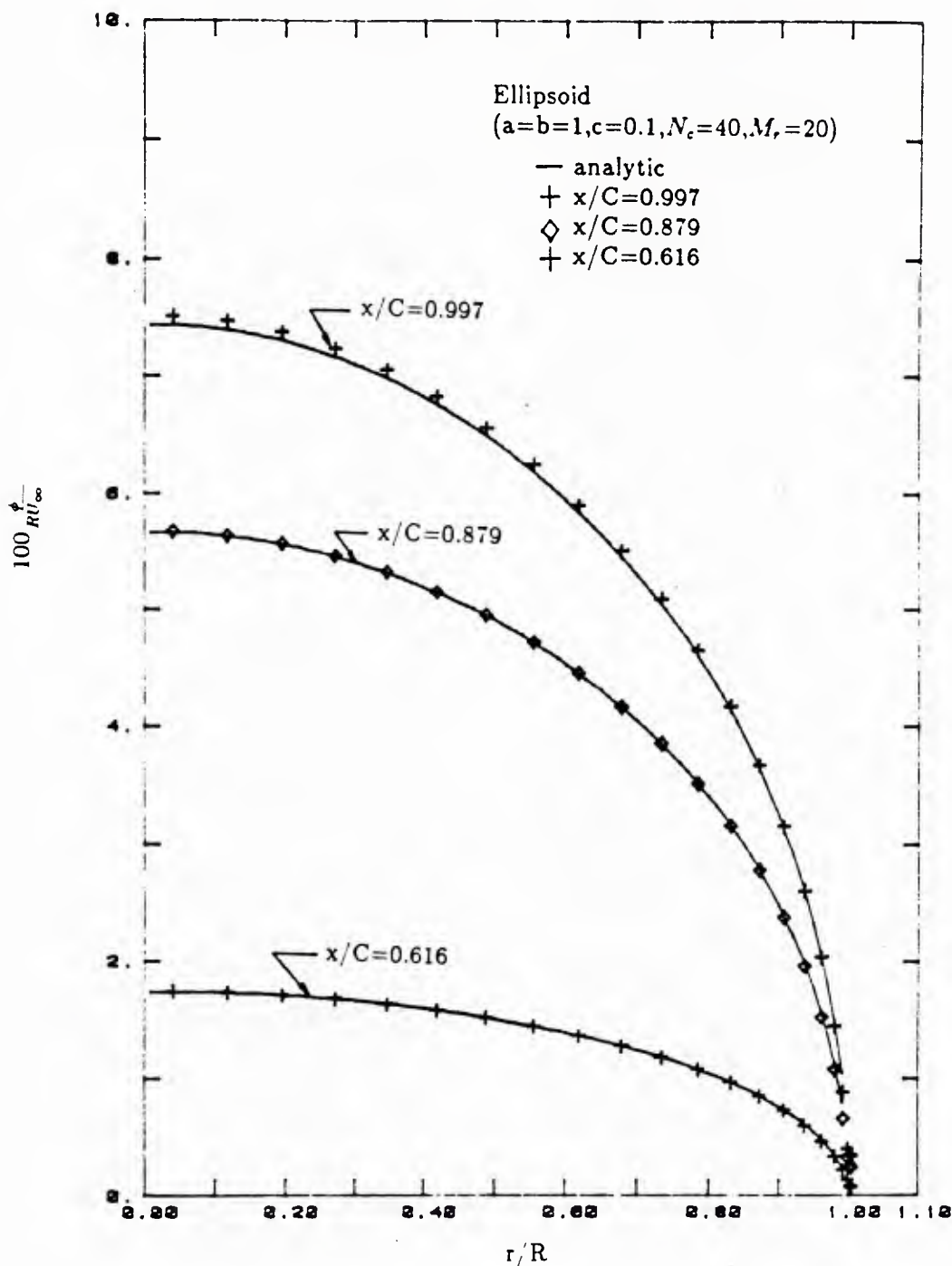


Figure 4.4: Spanwise potential distribution of the ellipsoid. ($a=b=1, c=0.1$)

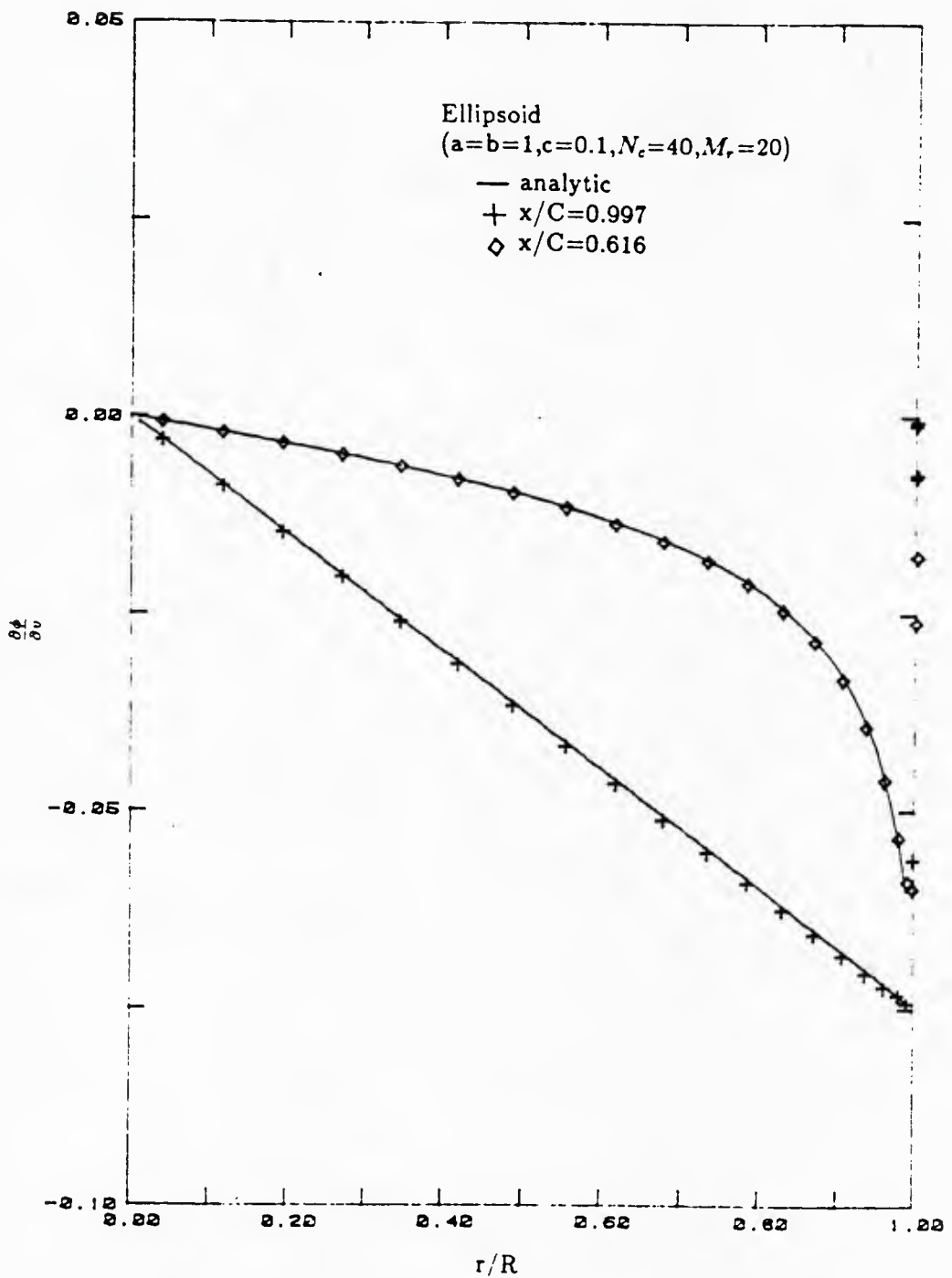


Figure 4.5: Spanwise distribution of the v -velocity component of the ellipsoid.
 $(a=b=1, c=0.1)$

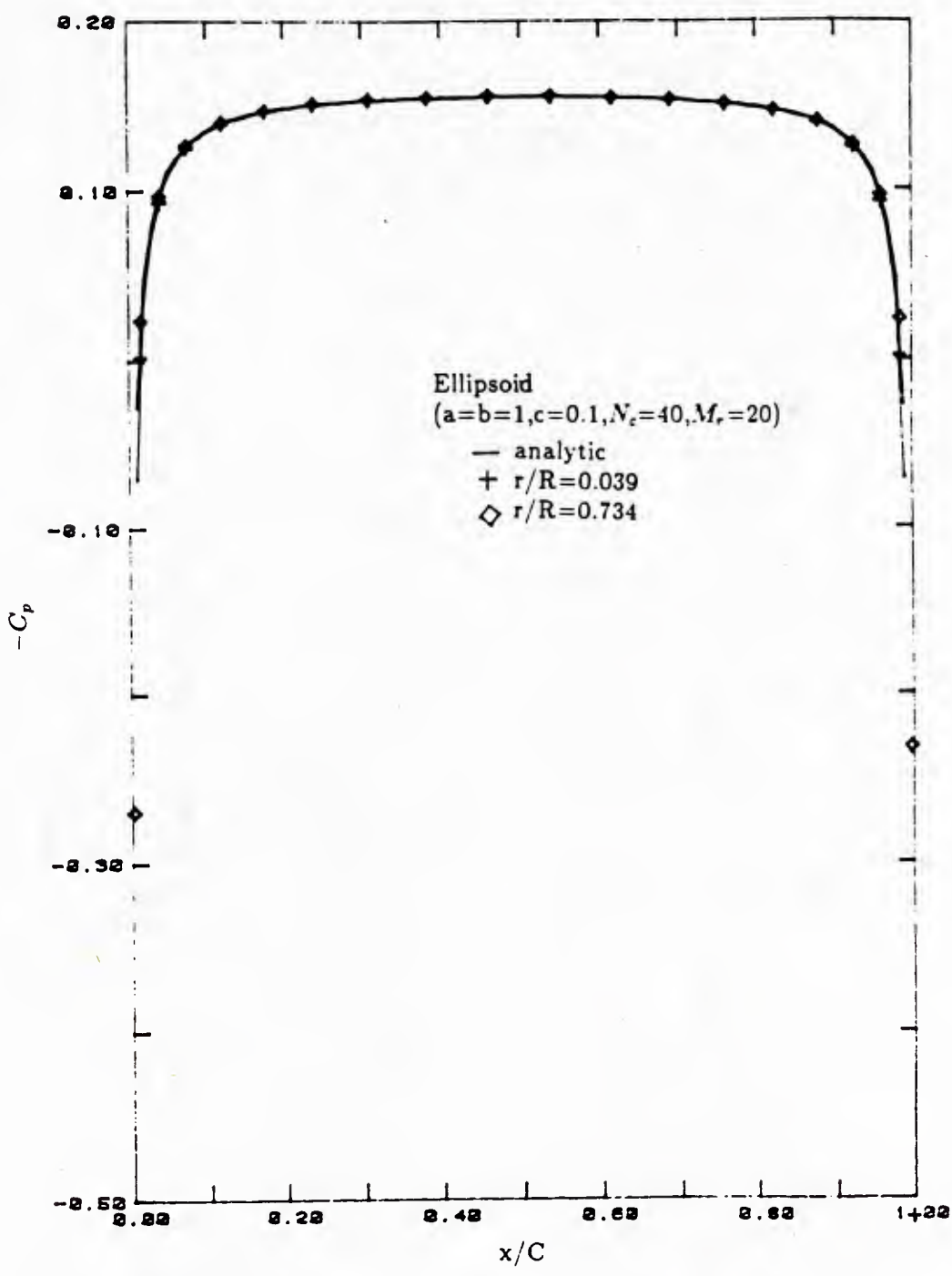


Figure 4.6: Chordwise pressure distribution of the ellipsoid. ($a=b=1, c=0.1$)

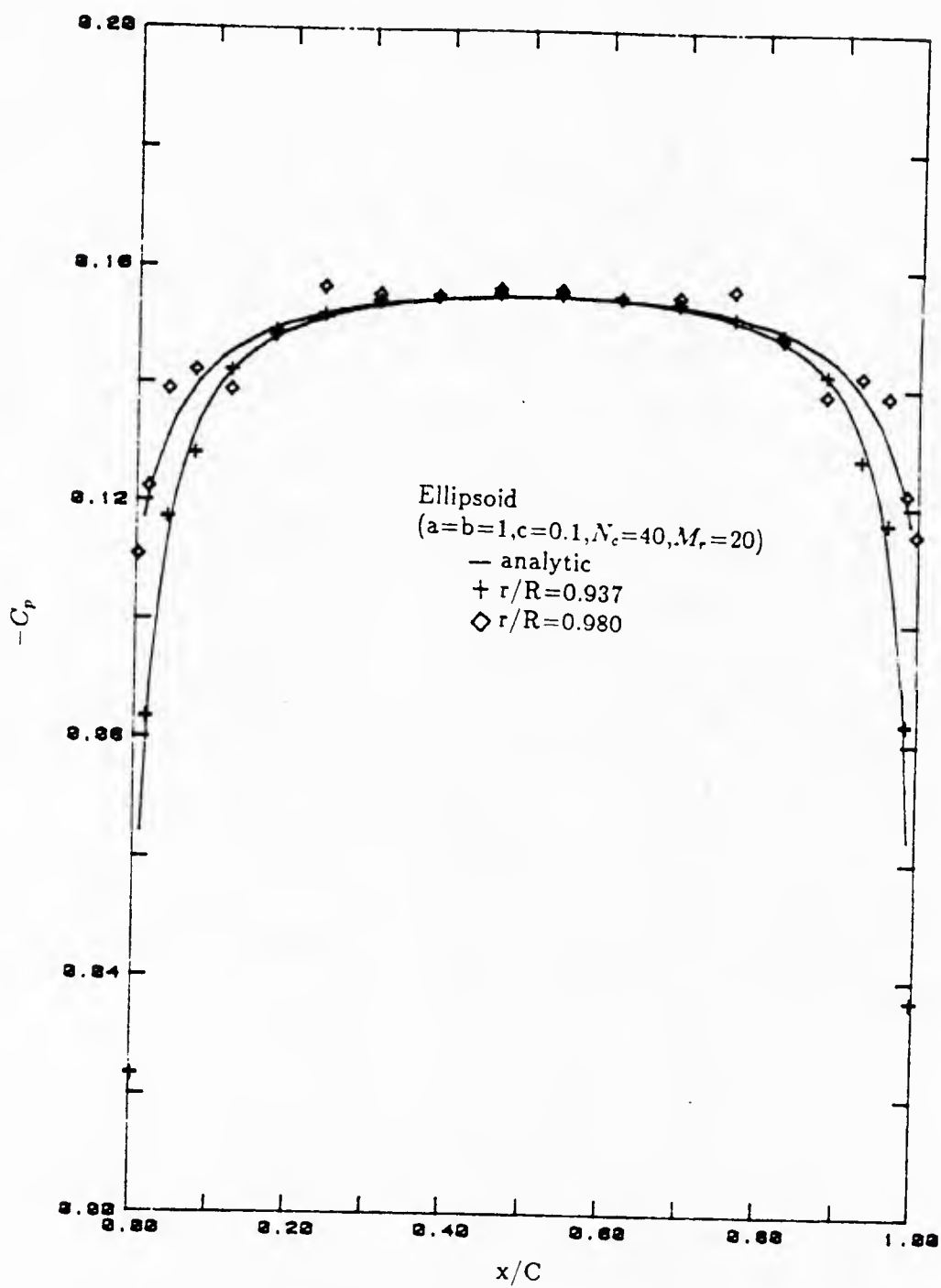


Figure 4.7: Chordwise pressure distribution of the ellipsoid. ($a=b=1, c=0.1$)

A series of computations is performed for the circular wing with an NACA 0001 section. The radial circulation distributions for varying numbers of chordwise panels (N_c) are presented in Figure 4.8 with Jordan's result for zero thickness circular wing. The effect of the number of spanwise panels (M_r) on the circulation is shown in Figure 4.9. For the circular wing case, the spanwise convergence is relatively slow compared to the chordwise convergence, which is a typical characteristic of low aspect ratio wings. The results with 40 chordwise and 40 spanwise panels are considered converged, and the calculation is performed with this number of panels hereafter.

As described in Section 3.6, the pressure Kutta condition is applied for this lifting problem. Figure 4.10 provides a comparison of the pressure distributions calculated by Morino's Kutta condition and by the pressure Kutta condition. The pressure differences between the upper and lower surfaces for the circular wing with an NACA 0001 section are shown along the chordwise panels at a radial position of $r/R=0.916$. The pressure difference at the trailing edge by Morino's Kutta condition has a positive value, which should be set to zero by the pressure Kutta condition.

The pressure difference distributions for the wing with an NACA 0005 section at the same radial location are shown in Figure 4.11. The positive loading at the trailing edge by Morino's Kutta condition is seen to be increased compared to that for the thinner section. Again, the positive loading is set to zero by the pressure Kutta condition.

The non-zero loading at the trailing edge near the tip has annoyed many researchers in this field [15],[24]. When the usual Morino's Kutta condition is applied, a positive loading at the trailing edge near the tip results for a wing with large negative sweep angles, while a negative loading results for a wing with large positive sweep angles. This can be explained as follows.

Figure 4.12 shows a magnified flow at the trailing edge near the tip for a wing with large negative sweep angles. A tip cross section profile parallel to the trailing edge

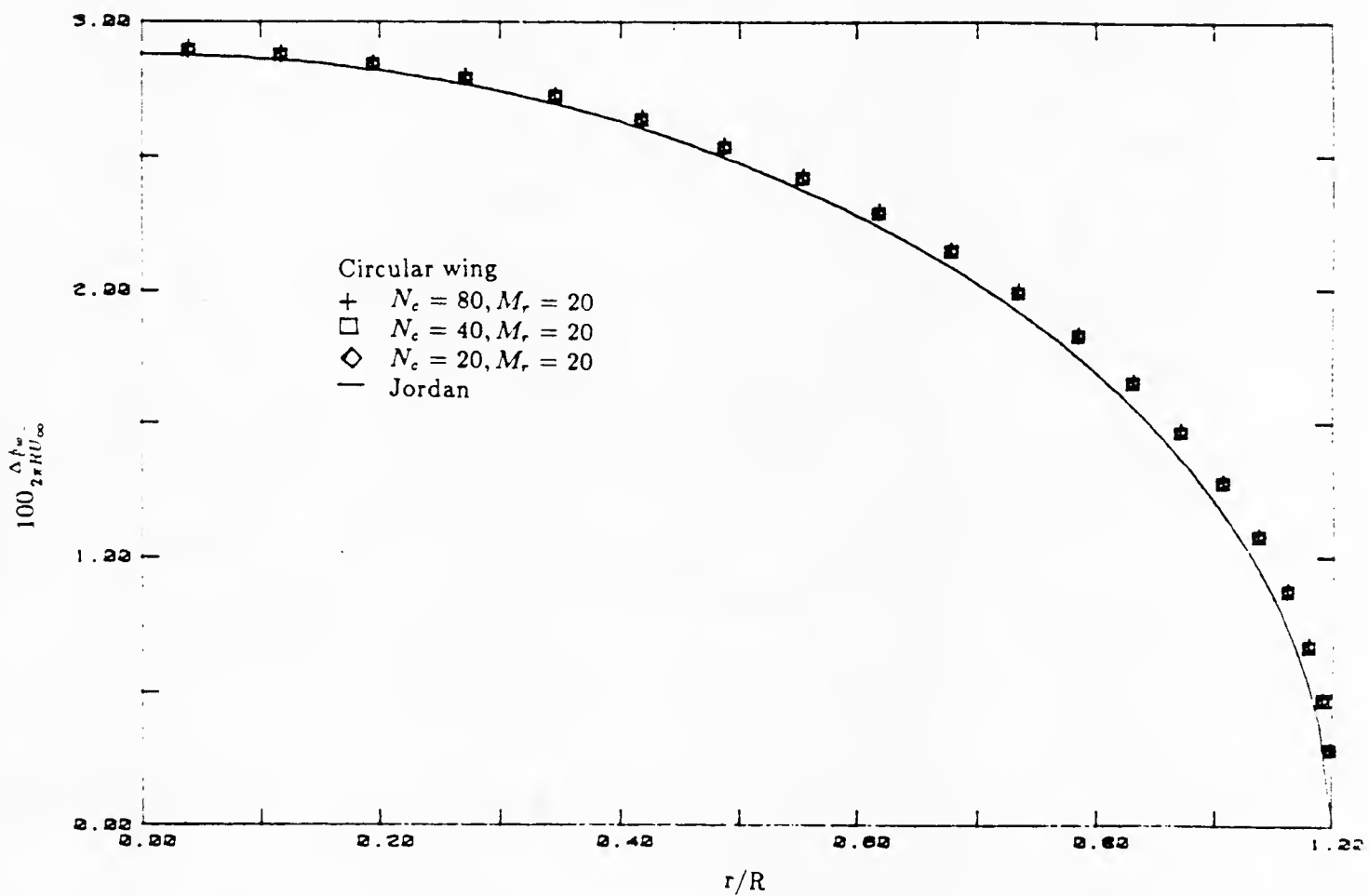


Figure 4.8: Effect of the chordwise number of panels on the circulation distribution of the circular wing. ($t/c=0.01, \alpha=5.73$ deg.)

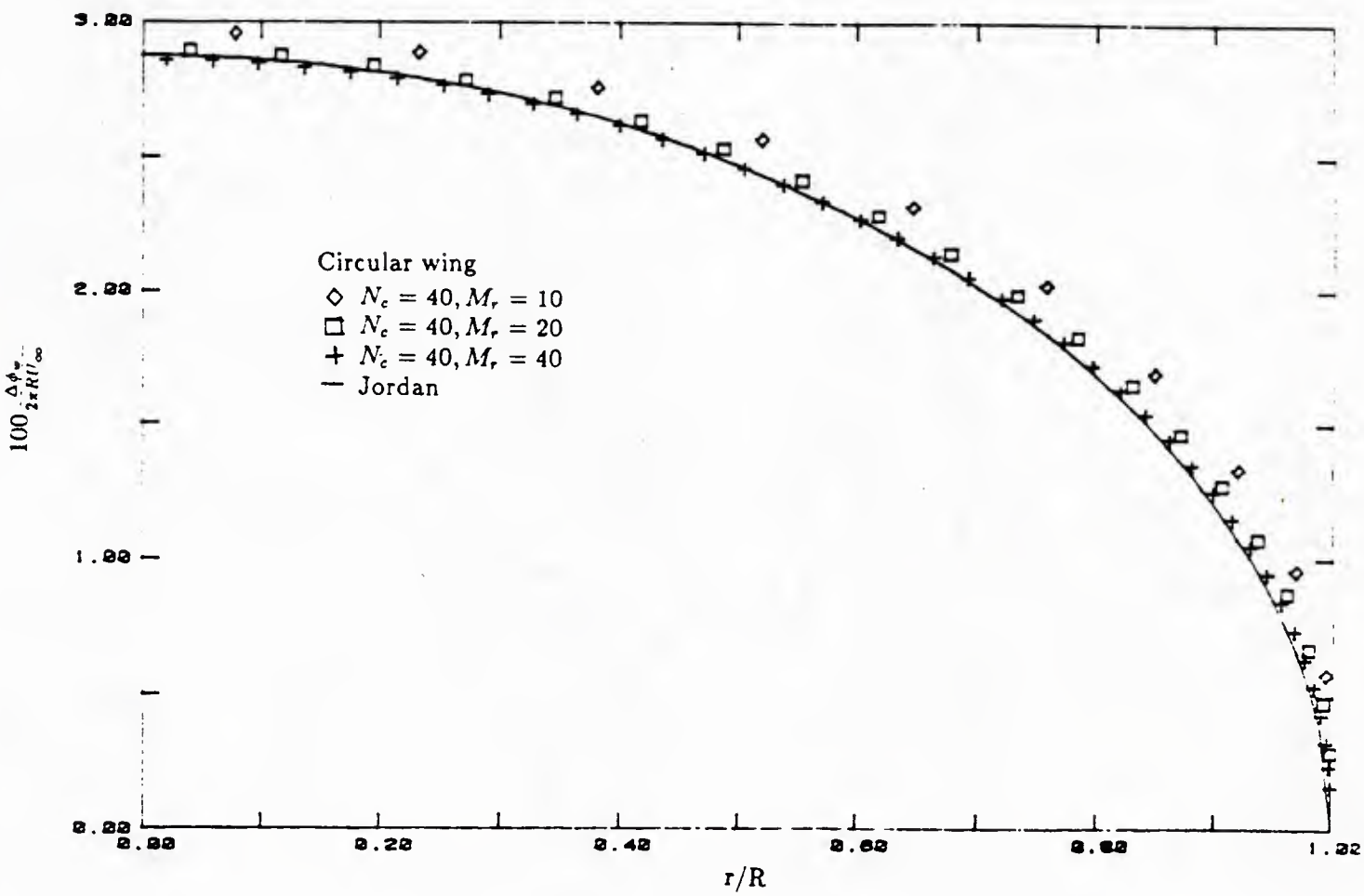


Figure 4.9: Effect of the spanwise number of panels on the circulation distribution of the circular wing. ($t/c=0.01$, $\alpha=5.73$ deg.)

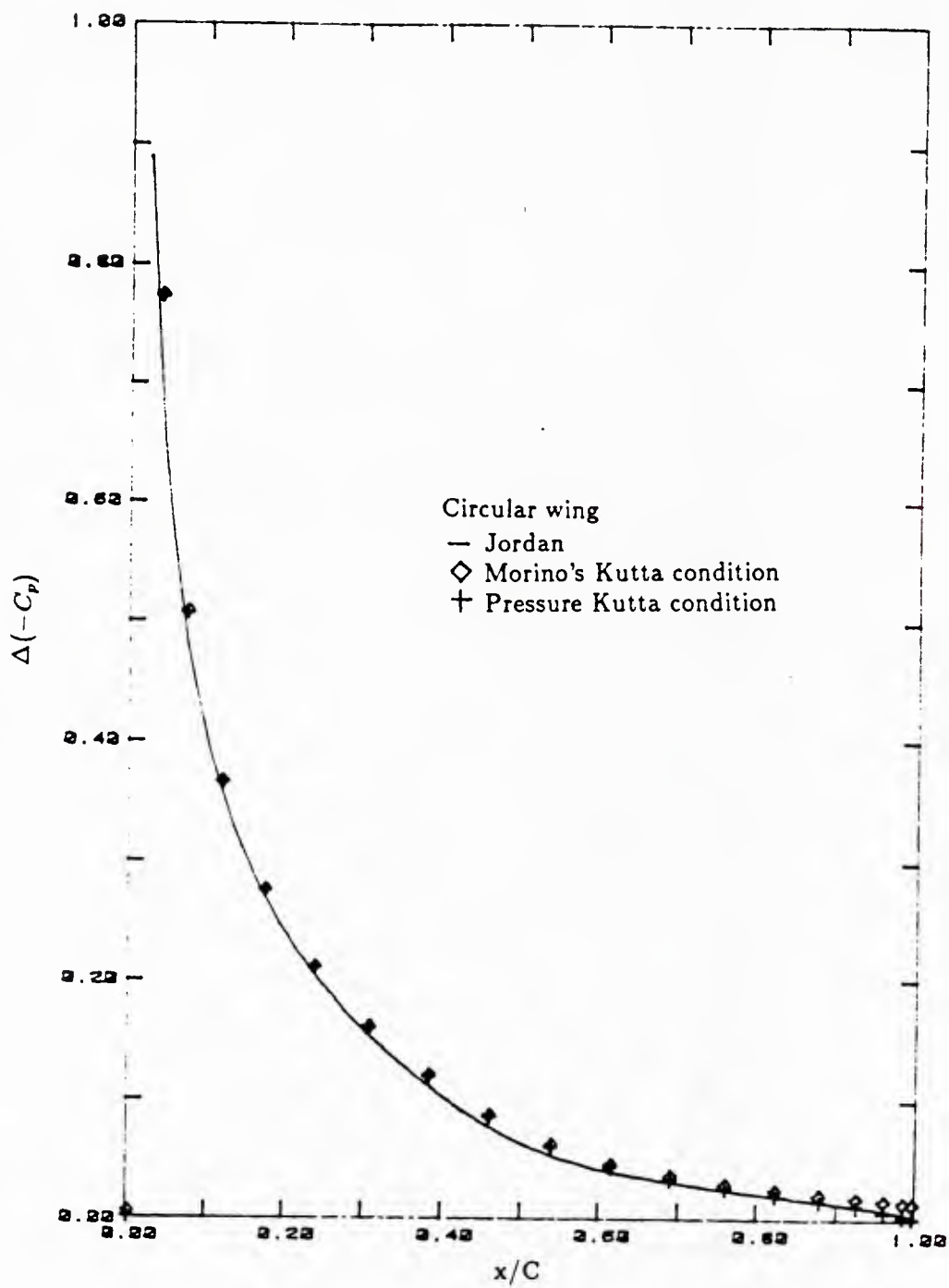


Figure 4.10: Effect of the pressure Kutta condition on the chordwise distribution of the pressure difference of the circular wing. ($t/c=0.01$, $\alpha=5.73$ deg., $r/R=0.916$)

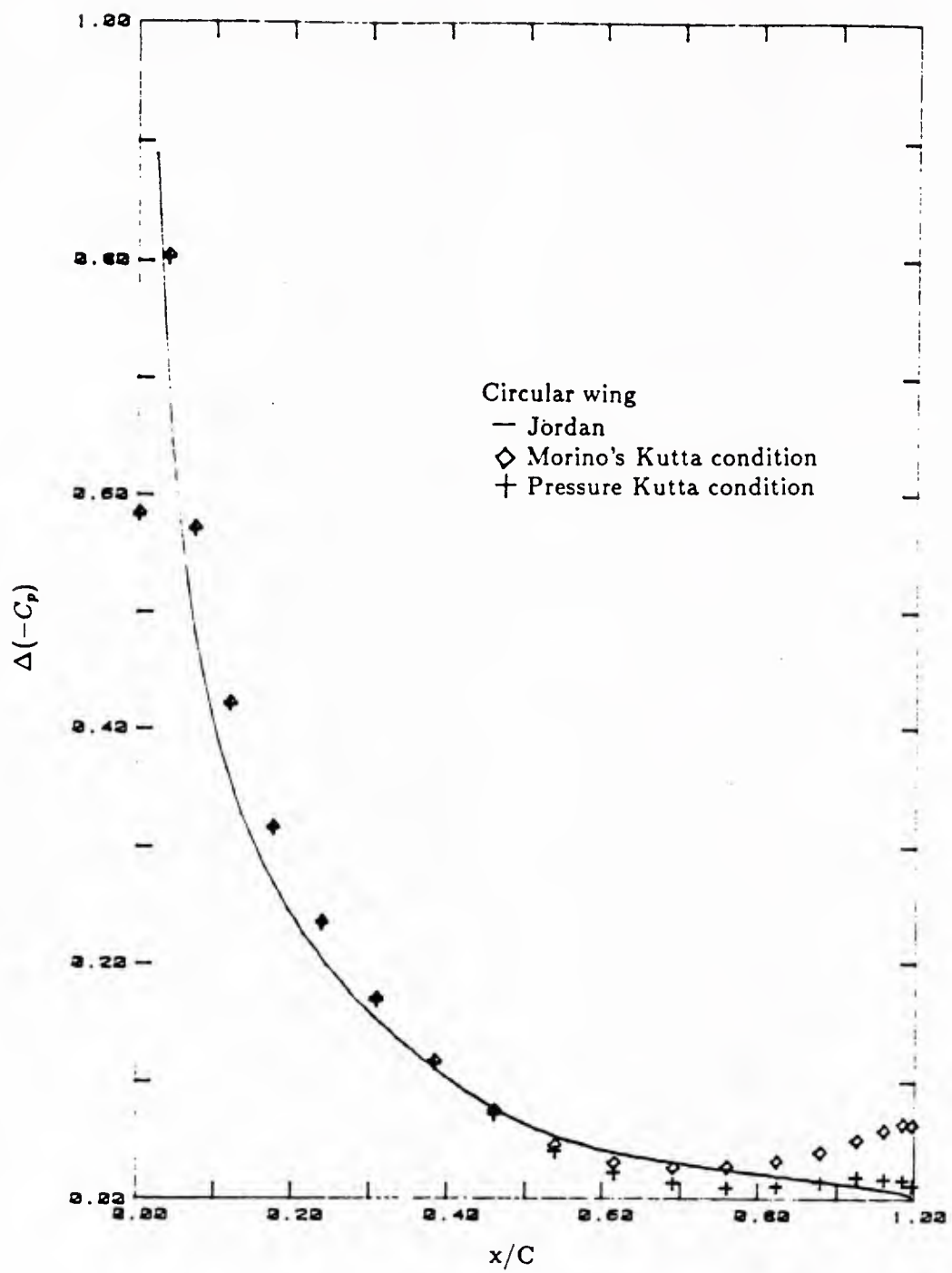


Figure 4.11: Effect of the pressure Kutta condition on the chordwise distribution of the pressure difference of the circular wing. ($t/c=0.05$, $\alpha=5.73$ deg., $r/R=0.916$)

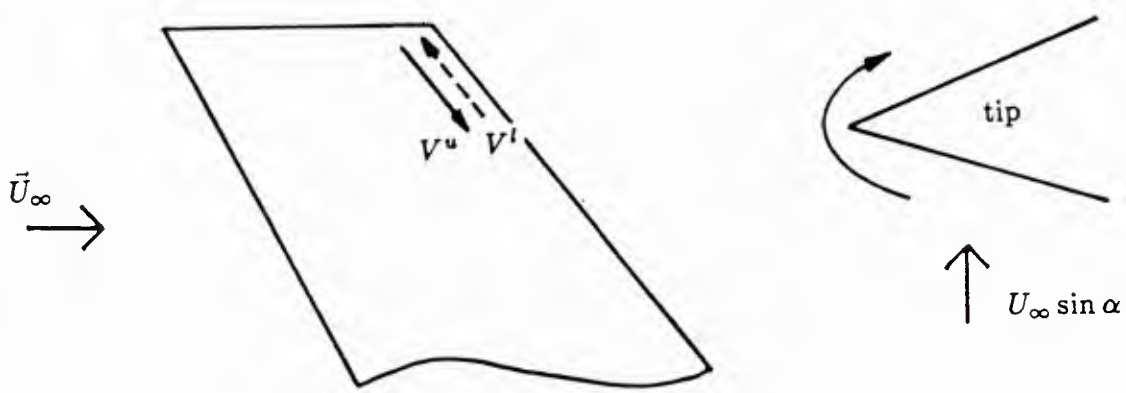


Figure 4.12: Magnified flow at the trailing edge near the tip.

is also shown. The inflow velocity can be decomposed into the x - and z -components. Due to the z -component of inflow velocity, a cross flow around the tip results, which is locally similar to the flow around a wedge. The cross flow component is outboard on the lower surface and inboard on the upper surface. The magnitude of the cross flow velocity becomes larger for a thicker section.

The cross flow is added to the x -component inflow velocity. With a negative sweep angle, the magnitude of the resulting velocity on the upper surface is larger than that on the lower surface, which results in positive loading at the trailing edge near the tip. Since the trailing edge region of the circular wing toward the tip is geometrically similar to a wing with negative sweep angles, the loading distribution there behaves similar to the negative sweep case. For the case of a wing with large positive sweep angles, the situation is reversed and negative loading at the trailing edge results.

If a wake alignment scheme were adopted, the trailing vortex wake would leave the

trailing edge in the mean direction of velocities on the upper and lower surfaces, and the trailing wake would contract for the negative sweep case. Since the contraction of the wake would increase the downwash velocities at the control points in the inner radii of the trailing vortex, a fully aligned wake model would alleviate the positive loading at the trailing edge. The frozen wake model in the present method does not account for the wake contraction. Only the positive loading should be set to zero by the pressure Kutta condition.

As the thickness of the circular wing increases, the magnitude of the cross flow component increases and the positive loading at the trailing edge with Morino's Kutta condition increases. In order to satisfy the pressure Kutta condition, the dipole strength in the wake is reduced during the iteration process. As a result, circulation is reduced as the thickness is increased, which contradicts the trend for two-dimensional cases. This trend is shown in Figure 4.13, where the radial circulation distributions are illustrated for the wing with NACA 0001 and NACA 0005 sections.

Figures 4.14 through 4.17 show the chordwise distributions of the pressure difference at four different spanwise locations. Here the results for thickness/chord ratios of 0.01 and 0.05 are plotted with Jordan's result for the zero thickness circular wing. As one can see, the result of the 0.01 thickness-chord ratio wing agrees very well with Jordan's result. This indicates the robustness of the present method even for the very thin wing. Positive loading is shown near the trailing edge toward the tip for the wing with the NACA 0005 section. This would decrease if a he contraction model for the trailing wake were adopted.

4.3 Rectangular wings with different sweep angles

The next example is chosen to study the effect of sweep angles on the performance of rectangular wings. A series of computations is made for wings with 5.9 aspect ratio, 8 degree incidence, and varying sweep angles of -45, 0 and +45 degrees. For each

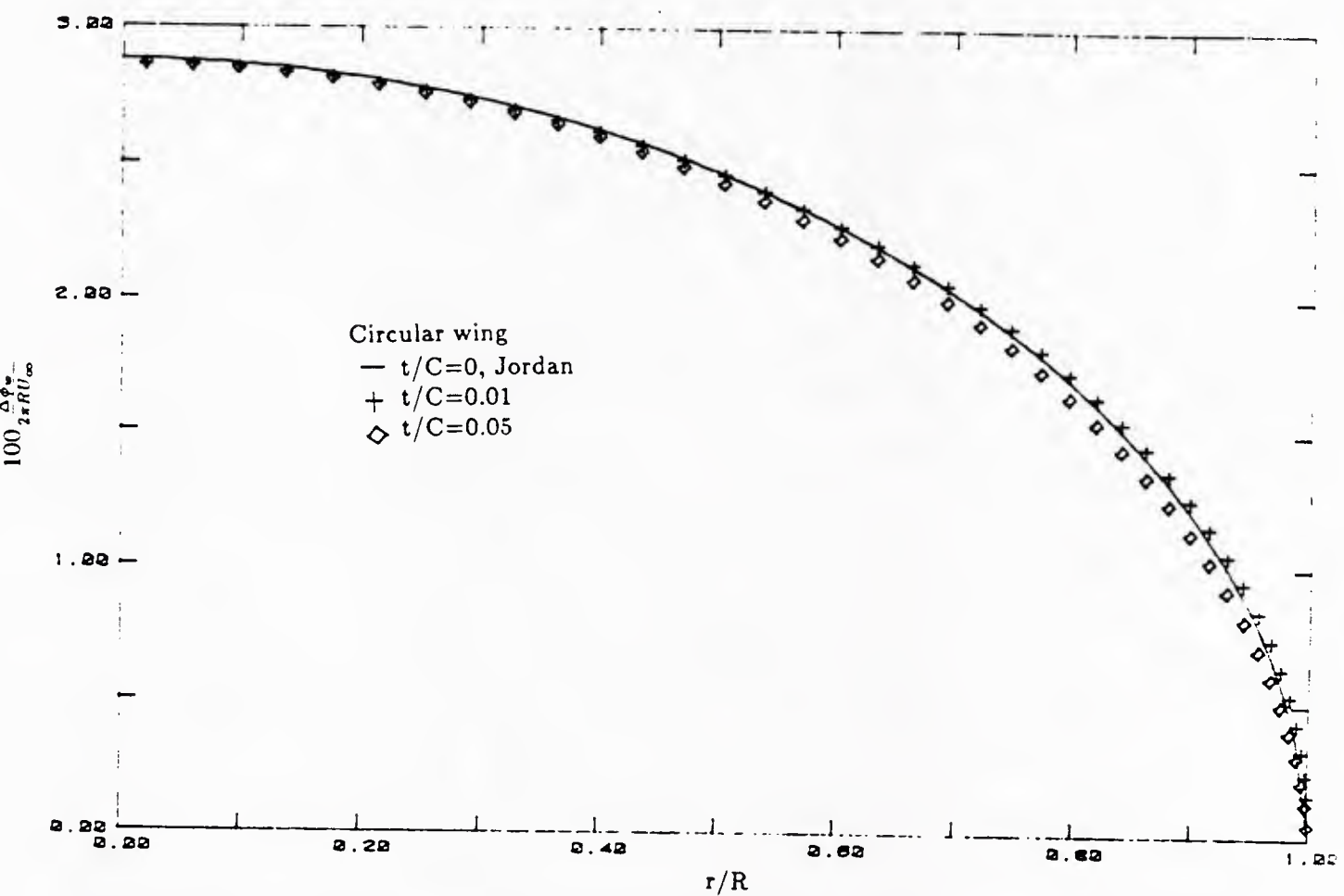


Figure 4.13: Thickness effect on the radial circulation distribution of the circular wing. ($\alpha=5.73$ deg.)

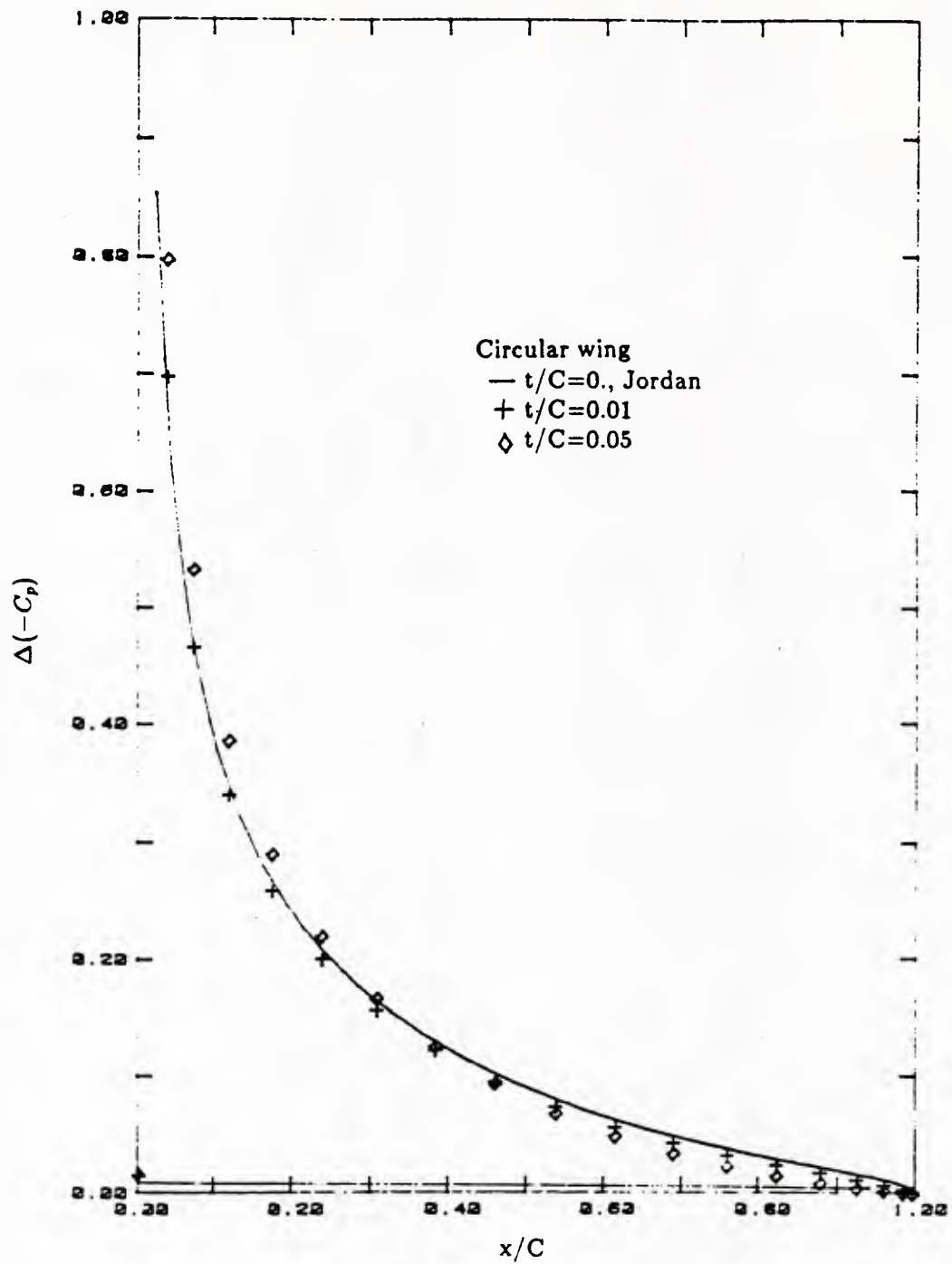


Figure 4.14: Chordwise distribution of the pressure difference of the circular wing at $r/R=0.098$.

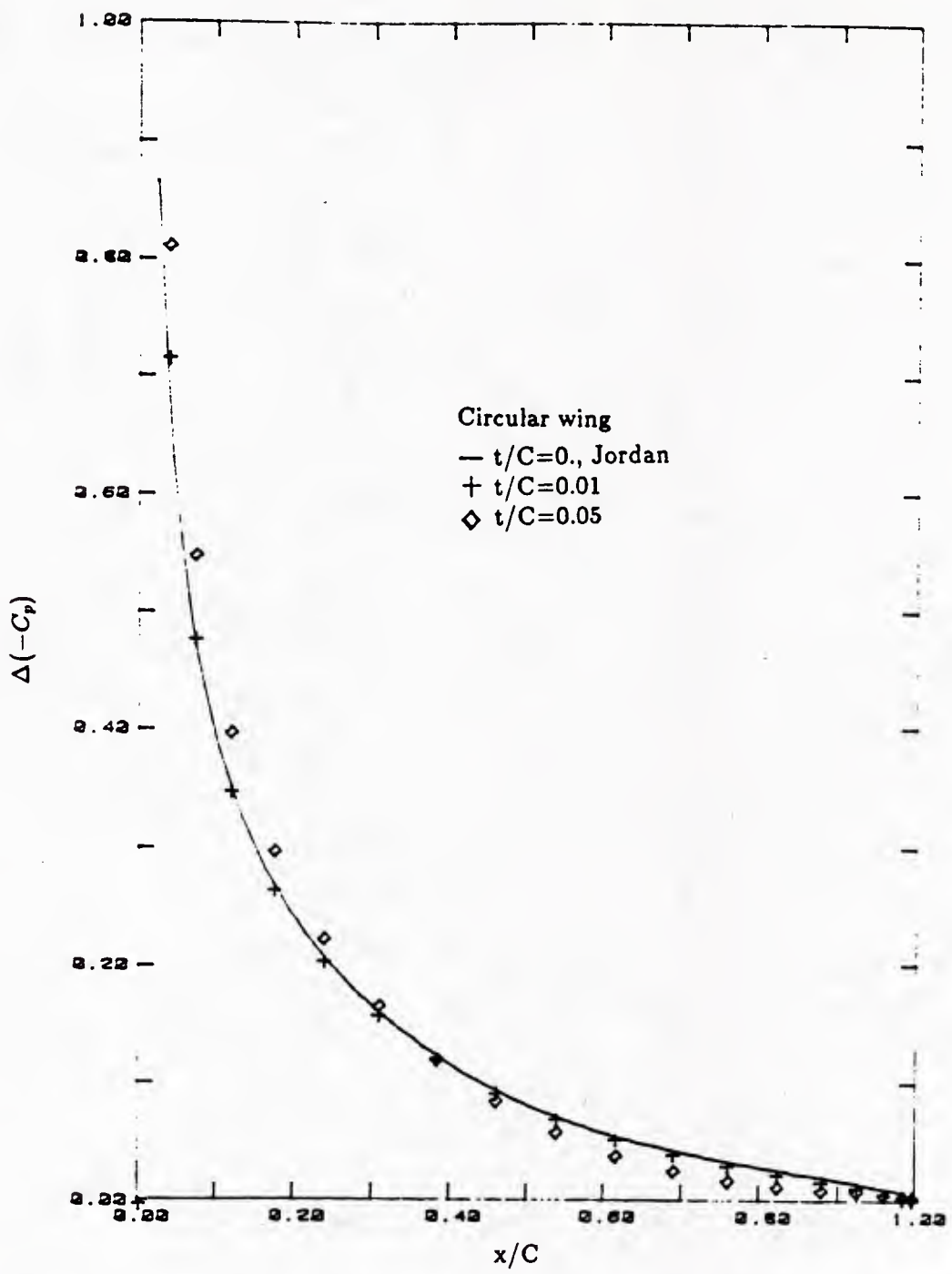


Figure 4.15: Chordwise distribution of the pressure difference of the circular wing at $r/R=0.693$.

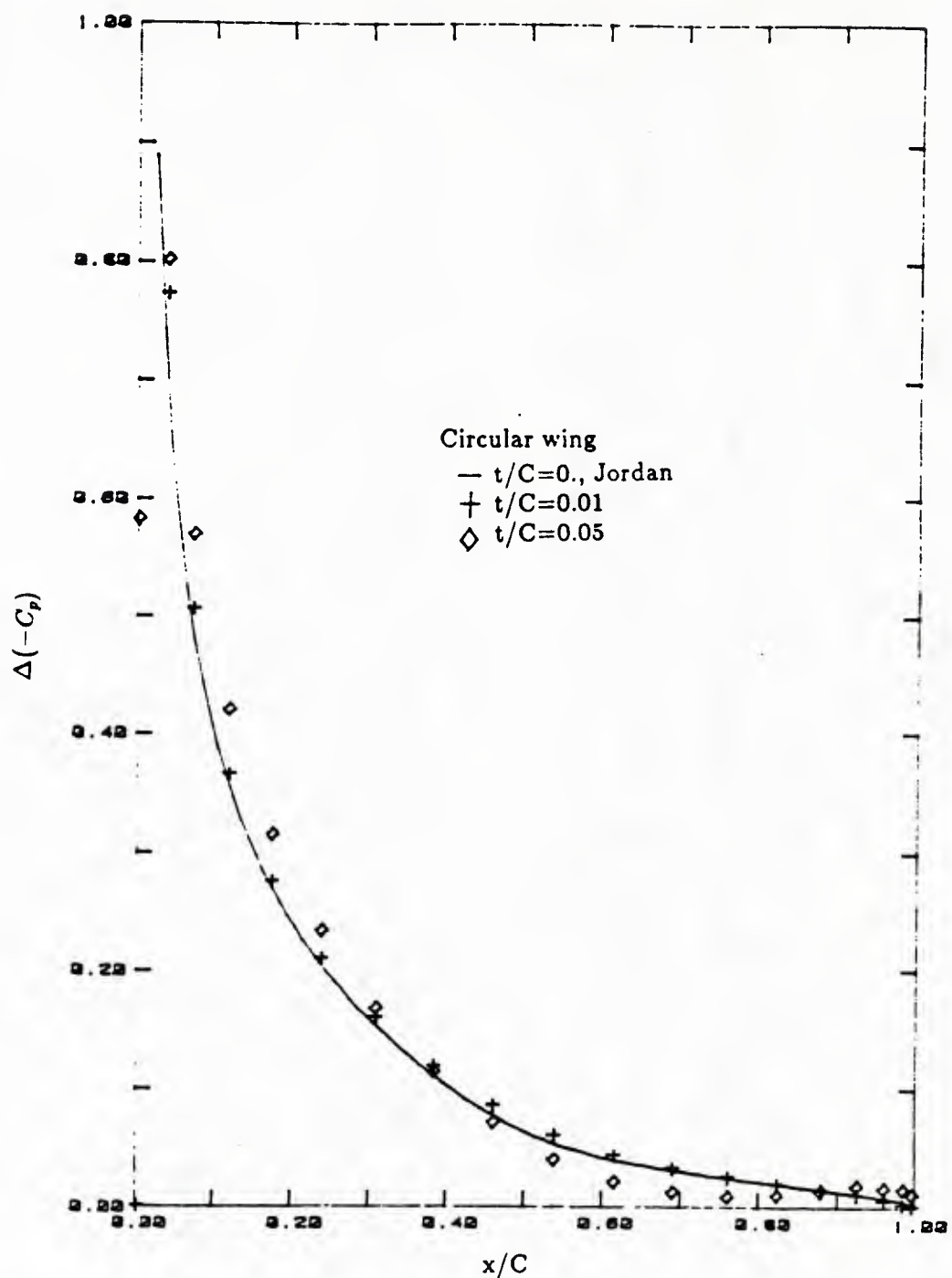


Figure 4.16: Chordwise distribution of the pressure difference of the circular wing at $r/R=0.916$.

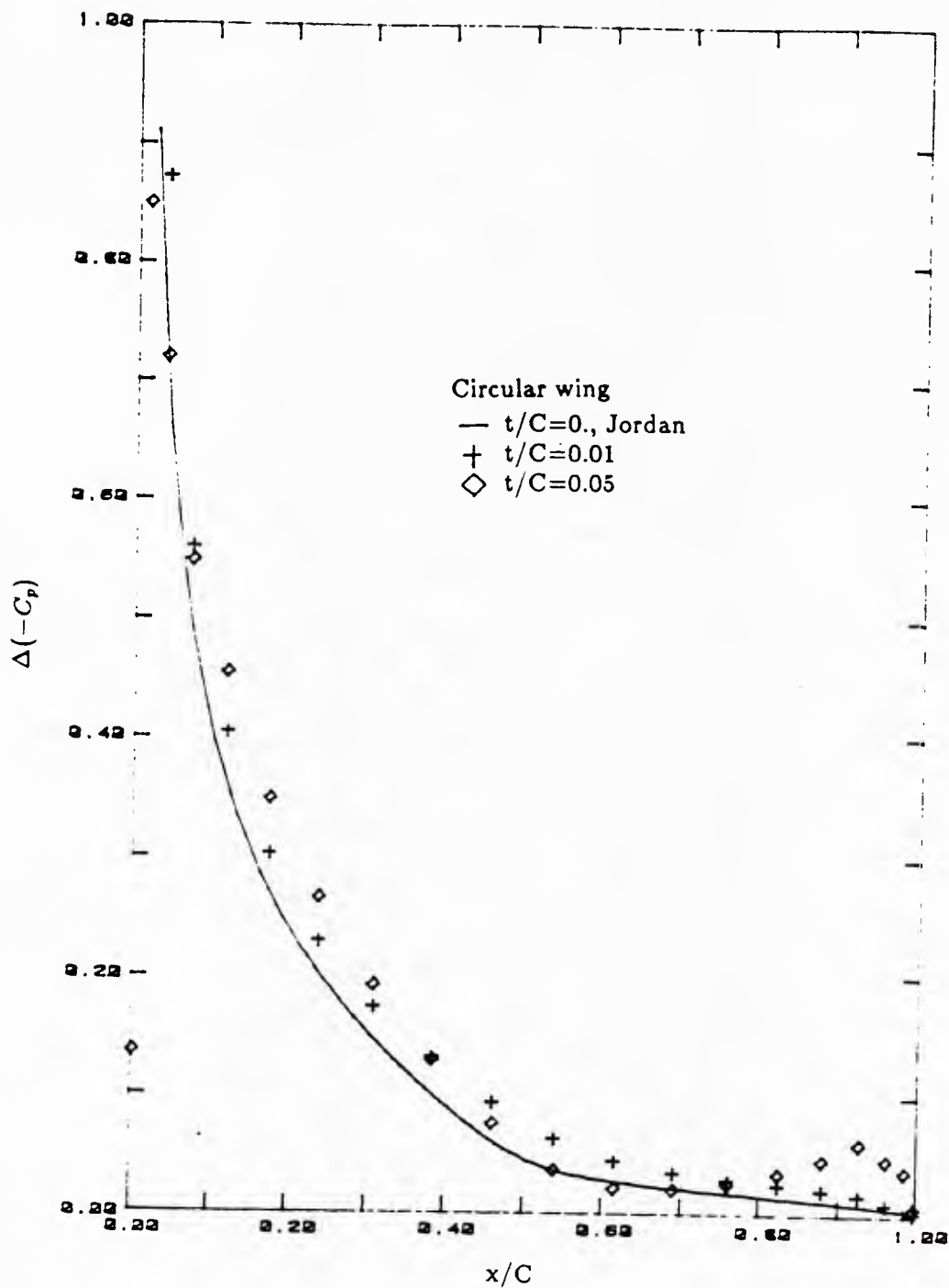


Figure 4.17: Chordwise distribution of the pressure difference of the circular wing at $r/R=0.977$.

wing, the thickness effect is illustrated with the results of the wings with NACA 0001, NACA 0005 and NACA 0012 sections.

The panel arrangements for the wings with three different sweep angles are shown in Figure 4.18. Here again, cosine spacing is adopted to account for the rapid change of the singularity strength near the leading and trailing edges and the tip.

A convergence test is performed for the unswept wing with an NACA 0012 section. The influence of number of panels on circulation is illustrated in Figures 4.19 and 4.20. The solid line in both figures is the result with 80 chordwise and 20 spanwise panels, which is considered as converged. The chordwise convergence is shown to be slower than the spanwise convergence for this relatively high aspect ratio wing. For a low aspect ratio wing, the convergence characteristic would be opposite, as shown in the previous example of the circular wing. Since the result with 40 chordwise and 10 spanwise panels is reasonably accurate and requires much less computing time, computation is made with this number of panels unless otherwise mentioned.

The force calculation can be done either by integration of the element pressure on each panel, or by considering the energy far downstream, which is the so-called Trefftz plane wake integration method. The lift and drag coefficients calculated by both methods are shown in Table 4.1, for the rectangular wing with aspect ratio 5.9, with an NACA 0012 section at 8 degree incidence. N_c represents the number of panels along the chordwise strip in the wing, while M_r represents the number of radial strips. The forces calculated by both methods converge to common values as the number of panels increases. Again the result using 40 chordwise and 10 spanwise panels is reasonably accurate. The pressure integration method is preferred because of its direct physical interpretation.

The thickness effect for the unswept wing is illustrated in Figure 4.21. For this unswept wing, the circulation is increased as the thickness is increased, which is the same trend as in the two-dimensional case.

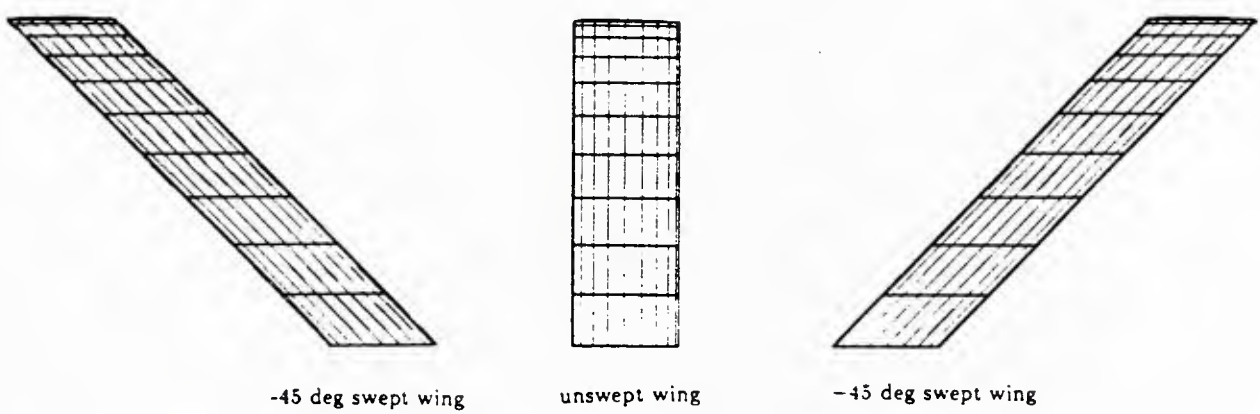


Figure 4.18: Panel arrangements of the rectangular wings with -45, 0, and +45 degree sweep angles. (Aspect ratio=5.9, t/c =0.01, 0.05 and 0.12, $\alpha=8$ deg.)

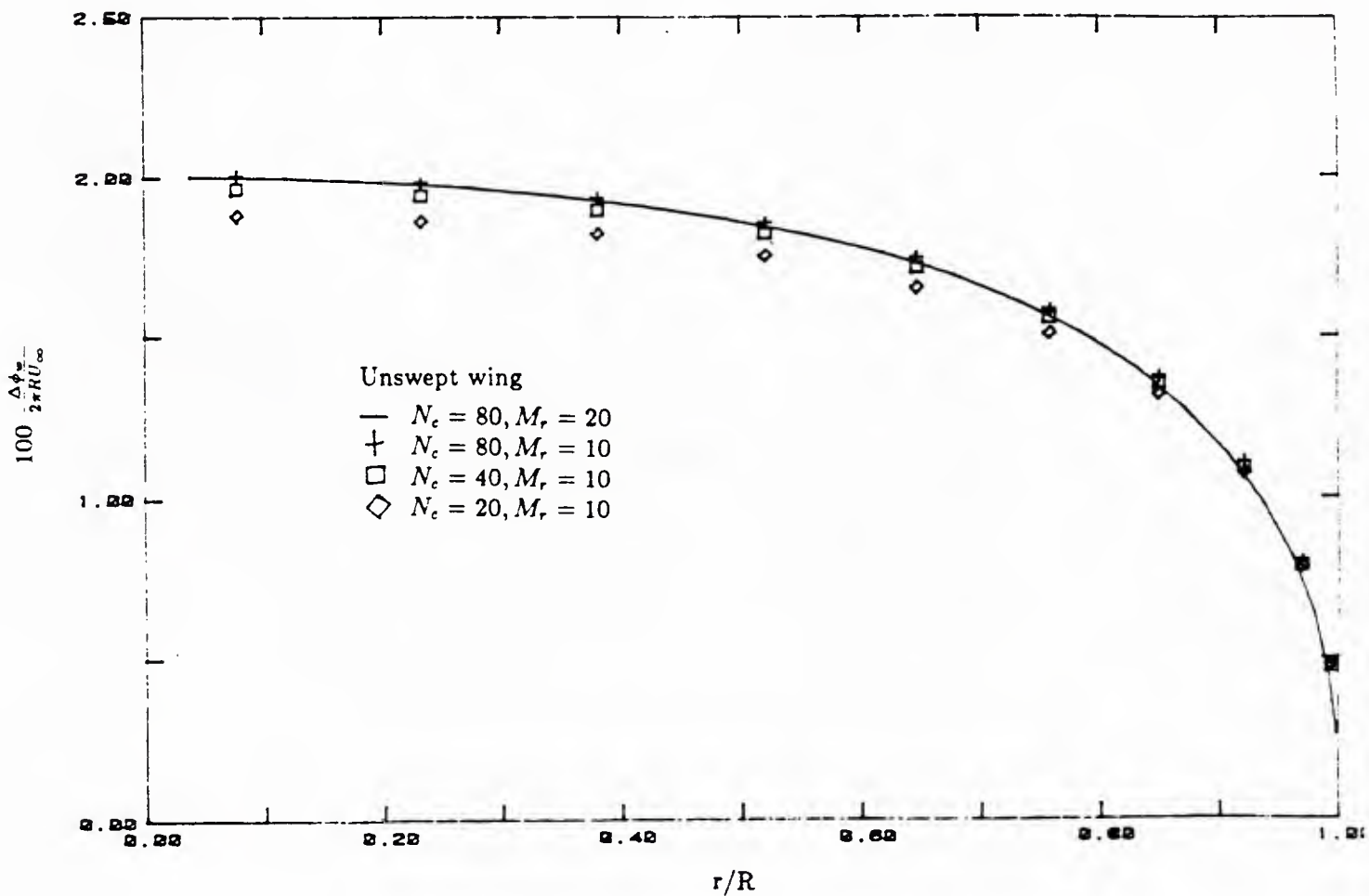


Figure 4.19: Effect of the chordwise number of panels on the circulation distribution of the unswept rectangular wing. (Aspect ratio=5.9, $t/c=0.12$, $\alpha=8$ deg.)

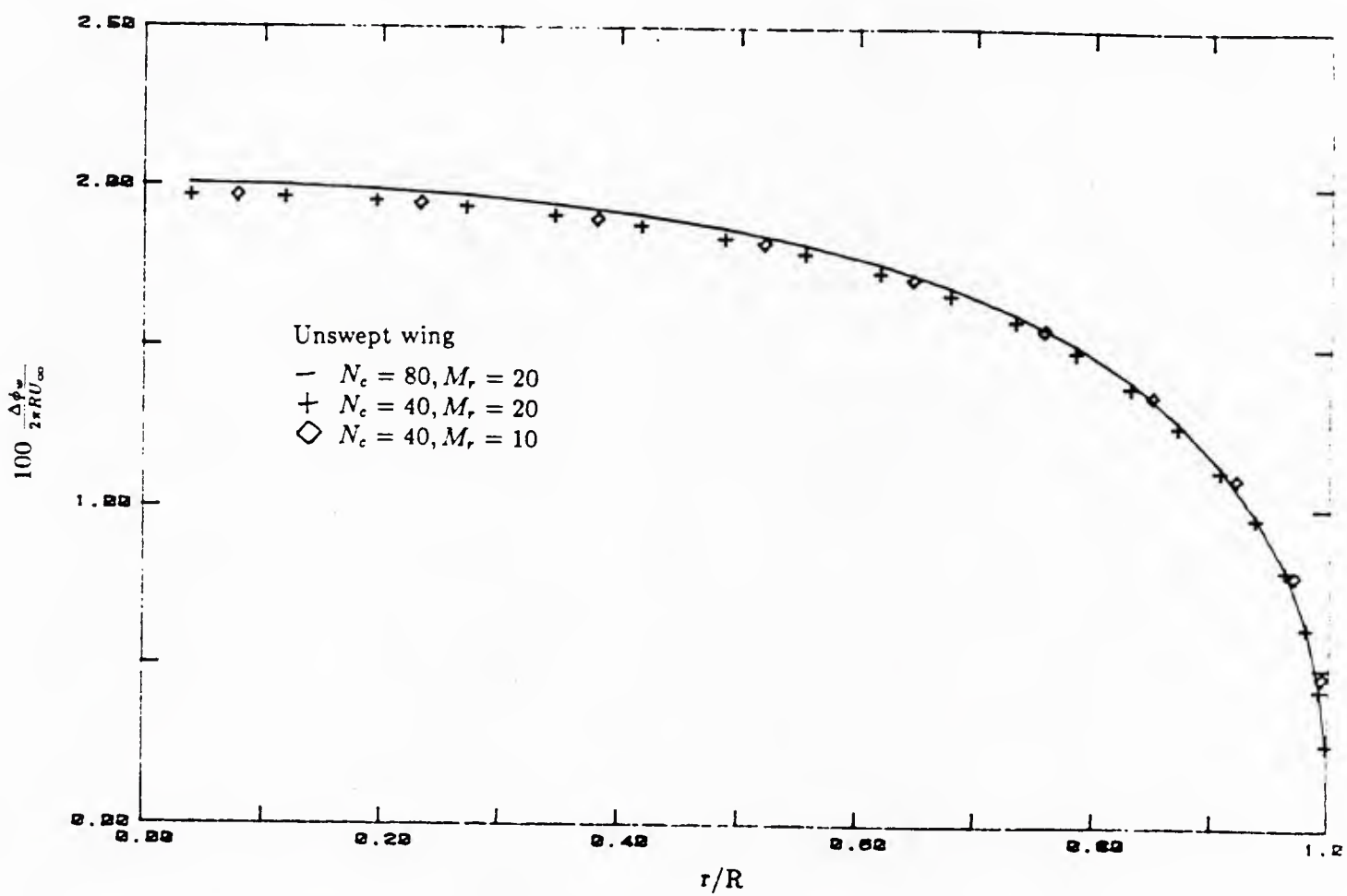


Figure 4.20: Effect of the spanwise number of panels on the circulation distribution of the unswept rectangular wing. (Aspect ratio=5.9, $t/c=0.12$, $\alpha=8$ deg.)

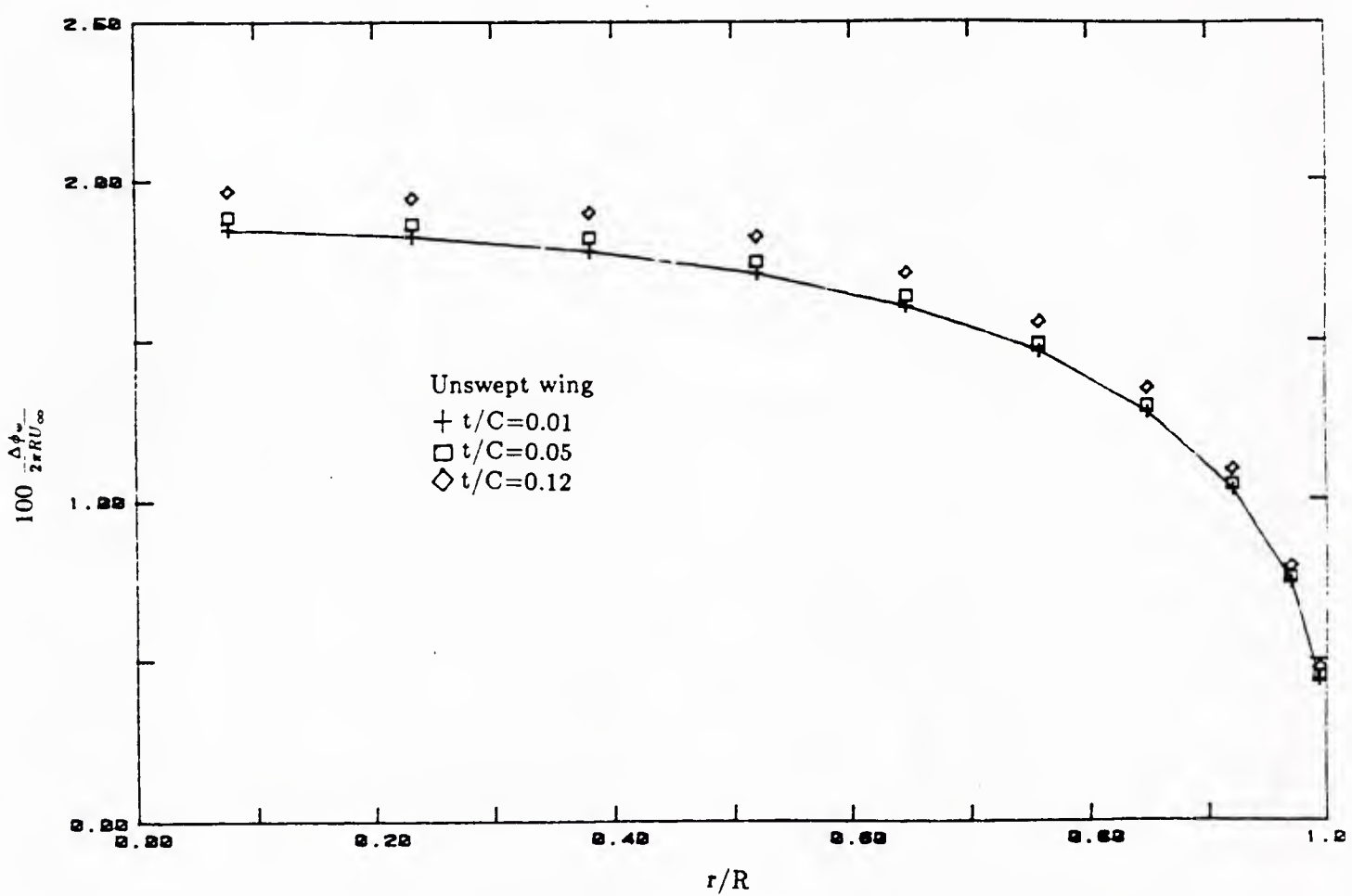


Figure 4.21: Effect of the thickness on the spanwise circulation of the unswept wing.
(Aspect ratio=5.9, $\alpha=8$ deg.)

Table 4.1: Effect of the number of panels on the lift and drag coefficients of the unswept rectangular wing. (Aspect ratio=5.9, $t/c=0.12$, $\alpha=8$ deg.)

N_c	M_r	$(C_L)_{press}$	$(C_L)_{trefftz}$	$(C_D)_{press}$	$(C_D)_{trefftz}$
20	10	0.426	0.410	0.0189	0.0145
40	10	0.429	0.426	0.0165	0.0154
80	10	0.432	0.434	0.0161	0.0160
40	20	0.424	0.422	0.0160	0.0148
80	20	0.427	0.429	0.0154	0.0152

The pressure difference between the upper and lower surfaces is shown in Figures 4.22 and 4.23 at three different spanwise locations, for thickness/chord ratios of 0.05 and 0.12 respectively. The thickness effect is apparent near the leading edge where a finite pressure peak is shown. The ability to calculate the pressure peak is one of the major advantages of the present method over the lifting surface theory.

As explained in Section 3.6, not only the pressure Kutta condition but also the compatibility condition should be satisfied at the trailing edge. Hirschel et. al. [11] claimed that a low order panel method, such as the present method, does not satisfy the compatibility condition near the tip. The radial vorticity distributions calculated by the difference of the cross flow velocities between the upper and lower surfaces are plotted with those calculated by the spline differentiation of the circulation in figures 4.24 and 4.25, for the unswept wings with NACA 0005 and NACA 0012 sections. The agreement is clearly shown, and the compatibility is satisfied. The satisfaction of the compatibility condition shows the self consistency of the present method.

The effect of thickness for the rectangular wing with -45 degree sweep angle is illustrated in Figure 4.26, where the distributions of the radial circulation are given for the varying thickness/chord ratios of 0.01, 0.05 and 0.12. Since the induced downwash due to the trailing wake is large toward the tip compared to the rectangular wing, the

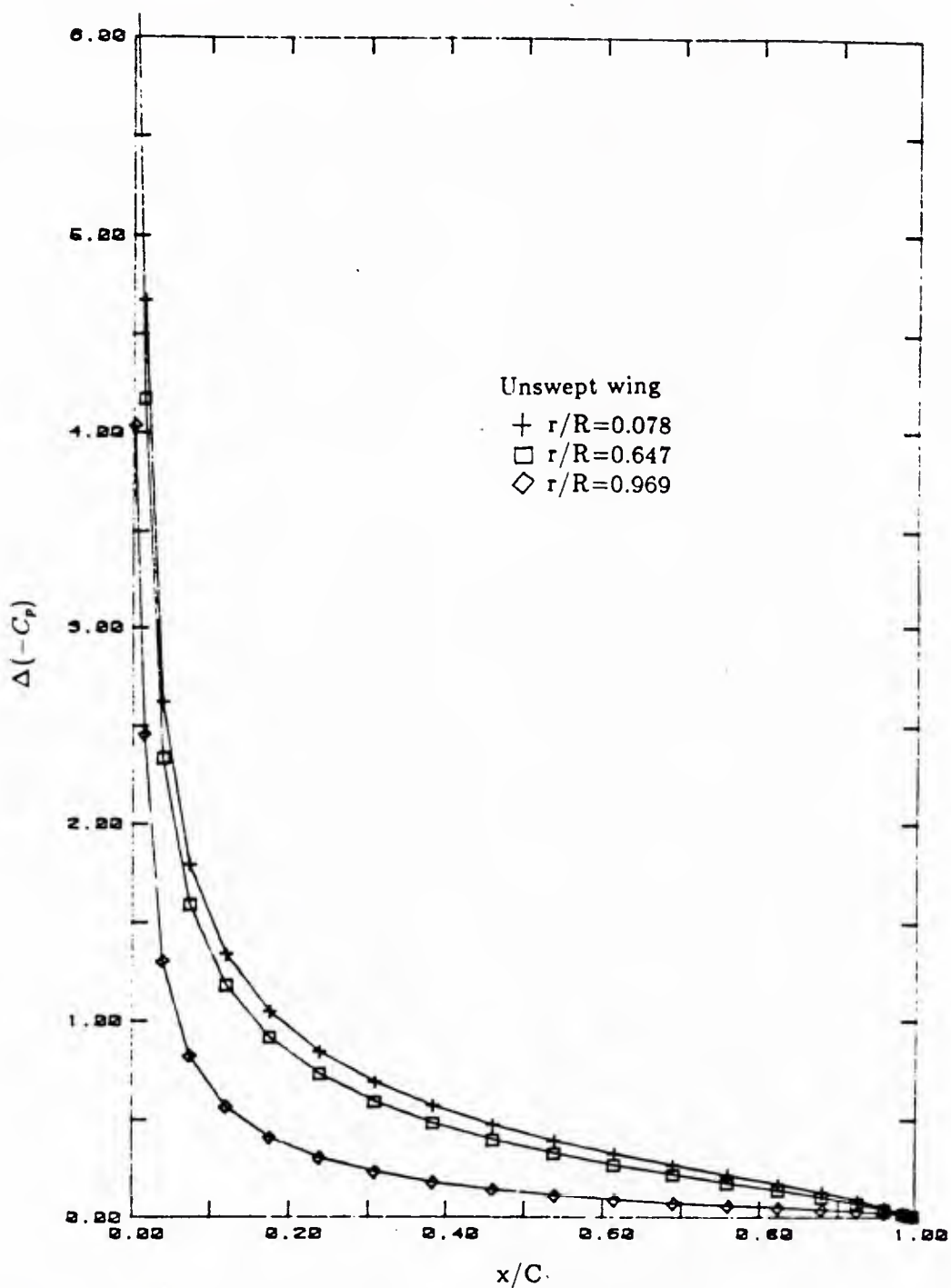


Figure 4.22: Chordwise distribution of the pressure difference of the unswept rectangular wing. (Aspect ratio=5.9, $t/c=0.05$, $\alpha=8$ deg.)

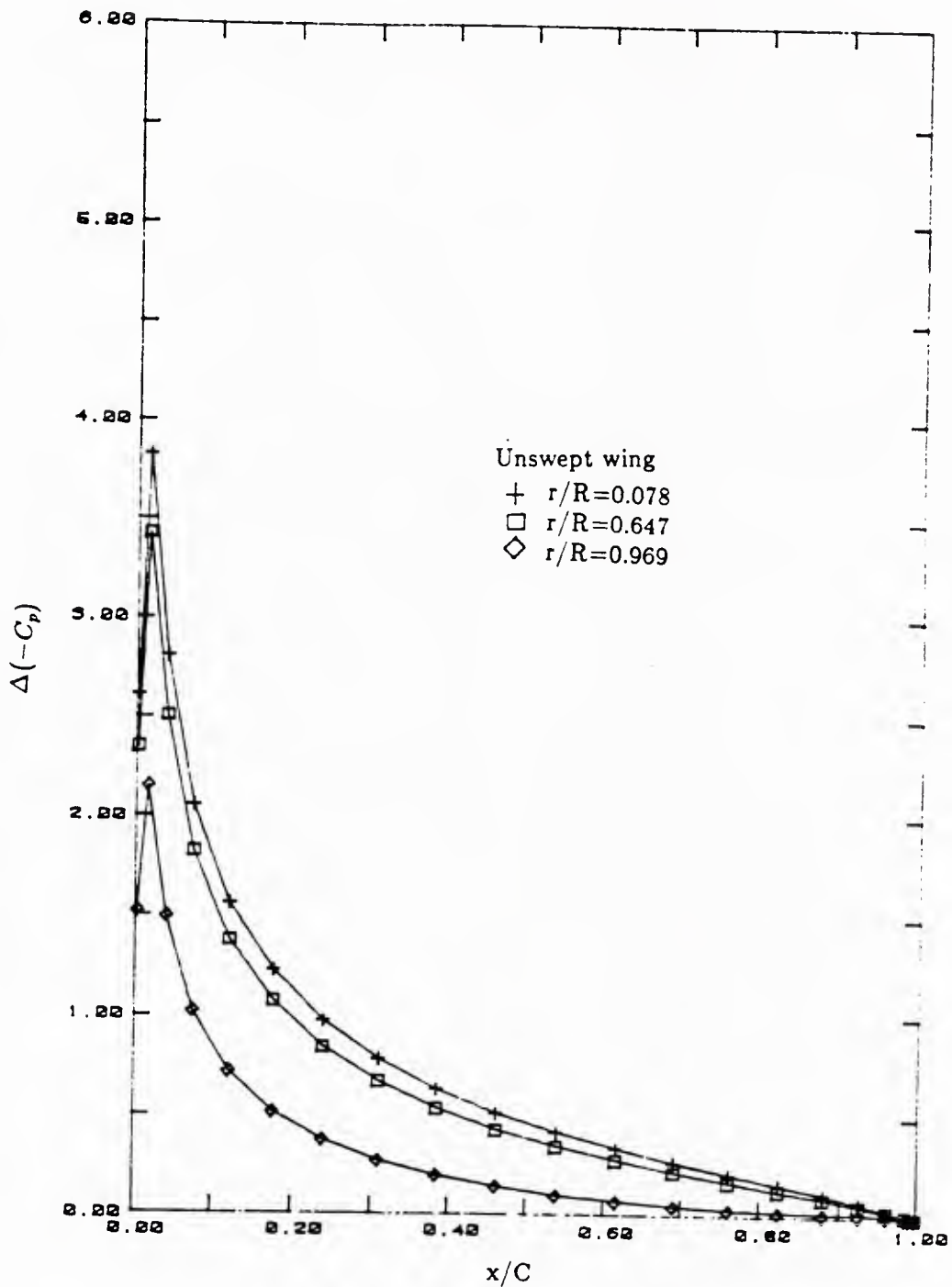


Figure 4.23: Chordwise distribution of the pressure difference of the unswept rectangular wing. (Aspect ratio=5.9, $t/c=0.12$, $\alpha=8$ deg.)

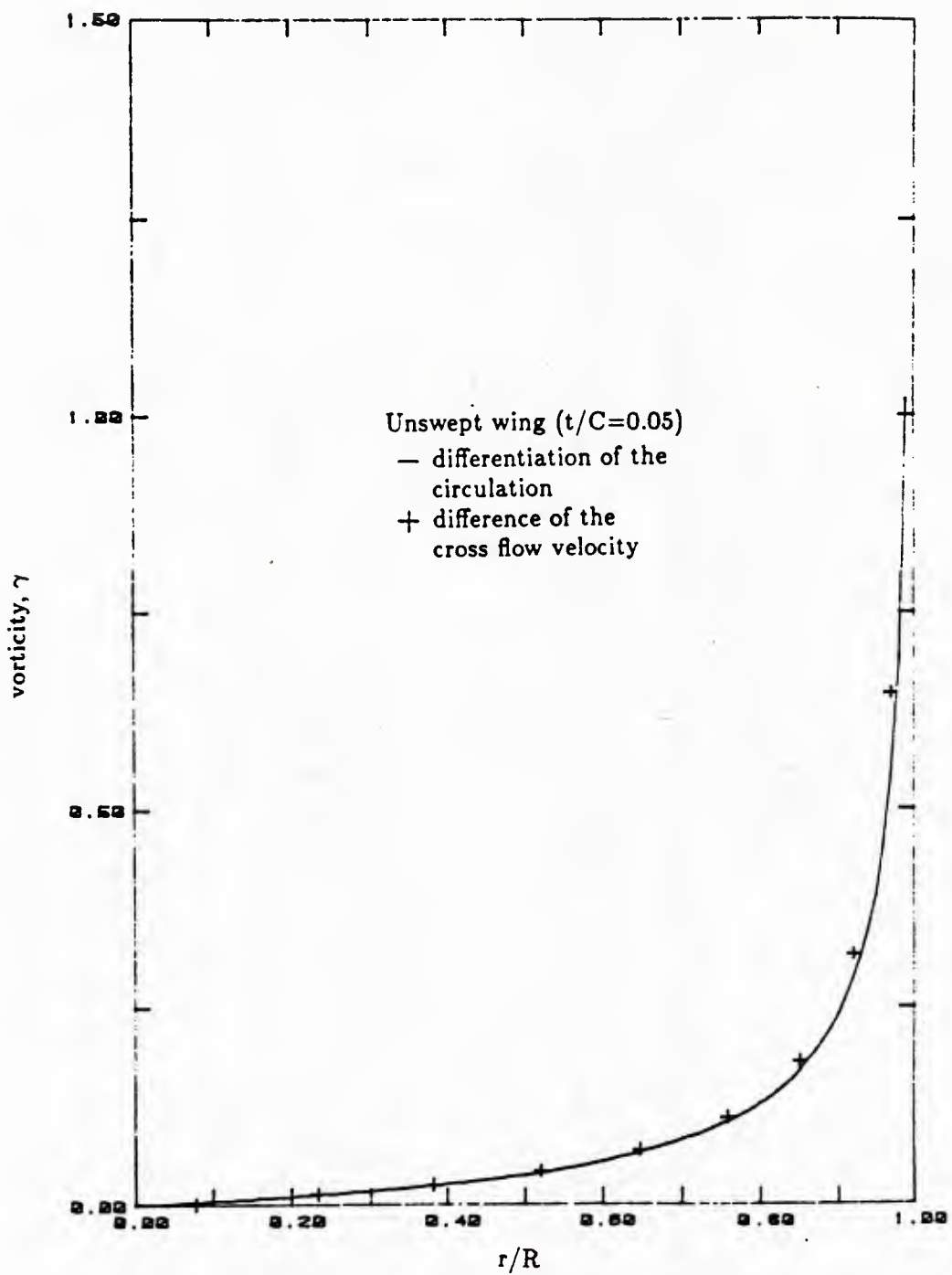


Figure 4.24: Spanwise vorticity distribution of the unswept rectangular wing. (Aspect ratio=5.9, $t/c=0.05$, $\alpha=8$ deg.)

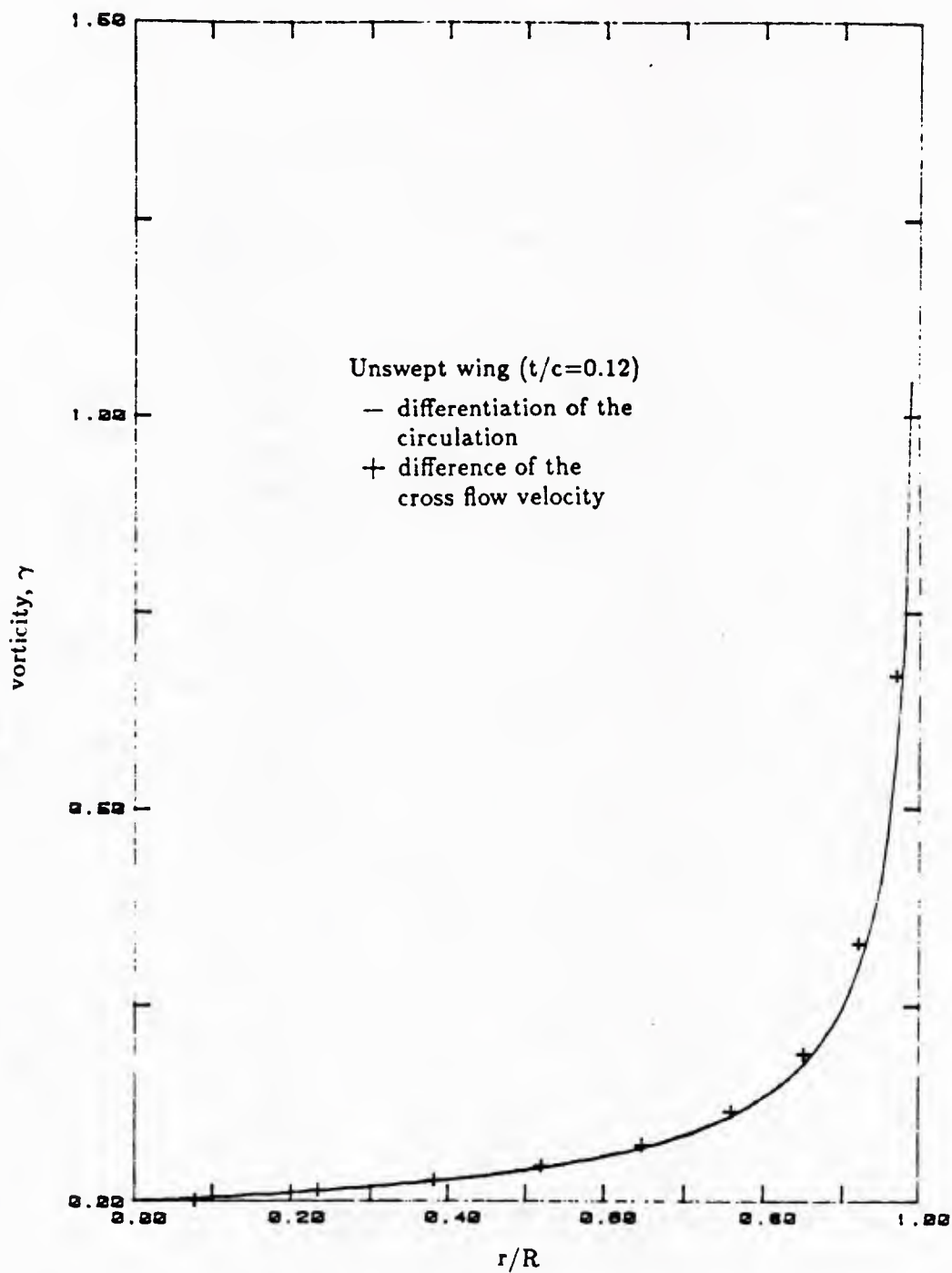


Figure 4.25: Spanwise vorticity distribution of the unswept rectangular wing. (Aspect ratio=5.9, $t/c=0.12$, $\alpha=8$ deg.)

overall circulation near the tip is reduced. The effect of thickness very close to the tip is shown to be the same as that of the circular wing, where the loading is decreased as the thickness is increased. This effect was explained in the section for the circular wing. However, for the inner part of the wing where the cross flow component is small, the circulation is increased as the thickness is increased.

Figure 4.27 shows the radial circulation distributions of the +45 degree swept wing with the varying thickness/chord ratios of 0.01, 0.05 and 0.12. Here, the downwash is bigger near the inner part of the wing due to the positive sweep, and as a result the loading is reduced. The thickness effect is shown to have a similar trend to that of the unswept wing.

Figure 4.28 provides a comparison of the local section lift coefficients by the present method with those by other production panel codes, for the unswept rectangular wing with aspect ratio 5.9 and NACA 0012 sections at 8 degree incidence. The results by the production panel codes are taken from Margason et. al. [17]. All of the panel methods, including the present one, over-predict the experimental data. This is attributable to neglecting the viscous effect. The result by the present method agrees well with those by the production codes.

The result for the +20 degree swept wing with aspect ratio 5.9 and NACA 0012 sections at 8 degree incidence is compared with those by the production codes in Figure 4.29. Again, the result by the present method agrees well with those by the other methods.

4.4 Wing-body configuration

A wing-body configuration is examined to determine whether the present method can determine the interference effect of a wing on a fuselage pressure distribution. Figure 4.30 illustrates the wing-body geometry selected for this example. An experimental surface pressure distribution, which was made in the RAE 8 ft \times 6 ft wind

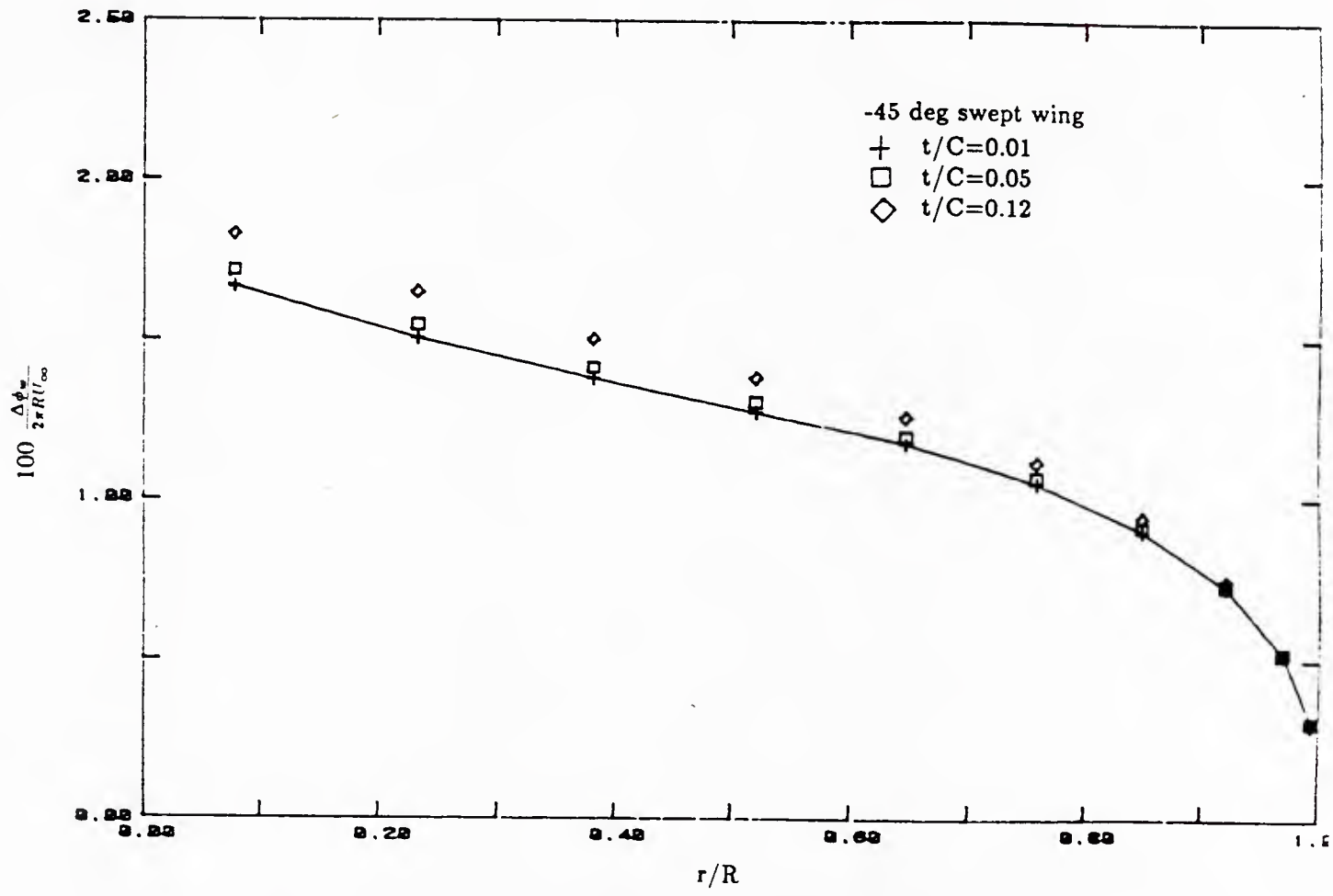


Figure 4.26: Radial circulation distribution for the -45 degree swept wing. (Aspect ratio=5.9, $\alpha=8$ deg.)

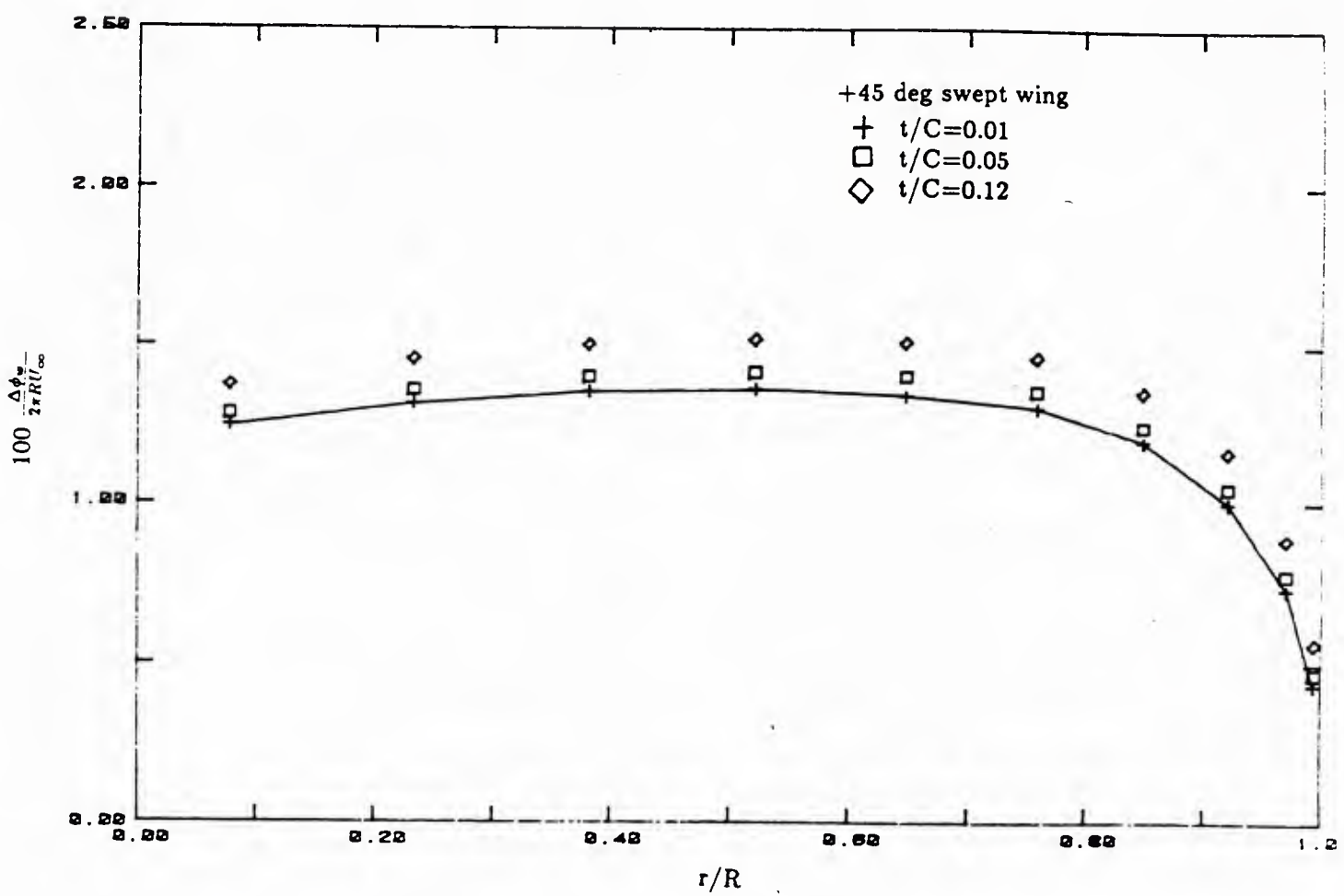


Figure 4.27: Radial circulation distribution for the +45 degree swept wing. (Aspect ratio=5.9, $\alpha=8$ deg.)

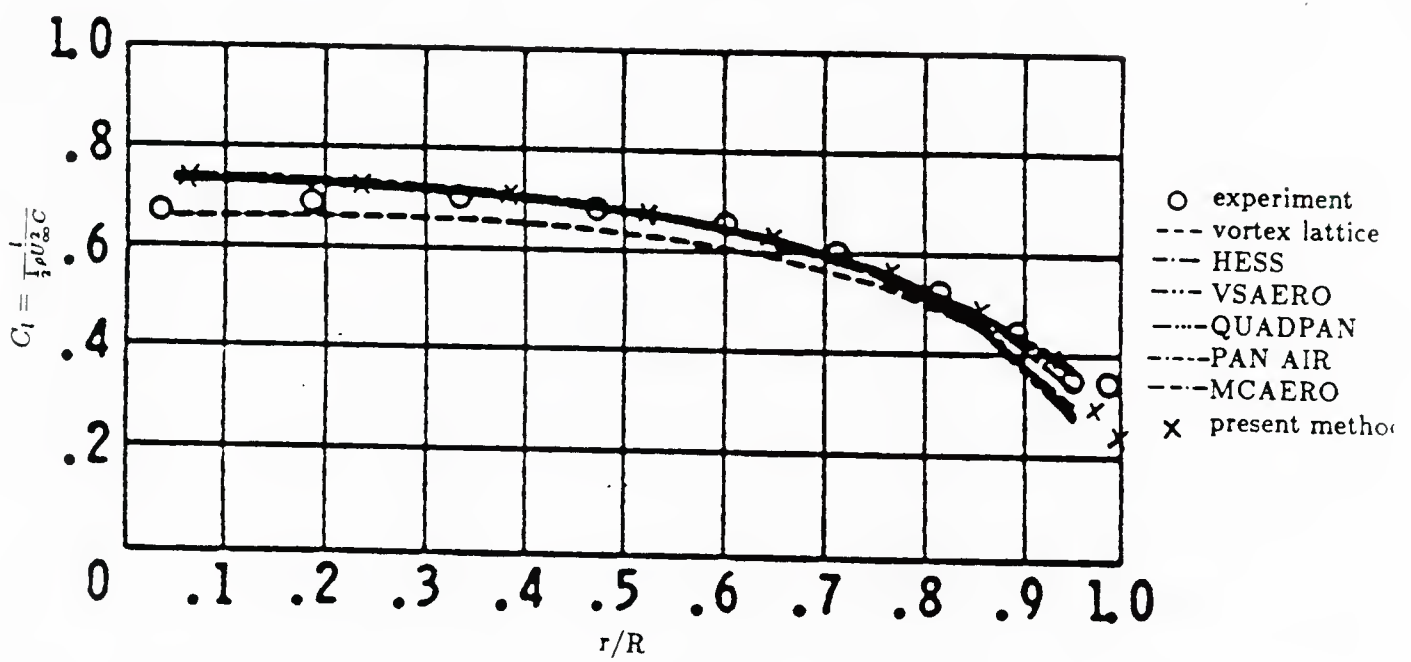


Figure 4.28: Spanwise local lift coefficient distribution for the unswept rectangular wing. (Aspect ratio=5.9, $t/c=0.12$, $\alpha=8$ deg.)

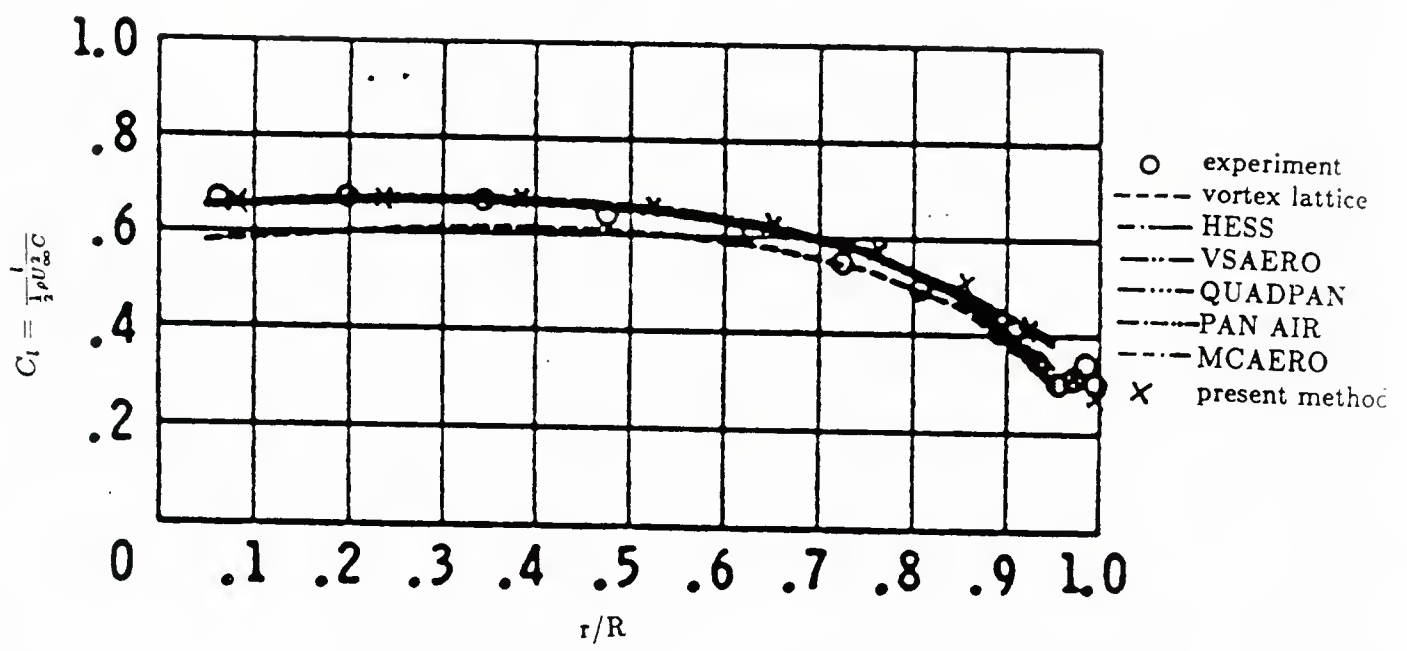


Figure 4.29: Spanwise local lift coefficient distribution for the +20 degree swept rectangular wing. (Aspect ratio=5.9, $t/c=0.12$, $\alpha=8$ deg.)

tunnel, was taken from Treadgold et. al. [22].

The geometry is symmetric with respect to both the wing chord plane and the zero butt line plane. The cross section of the wing is an uncambered RAE 101 section with thickness/chord ratio of 0.09. The planform has an aspect ratio of 6 and a mid-chord sweep of 30 degrees. The axisymmetric body has a nose profile given as a quartic function of the axial distance from the leading edge of the body, which is connected to the circular cylinder with a diameter/wing span ratio of 0.167.

The Reynolds number in the experiment, based on the geometric mean chord of the wing, was 1.0×10^6 . A fixed transition mechanism to stimulate turbulence transition was attached at 12.5 percent of the chord. The experimental data corresponds to a free stream Mach number of 0.4.

Panelling is established on only one side of the lateral plane of symmetry. The wing is modelled by 11 spanwise strips, which are located conveniently to match the spanwise locations of the control points with those given in the experiment. Each strip contains 20 upper and 20 lower surface panels. Axial panelling of the body is uniformly spaced except between the leading and trailing edge of the wing, where panelling is matched to that of the wing. The fuselage cross section panelling is equally spaced, with each panel subtending an arc of 30 degrees. The panel arrangement of the half wing-body configuration is shown in Figure 4.31.

The flow around the wing-body is calculated at 0 and 2 degree angles of attack. Neither compressibility nor viscous corrections are made to the calculated pressures.

The calculated and experimental wing section pressure distributions at three different spanwise stations are presented in Figures 4.32 through 4.34. Effect of the fixed transition is shown in the pressure distributions of the experiment at 12.5 percent of the chord. The agreement is excellent in spite of the fact that neither viscous nor compressibility corrections are applied.

The calculated and experimental fuselage pressure distributions are presented in

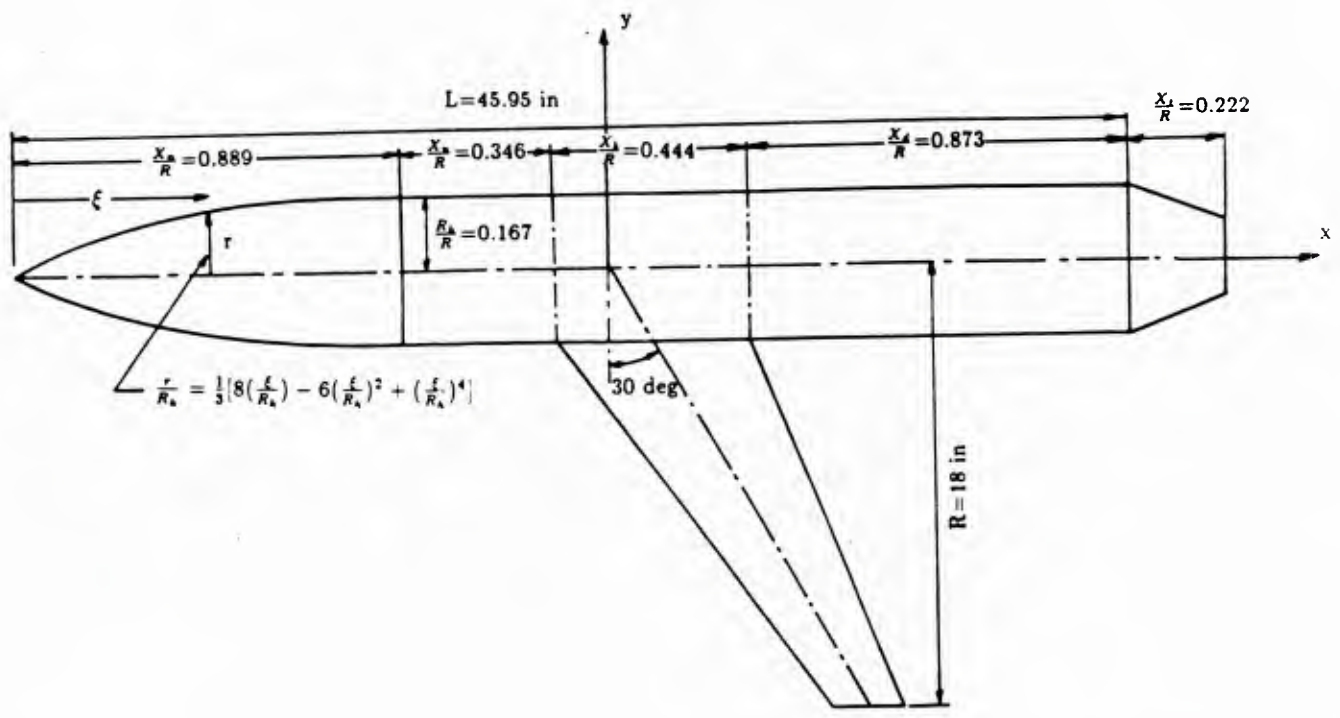


Figure 4.30: RAE wing-body configuration.

PANEL = 400
TIME = -60.0
INCSTEP = 100.0
XV = 000.0

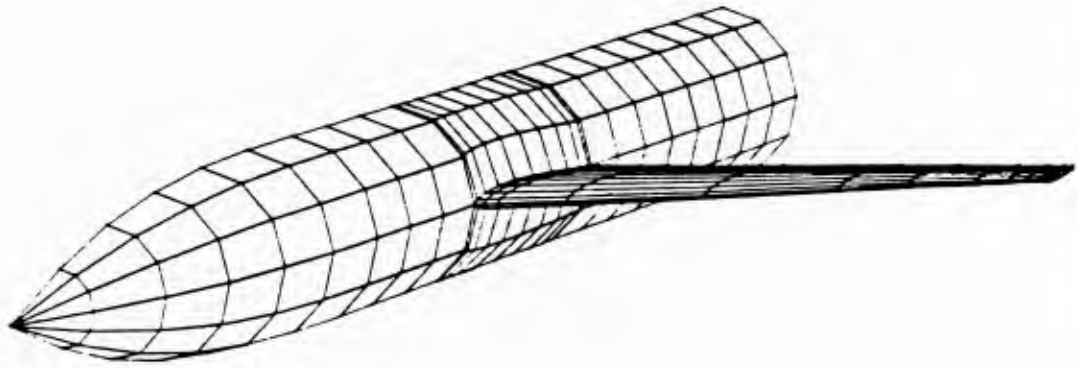


Figure 4.31: Panel arrangement of the half wing-body configuration.

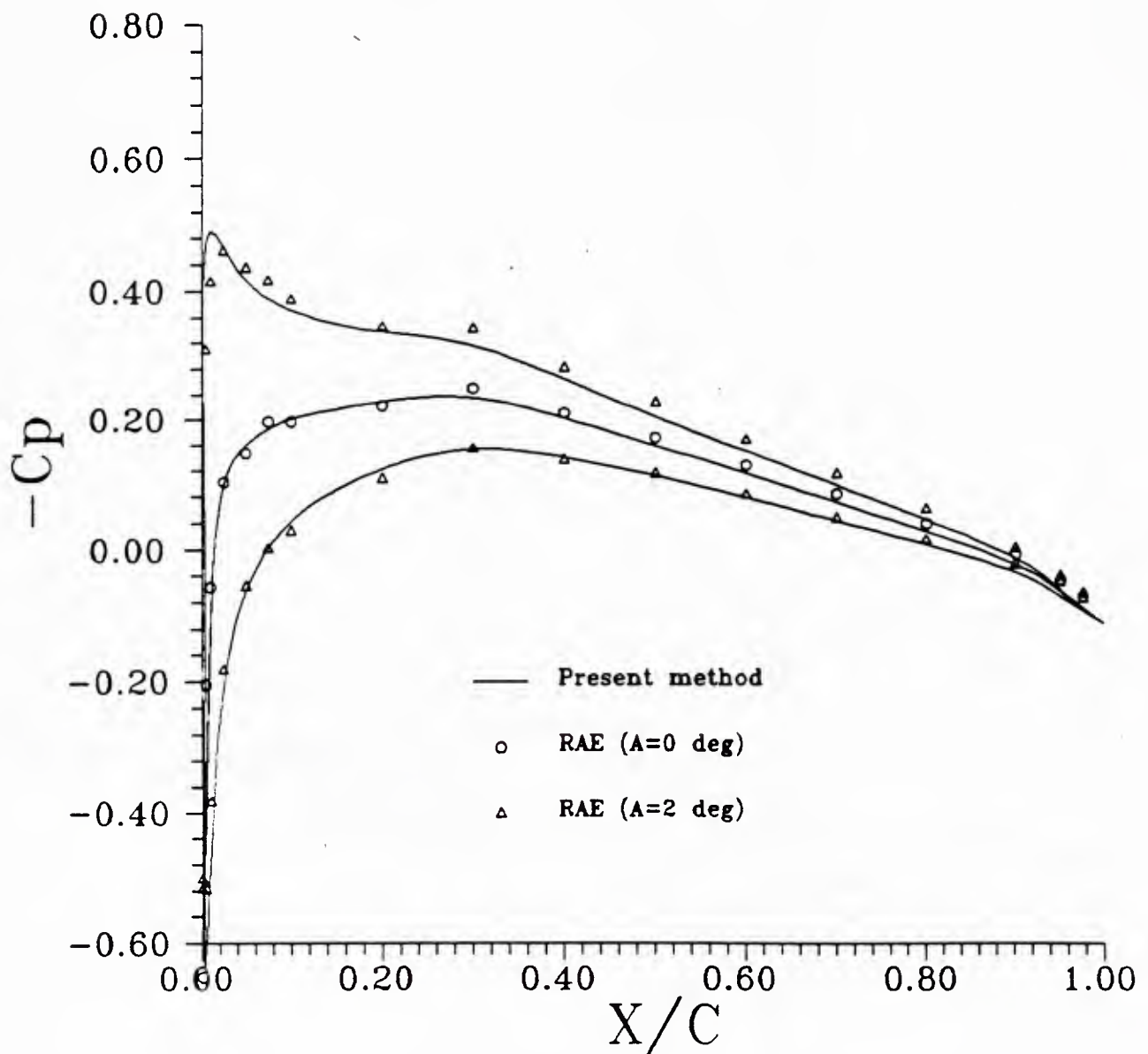


Figure 4.32: Wing-body chordwise pressure distribution at $r/R=0.25$.

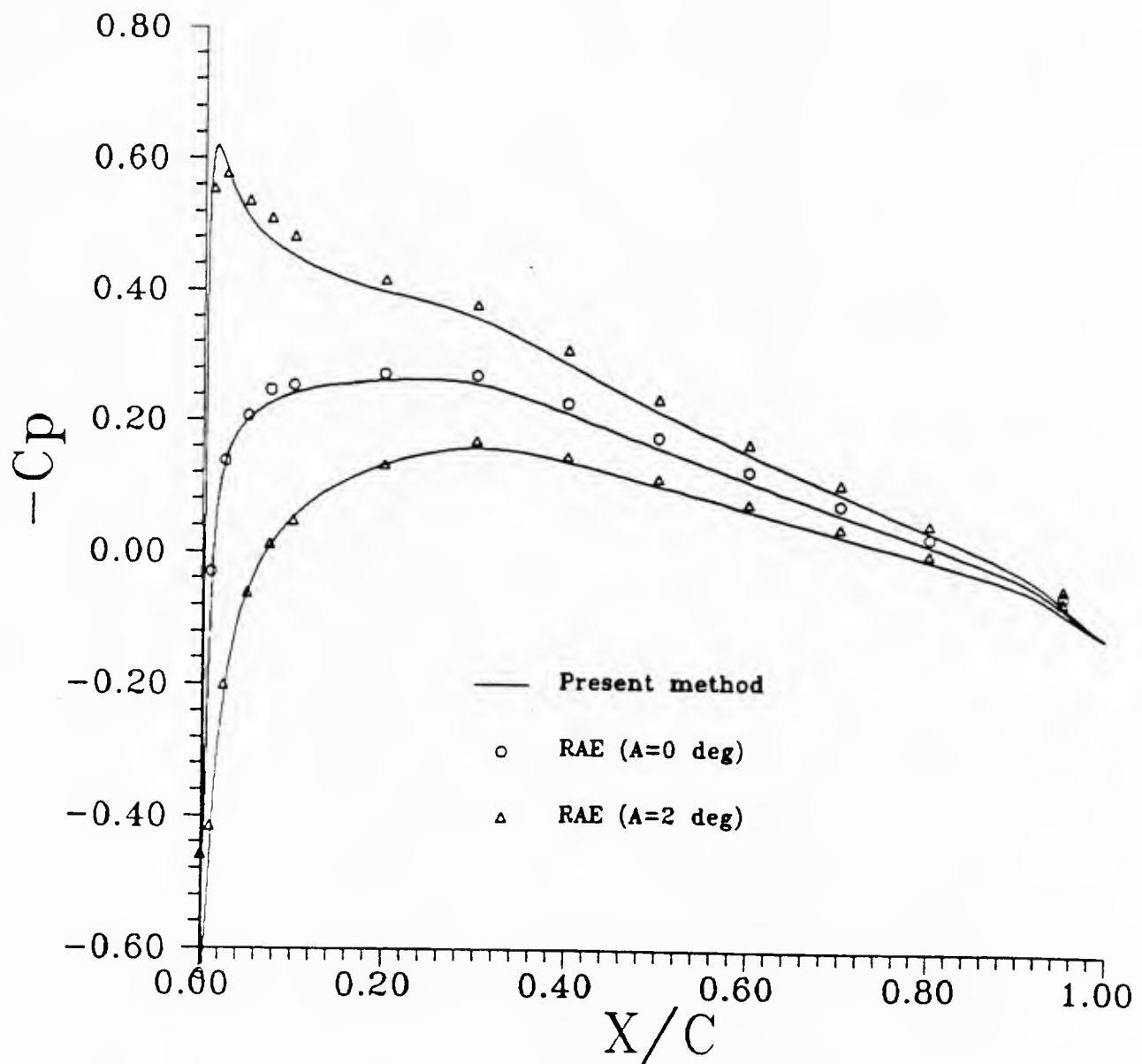


Figure 4.33: Wing-body chordwise pressure distribution at $r/R=0.60$.

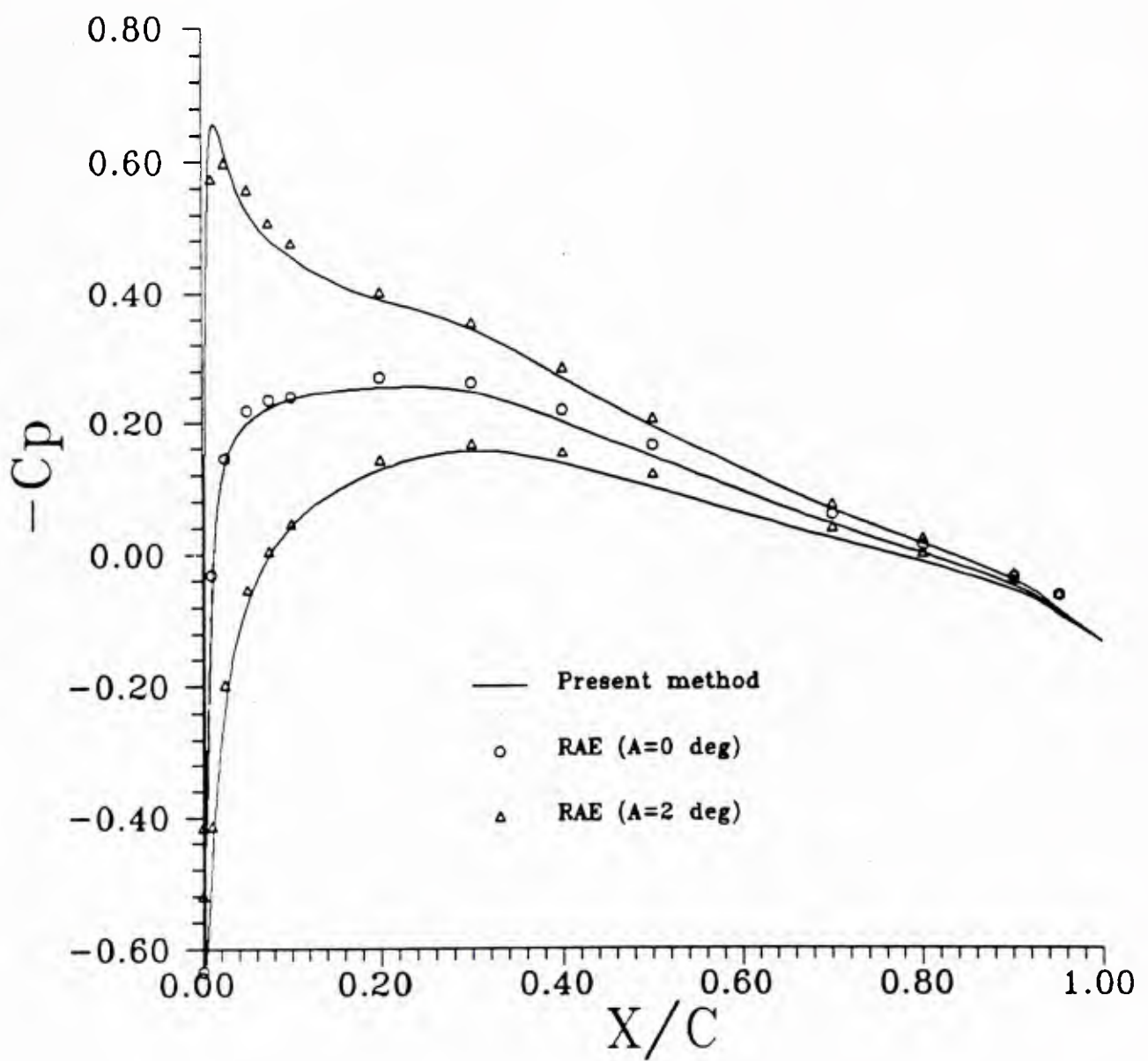


Figure 4.34: Wing-body chordwise pressure distribution at $r/R=0.925$.

Figures 4.35 through 4.37. The present method pressure distribution is of slightly lower magnitude immediately above and below the wing root. This is believed to be attributable to excursions from the normal azimuthal angles φ (see Figure 4.30). For the present method, the panelling at the wing-fuselage intersection is such that the actual values of φ are approximately ± 20 degrees instead of the nominal value of ± 15 degrees.

Since the panelling of the fuselage is matched to that of the wing, which is highly concentrated at the leading edge, axial lengths of the panels change rapidly. This produces the steep variation of the calculated pressure near the leading edge. Again, agreement between the calculated and experimental pressure distributions is shown to be satisfactory.

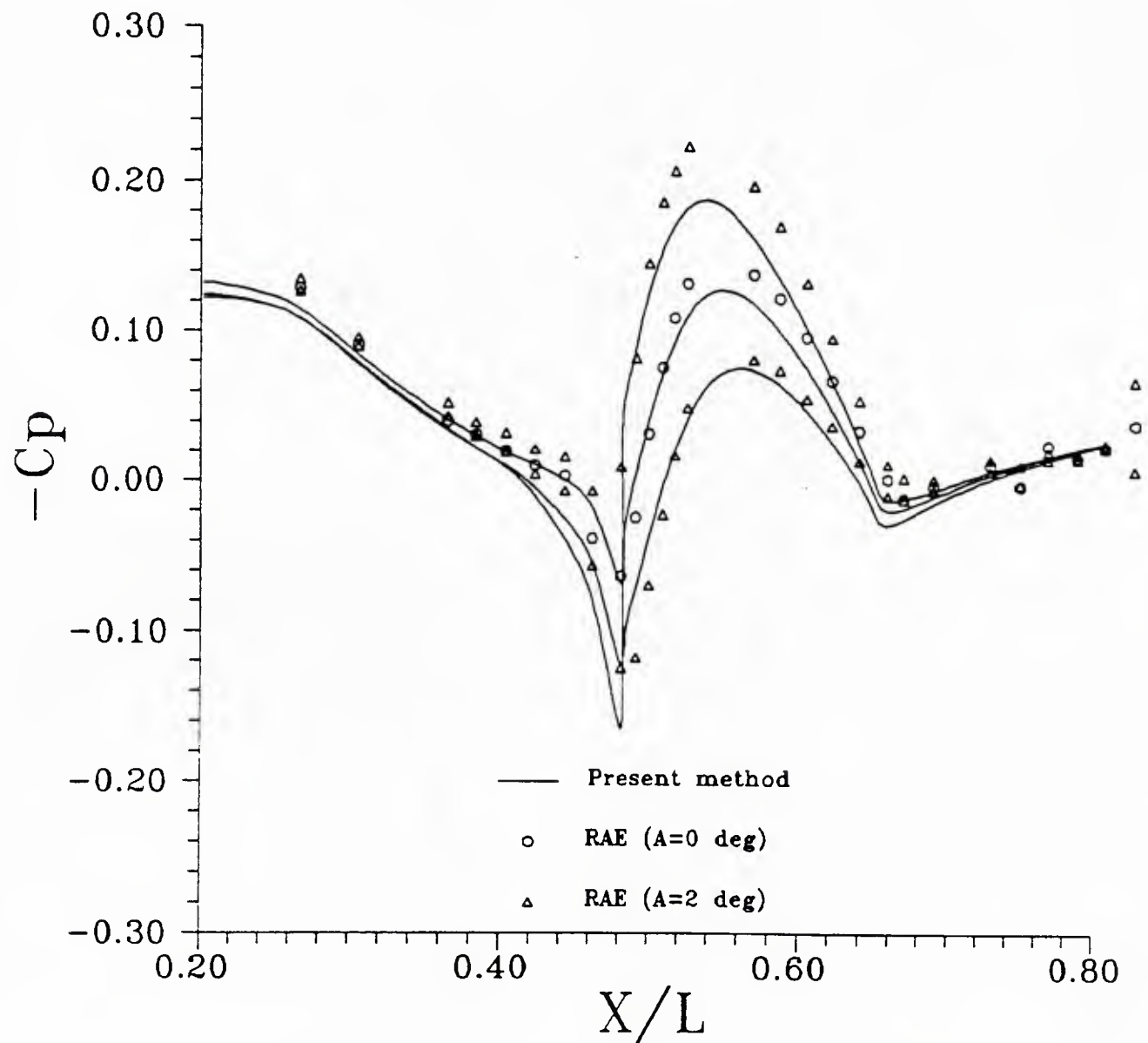


Figure 4.35: Fuselage pressure distribution in the presence of wing. ($\varphi = \pm 15$ deg.)

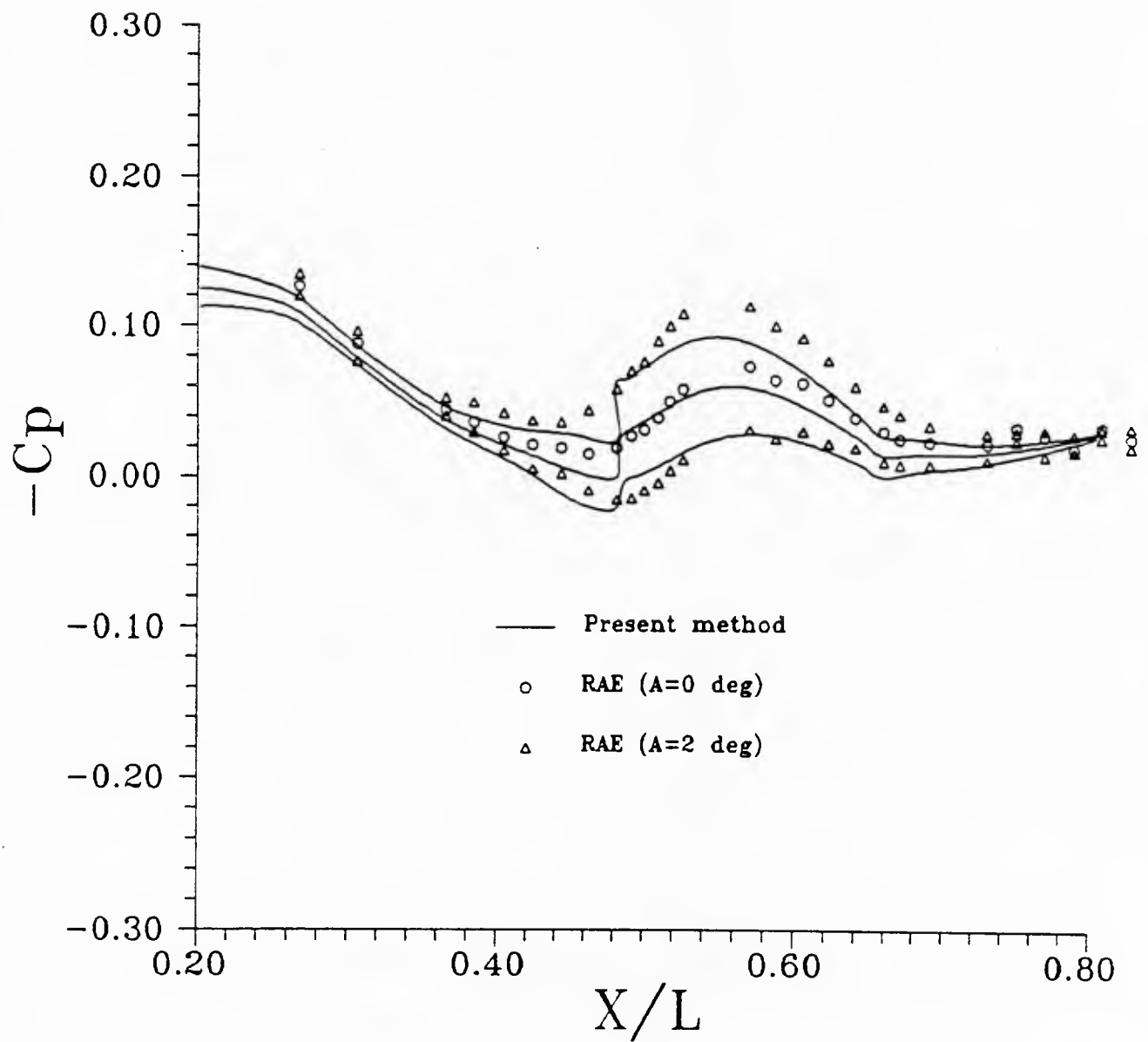


Figure 4.36: Fuselage pressure distribution in the presence of wing. ($\varphi = \pm 45$ deg.)

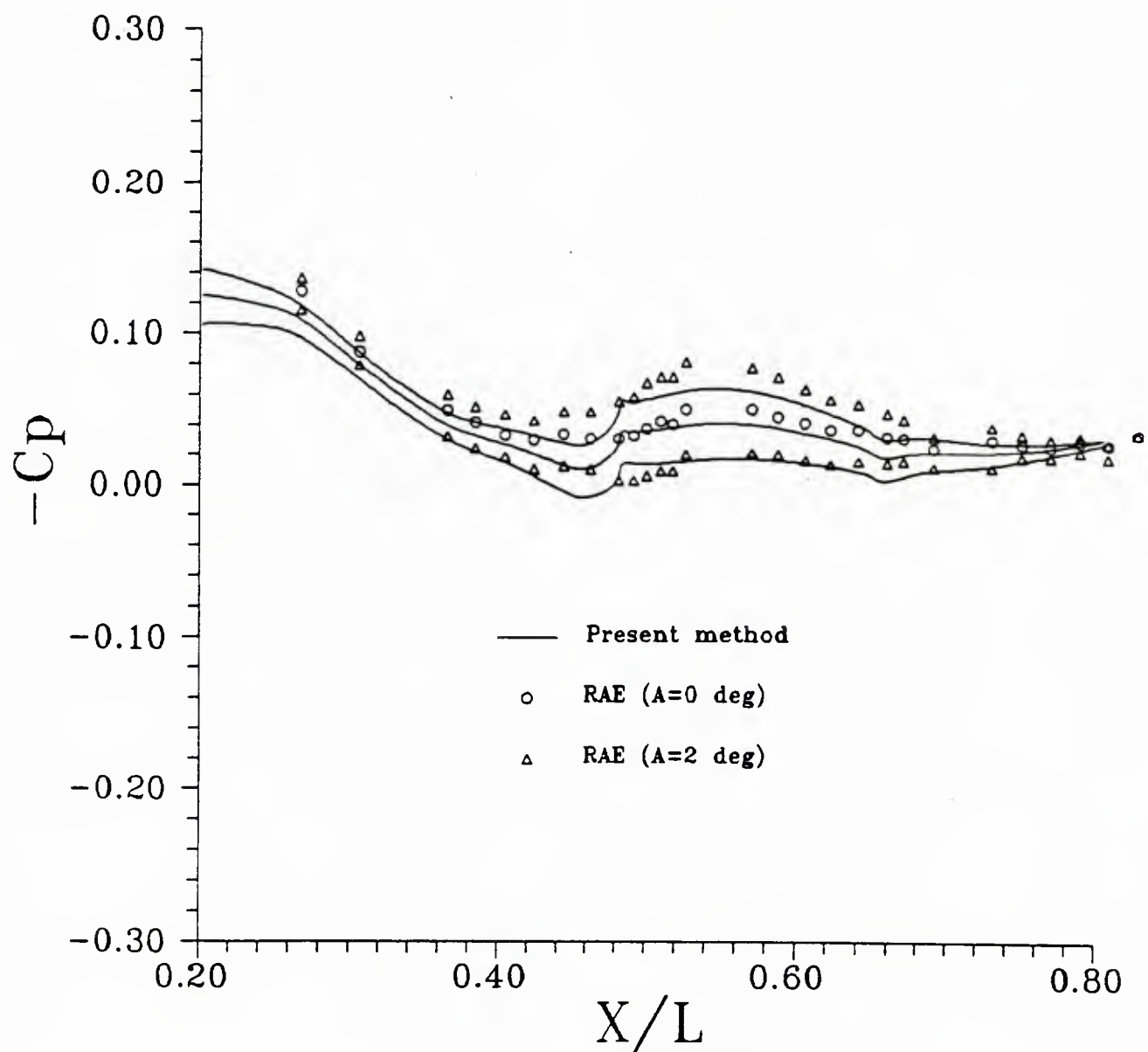


Figure 4.37: Fuselage pressure distribution in the presence of wing. ($\varphi = \pm 75$ deg.)

Part II

Duct problem

4.5 Axisymmetric duct

The next example is chosen to assess the capability of the present method to predict the internal flow properties. The geometry is a very long axisymmetric duct generated by wrapping a NACA 0010 section around a circular cylinder where the cylinder length/radius ratio is ten. The minimum internal cross sectional area is a factor of four smaller than the corresponding inlet and exit areas.

Results for this duct obtained with several panel codes were given by Bristow [2], and additional results were presented by Miranda [19] and by Hess [10] in a discussion to Miranda's paper. Predicting the pressure distribution for such an extreme duct is a very demanding test of a panel code. The mass flow through the duct, which is imposed by the Kutta condition, is extremely high in this case, and there is a tendency for all panel methods to underestimate its value.

Given an axisymmetric inflow, the solution is axisymmetric, so that the number of unknowns is equal to the number of chordwise panels. The geometry is specified only on the meridian section in the same way as a two-dimensional hydrofoil to exploit the symmetry, and the influence functions are formed by summing the individual panel contributions circumferentially. Panel arrangement for this geometry is illustrated in Figure 4.38.

For this axisymmetric case, the dipole strengths on the wake surface are constant in the circumferential direction. The induced potential at the control point p on the duct due to the wake surface S_w can be expressed as

$$(\Delta\phi)_{S_w} \iint_{S_w} \frac{\partial}{\partial r} \frac{-1}{R(p; q)} dS = (\Delta\phi)_{S_w} \iint_{S_0} \frac{\partial}{\partial x} \frac{-1}{R(p; q)} dS - (\Delta\phi)_{S_w} \iint_{S_\infty} \frac{\partial}{\partial x} \frac{-1}{R(p; q)} dS \quad (4.1)$$

where S_0 is a circular surface at the exit of the duct and S_∞ is a circular surface at downstream infinity. The contribution from the surface at infinity is negligible as the distance from the control point becomes infinite. As a result, the wake panels can be

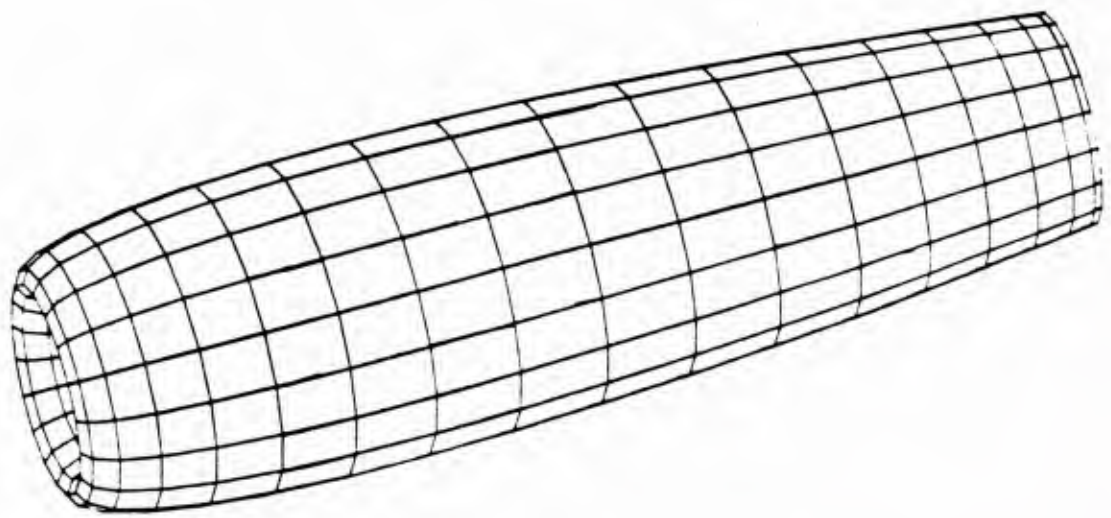


Figure 4.38: Panel arrangement for an axisymmetric duct formed from a NACA 0010 section with a chord/mean radius ratio of ten. ($N_c=36$, $M_\theta=18$)

replaced by a circular dipole disk at the exit of the duct.

The pressure distribution for various grids are shown in Figure 4.39. The first four calculations are for a fixed number of chordwise panels (N_c) equal to 36, but with the number of circumferential panels (M_θ) varying between 9 and 60. The results for 36 and 60 circumferential panels are almost identical, and indicate a minimum pressure coefficient of -11.3. Increasing the number of chordwise elements to 60 reduces the minimum pressure coefficient to -12.5.

Some results obtained with other panel codes are shown in Figure 4.40, which is taken from [19]. The *exact* solution, obtained with a special high order axisymmetric panel code [3] shows a minimum pressure coefficient of -13.8 which is slightly lower than the minimum value which obtained here. The results obtained by a high order panel code developed by Hess [7] and by QUADPAN [19], a low order potential based code, are similar to the present method. The results obtained by the Hess low order velocity based code [6] show pressure minima much closer to zero, which is evidently an inherent problem with that method for internal flows.

An extension of the present code to the non-axisymmetric problem, with a propeller inside the duct in a non-uniform flow, is reported in [13].

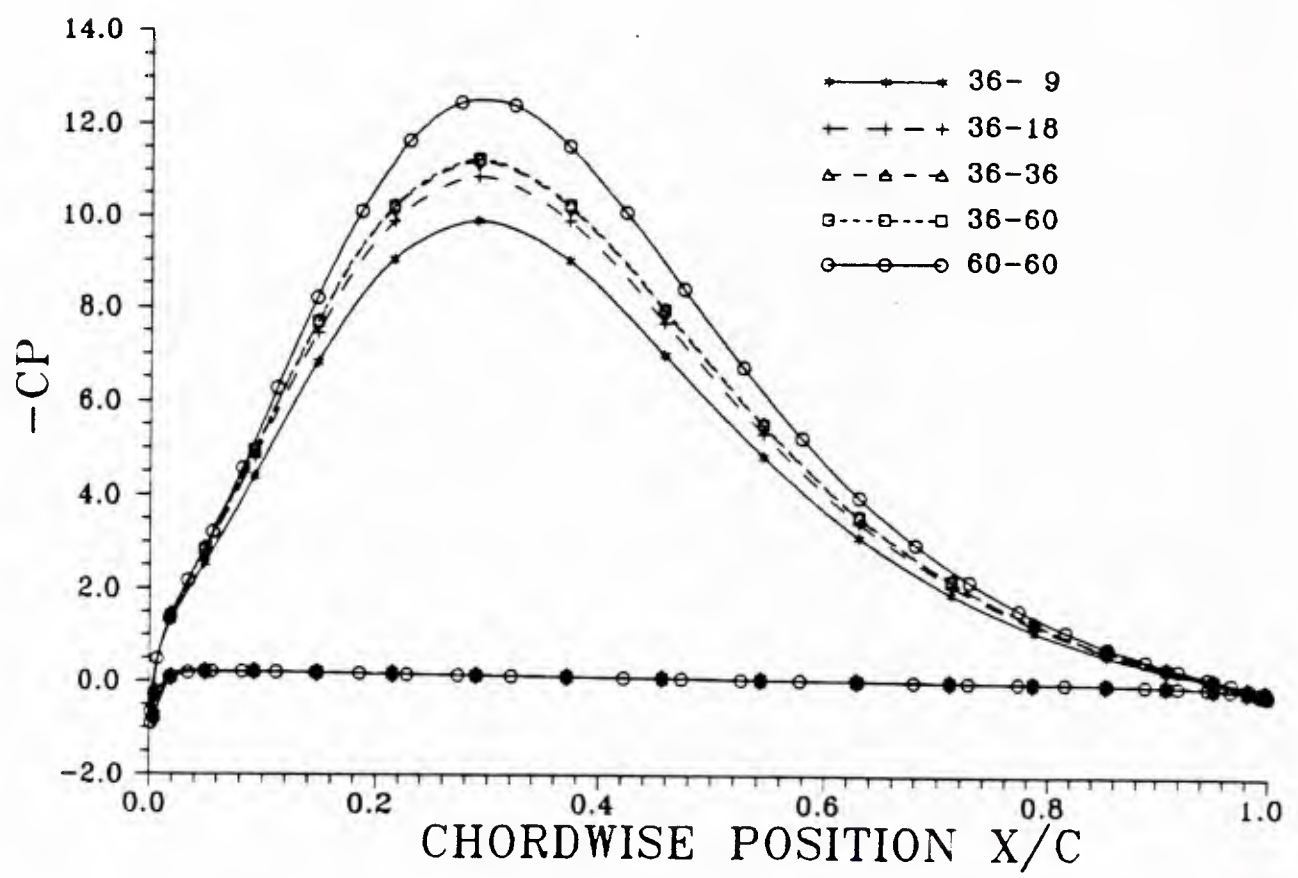


Figure 4.39: Pressure distribution for the axisymmetric duct with the present method with different number of panels.

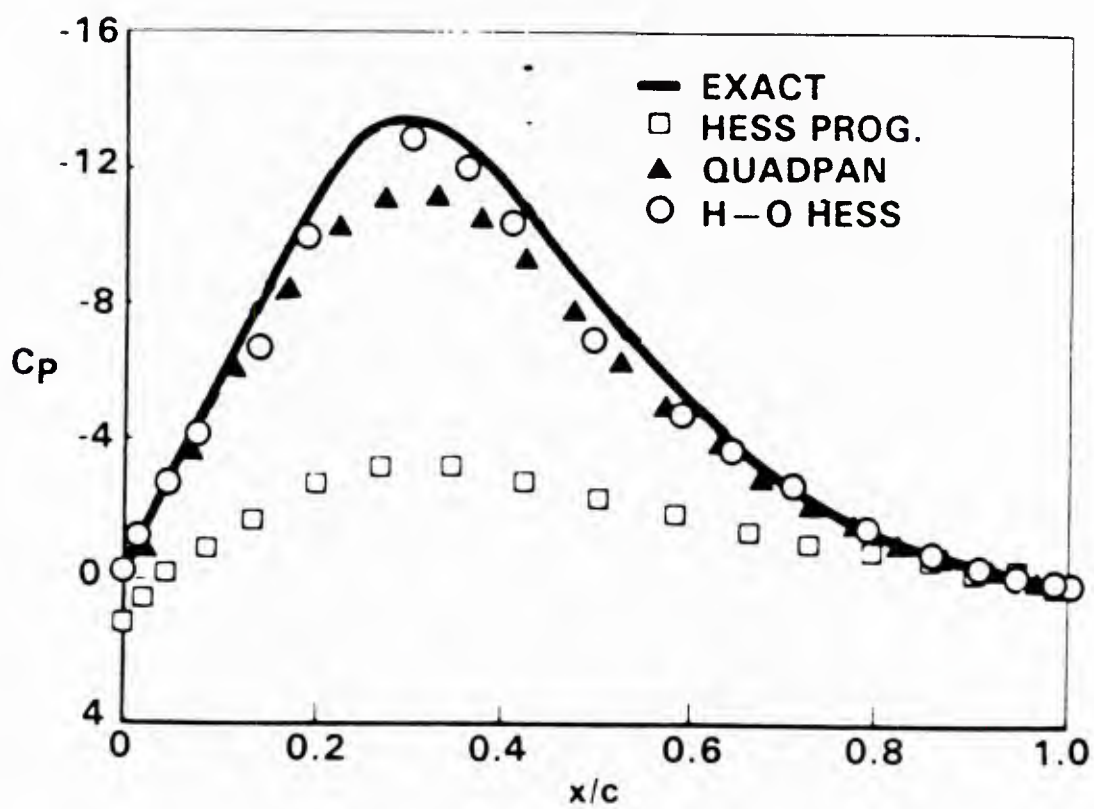


Figure 4.40: Pressure distribution for the axisymmetric duct by different panel method as presented by Miranda [19].

Part III

Propeller problem

4.6 Propeller performance analysis in steady flow

The final example is a marine propeller on an axisymmetric hub. The propeller is NSRDC 4118, which is a member of the NSRDC series propellers whose experimental results are available from [1]. The propeller is the unskewed propeller with three blades, and the section shape of the blade is an NACA 66 mod. thickness form superposed on an $a=0.8$ mean camber line. The geometry of the hub is a circular cylinder with a fairwater whose ordinates are given as a quartic function of the axial distance from the downstream end of the hub, as shown in Figure 3.4. Input geometric parameters in Figure 3.4 are given as $R_h=0.2$, $X_u=0.5$, $X_d=0.15$, and $X_t=0.5$.

Since the geometry and the loading is repeated identically on each blade and on each inter-blade segment of the hub, one third of the geometry is discretized. Ten chordwise strips of panels are arranged to be denser toward the tip, and each strip contains twenty upper and twenty lower surface panels.

Axial panelling of the hub is chosen to have eight panels upstream, twelve panels downstream, and twenty panels between the leading and trailing edges of the blades. Eight circumferential panels are equally spaced, with each panel subtending an arc of 15 degrees. As explained in Section 3.2, replacement of the upstream hub with the dipole disk at the upstream end of the hub significantly decreased the computational axial distance, X_u , without loss of accuracy. Panel arrangement of one third of the propeller is shown in Figure 4.41, and that of the whole propeller is shown in Figures 3.2 and 3.3.

Calculations are performed for three different flow conditions. The design advance coefficient for the propeller is $J=0.833$. For the computations described here the appropriate values of the ultimate wake radius(R_w), ultimate hub vortex radius(R_{wh}), and tip vortex contraction angle(δ_c) were determined from the experimental measurements of Min [18]. They are given as $R_w=0.83$, $R_{wh}=0.1$, and $\delta_c=15$ degrees. Distance from the propeller plane to the beginning of the ultimate wake region(X_{tw}) is given

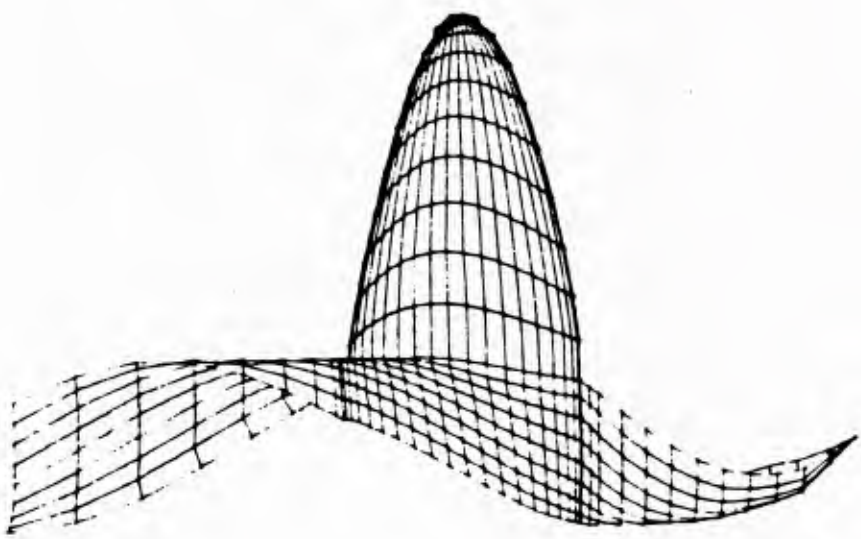


Figure 4.41: Panel arrangement of one third of the propeller.

as 1.5.

The pitch distribution of the transition wake is given as an input from the results by a lifting surface code [5], where the wake is aligned to the resultant flow. Since the ultimate wake, which extends to infinity downstream, is replaced by the sink disk at the beginning of the ultimate wake region, only 8 panels between the helical dipole strips are required to represent the whole ultimate wake. The panel arrangement for the wake, including the panels for the sink disk, is illustrated in Figure 4.42

The viscous drag coefficient is taken to be 0.003 for the calculation for the design condition, and that for the off-design condition is taken from the two-dimensional section drag coefficient curve.

The measured and computed open-water characteristics after the viscous correction are shown in figure 4.43. Agreement is shown to be satisfactory.

The perturbation potential distributions on the blade surface at three different radii at design J are given in Figure 4.44. The abscissa is taken as a nondimensional arc-length along the chordwise strip, which is zero at the lower trailing edge and one at the upper trailing edge of the blade.

Blade pressure distributions at design J are illustrated in Figure 4.45 at three different radii. The pressure distributions are shown to be smooth even very close to the tip. The positive loading at the trailing edge near the tip, which was experienced with the other low order panel method [15], is removed by adopting the pressure Kutta condition. The pressure difference between the upper and lower surface, which is the loading on the blade, is shown to have an $a=0.8$ loading shape at this design J. Unfortunately, there are no experimental pressure data to compare with these computations.

The perturbation potential distributions on the hub surface along three different streamwise panels are given in Figure 4.46. The potential values at the far upstream panels are shown to be the same in the circumferential direction, which is the justification for the assumption of a uniform potential in the axial direction.

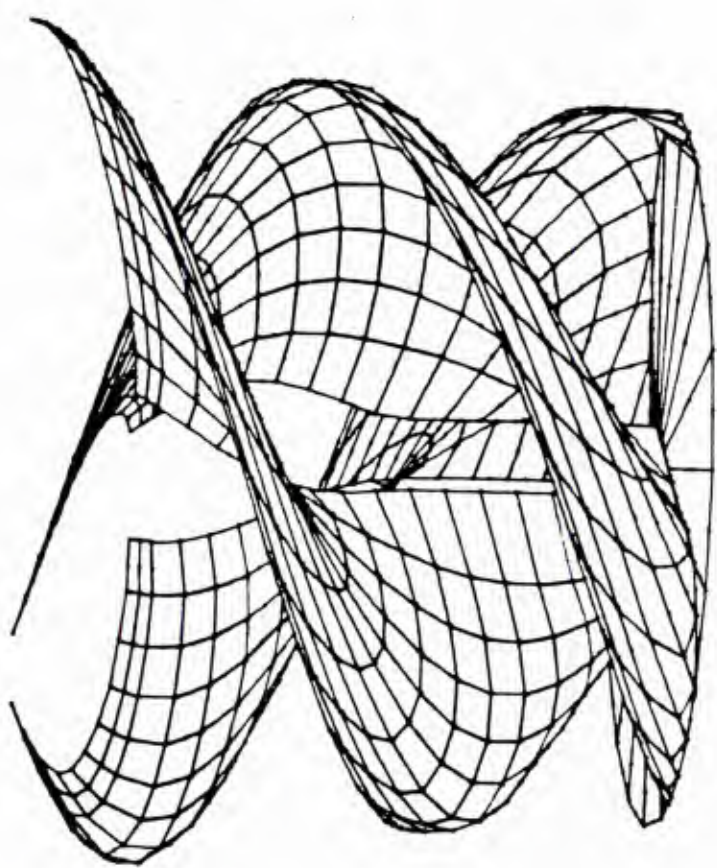


Figure 4.42: Panel arrangement for the wake.

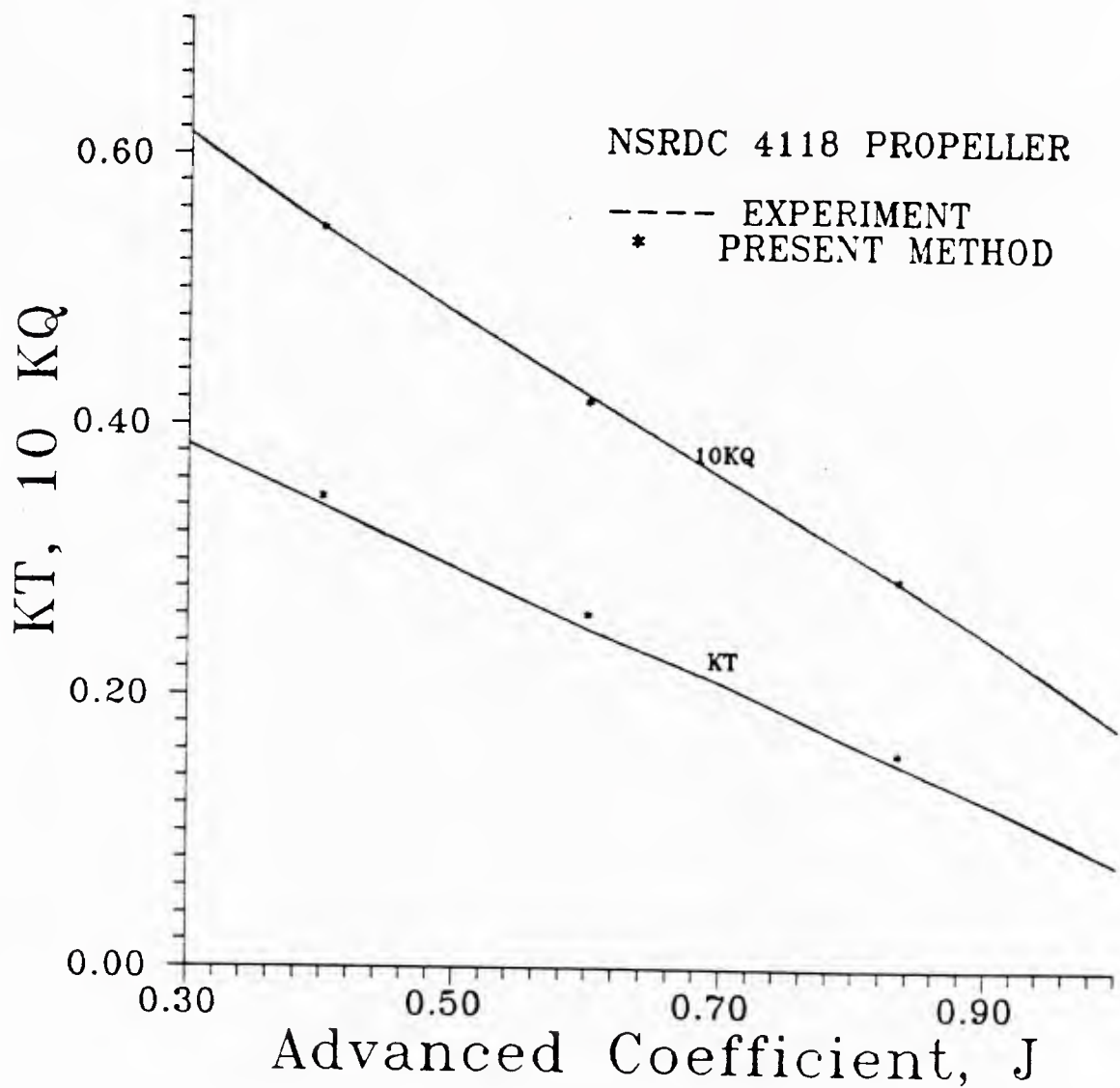


Figure 4.43: Measured and calculated open water characteristics of NSRDC propeller 4118.

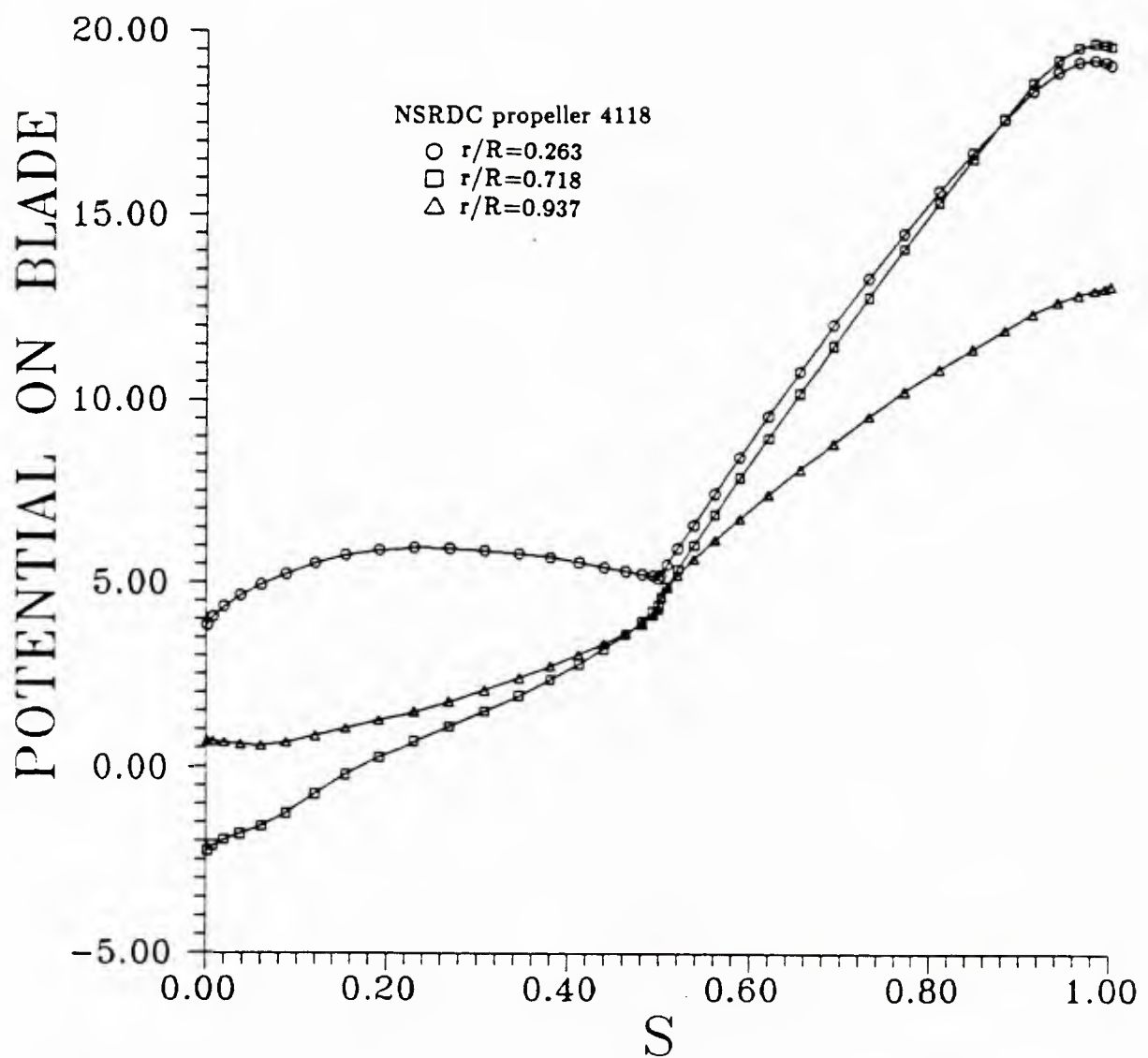


Figure 4.44: Perturbation potential distribution on the blade for NSRDC propeller 4118 operating at an advance coefficient $J=0.833$.

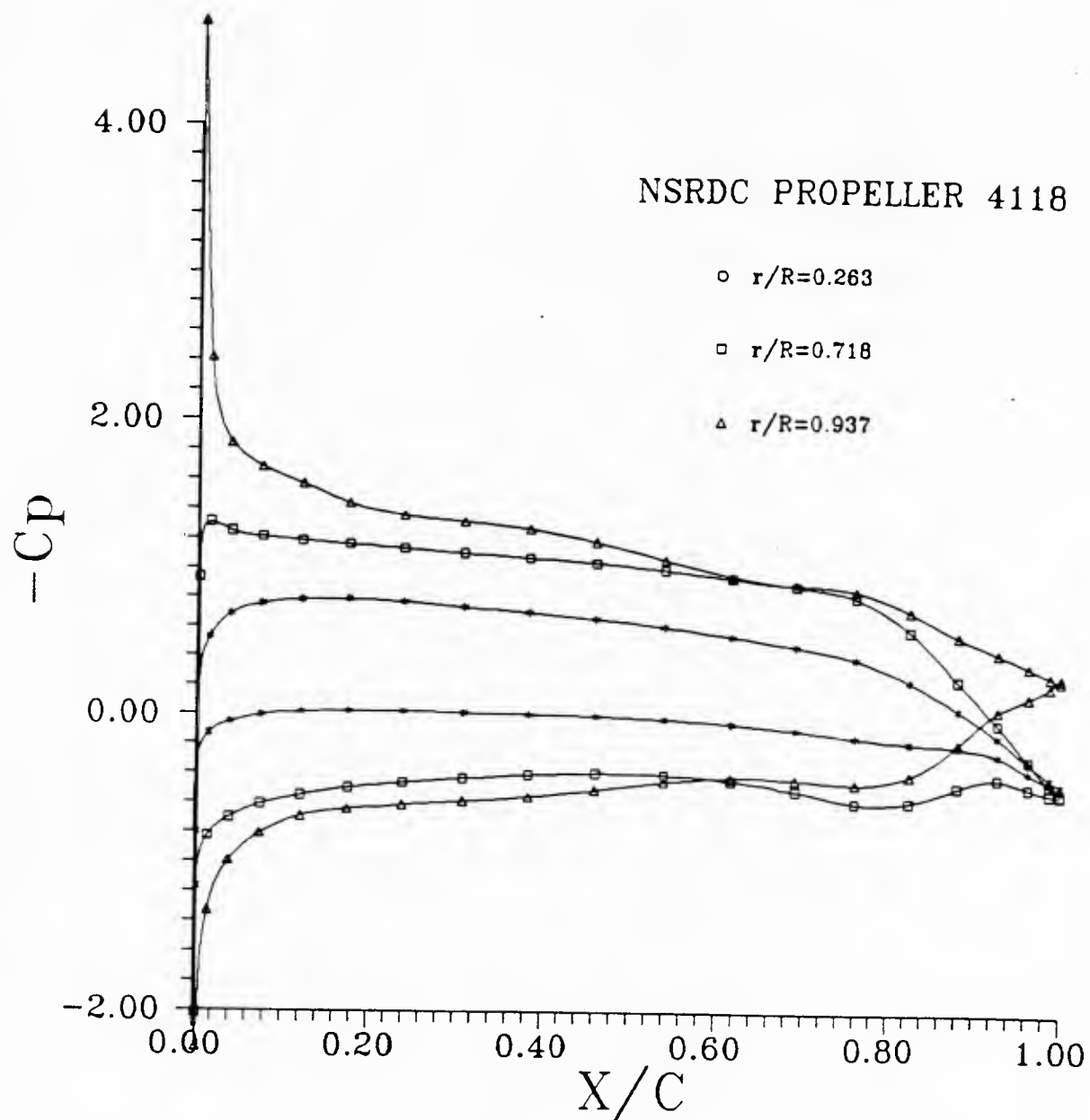


Figure 4.45: Computed chordwise pressure distributions for NSRDC propeller 4118 operating at an advance coefficient $J=0.833$.

cation of replacing the semi-infinite upstream hub by the dipole disk. The potential jump at the trailing edge of the root section is preserved in the hub panels along the wake surface.

Computed hub pressure distributions are shown in Figure 4.47 along three different streamwise strips. Due to the rapid change of the panel size near the leading edge, the pressure distribution at the leading edge is not smooth.

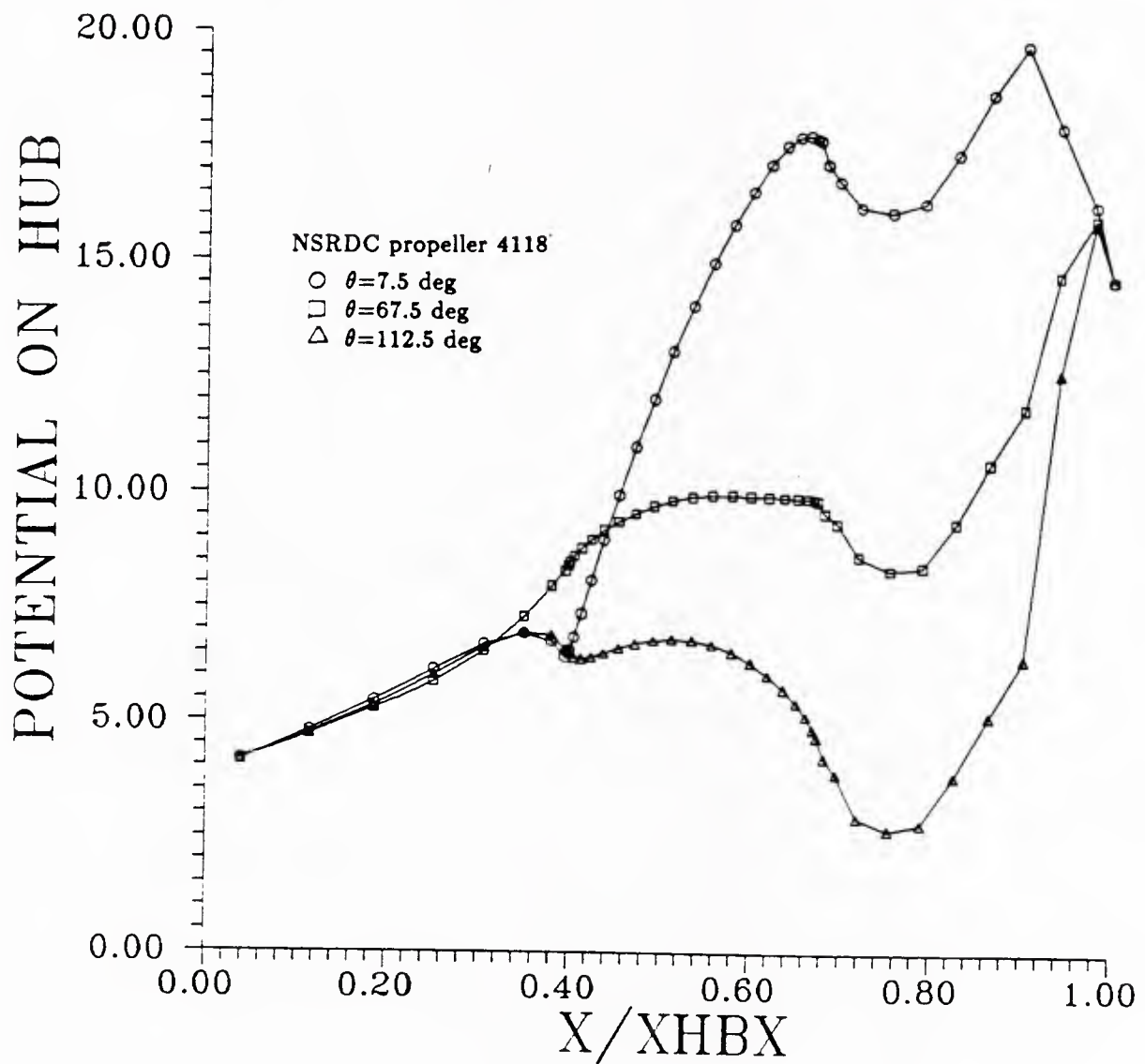


Figure 4.46: Perturbation potential distribution on the hub for NSRDC propeller 4118 operating at an advance coefficient $J=0.833$.

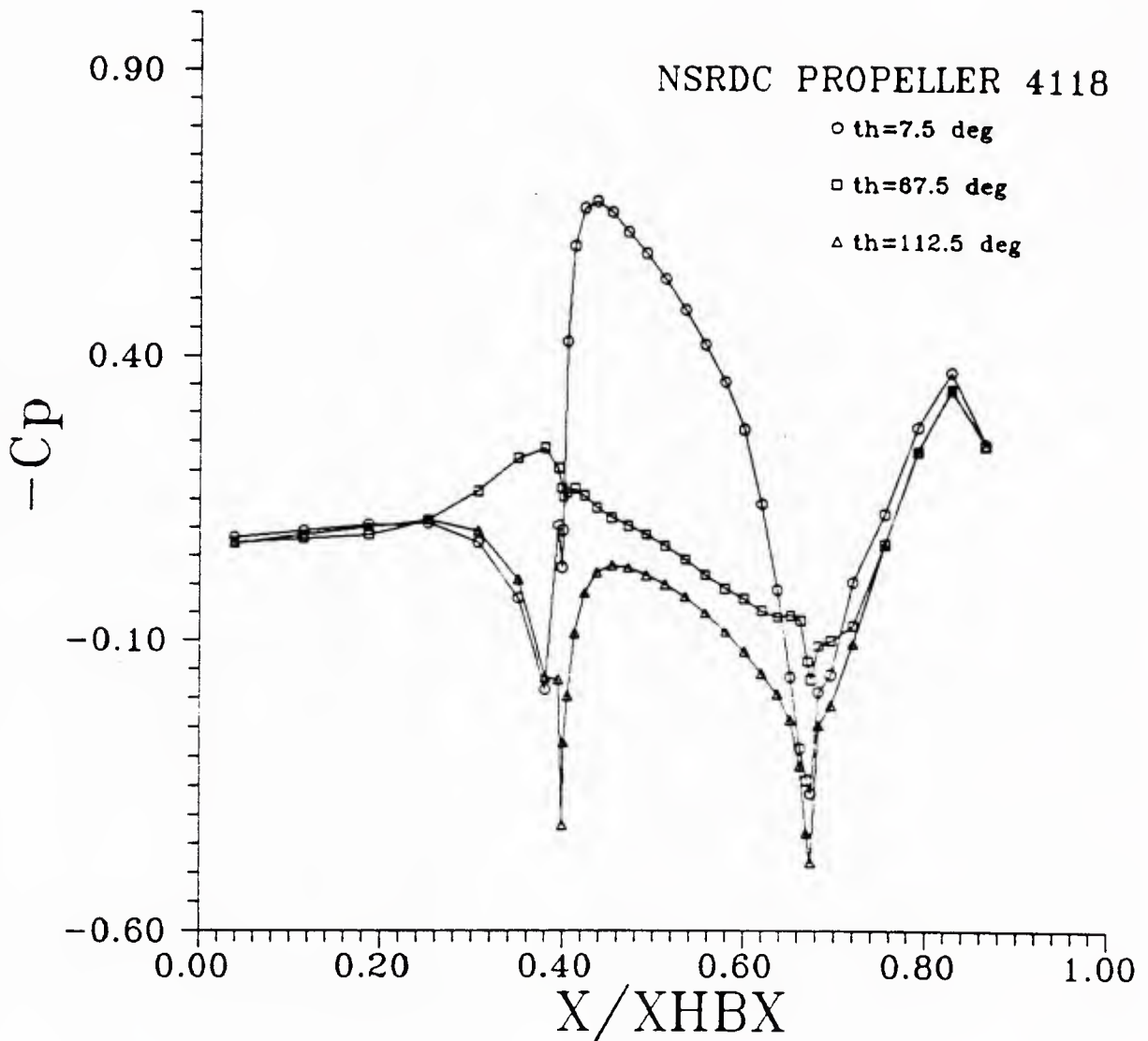


Figure 4.47: Computed hub pressure distributions for NSRDC propeller 4118 operating at an advance coefficient $J=0.833$.

Chapter 5

Conclusions

A surface panel method suitable for the analysis of marine propellers is developed and applied to various geometries to demonstrate its effectiveness. In the way of selecting the most suitable method for the marine propellers, basic theories behind the various panel methods are reviewed and characteristics of each method are compared. The perturbation potential method is selected because of its robustness to the extreme geometries, such as a very thin foil section and a long duct. The perturbation potential method also requires relatively smaller computing times and computer storage compared to the velocity method.

The usual Morino's Kutta condition is found to have a deficiency for thick foil sections with finite trailing edge angles. Moreover, it does not account for the three-dimensional cross flow effects, which become large toward the blade tip. The deficiency for thick foil sections is removed by including a correction term, which is the difference in free-stream potential values between the trailing edge control points.

Detailed study of the flows at the trailing edge near the tip suggests a pressure Kutta condition, which requires the pressures of the last panels at the trailing edge be equal. The non-linear aspect of the pressure Kutta condition requires an iterative scheme, whereby the initial dipole strengths on the wake surface are obtained using Morino's Kutta condition, and the successive dipole strengths are adjusted based

on the error in the computed trailing edge element pressures. Hence, the three-dimensional cross flow effects on Kutta condition are included by adjusting the dipole strengths on the wake surface during the iteration process.

The compatibility condition, which requires the difference of the spanwise velocities of the upper and lower panels at the trailing edge be equal to the differentiation of the spanwise circulation, is shown to be satisfied. This indicates the self-consistency of the present method.

An accelerated iterative matrix solver is employed for the solution of the resulting linear system of equations. Computing time is reduced significantly compared to that for the Gauss elimination method.

Comparison of the results for the ellipsoid at zero angle of attack with the analytic solutions provides a verification of the present method.

Calculation for the circular wing with varying thickness is performed to illustrate the thickness effect on the performance of the wing. As the thickness is decreased, the analytic results for the zero thickness wing by Jordan [12] are recovered. This demonstrates the suitability of the present method for the analysis of a very thin wing. With the frozen wake model in the present method, the thickness effect near the tip is found to have a trend which is the reverse of the two-dimensional case, i.e., as the thickness is increased, the loading is decreased. This is due to the cross flow component around the tip, whose magnitude increases as the thickness is increased.

The effect of sweep angles on the spanwise circulation of the rectangular wing is investigated. The circulation near the tip is decreased for the forward swept wing, while the circulation in the inner part of the wing is decreased for the backward swept wing, compared to the unswept wing case. The local section lift coefficients for the 0 and 20 degree swept wings show a satisfactory agreement with those by the various production codes.

The calculated pressure distributions around the wing-body configuration are in

excellent agreement with those found by experiment in spite of the fact that neither compressibility nor viscous corrections are made.

The capability of the present method to predict internal flow properties is demonstrated by the example of a long axisymmetric duct, for which Hess's low order surface source method gives particularly inaccurate results.

For the propeller problem, a rotational symmetry is exploited so that only $\frac{1}{K}$ fraction of the geometry, i.e., one blade and the inter-blade segment of the hub, is discretized. By summing the influence functions for the symmetric panels by rotating an angle $\frac{2\pi}{K}$, the same panelling on all blades is achieved. Substantial coding complication needed for different panelling on the other blades is thus avoided.

A special far-wake approximation is employed for the calculation of the influence function of the ultimate wake. The semi-infinite helical dipole strip representing the ultimate wake is replaced by a source disk at the beginning of the ultimate wake. The computational axial distance in the upstream hub is reduced without loss of accuracy by replacing the semi-infinite upstream hub by a dipole disk.

A reliable pressure distribution around a marine propeller, especially near the leading edge of the blade, is obtained. At the design inflow condition of the selected propeller, the chordwise loading distribution is shown to have an $a=0.8$ loading shape. The effect of the hub is naturally included by distributing panels on the surface of the hub.

The viscous effects are included by including a tangential friction force on each panel with the two-dimensional section drag coefficient. The thrust and torque, calculated by the integration of the element pressure on each panel, are in close agreement with the experimental results even for the off-design conditions.

Bibliography

- [1] R.J. Boswell and M.L. Miller. *Unsteady Propeller Loading - Measurement, Correlation, with Theory and Parametric Study*. Technical Report DTNSRDC Report 2625, DTNSRDC, October 1968.
- [2] D.R. Bristow and G.G. Grose. *Modification of the Douglas Neumann Program to Improve the Efficiency of Predicting Component Interference and High Lift Characteristics*. Technical Report NASA CR-3020, Langley Research Center, NASA, 1978.
- [3] R.L. Carmichael and L.L. Erickson. PAN AIR - a higher order panel method for predicting subsonic and supersonic linear potential flows about arbitrary configurations. *AIAA Paper*, 81-0252, 1981.
- [4] R.W. Clark. A new iterative matrix solution procedure for three-dimensional panel methods. In *29rd Aerospace Sciences Meeting*, AIAA, Reno, Nevada, January 1985.
- [5] D.S. Greeley and J.E. Kerwin. Numerical methods for propeller design and analysis in steady flow. *Trans. SNAME*, 90, 1982.
- [6] J.L. Hess. *Calculation of Potential flow About Arbitrary Three-Dimensional Lifting Bodies*. Technical Report MDC J5679-01, McDonnell Douglas, October 1972.

- [7] J.L. Hess and D.L. Friedman. *An Improved Higher Order Panel Method for Three-Dimensional Lifting Potential Flow*. Technical Report 79277-60, NADC, December 1981.
- [8] J.L. Hess and A.M.O. Smith. Calculation of nonlifting potential flow about arbitrary three dimensional bodies. *Journal of Ship Research*, 8(2), September 1964.
- [9] J.L. Hess and Walter O. Valarezo. Calculation of steady flow about propellers by means of a surface panel method. In *29rd Aerospace Sciences Meeting*, AIAA, Reno, Nevada, January 1985.
- [10] J.L. Hess. Comment on application of computational aerodynamics to airplane design. *Journal of Aircraft*, 22(4):351-352, April 1985.
- [11] E. H. Hirschel and L. Fornasier. Flowfield and vorticity distribution near wing trailing edges. *AIAA Paper*, 84-421, 1984.
- [12] Peter F. Jordan. Exact solutions for lifting surfaces. *AIAA Journal*, 11(8), August 1973.
- [13] J.E. Kerwin, Spyros A. Kinnas, Jin-Tae Lee, and Wei-Zen Shih. A surface panel method for the analysis of ducted propellers. *Trans. SNAME*, 95, 1987.
- [14] J.E. Kerwin and C.-S. Lee. Prediction of steady and unsteady marine propeller performance by numerical lifting-surface theory. *Trans. SNAME*, 86, 1978.
- [15] K. Koyama, A. Kakugawa, and M. Okamoto. Experimental investigation of flow around a marine propeller and application of panel method to the propeller theory. In *Sixteenth Symposium on Naval Hydrodynamics*, 1986.
- [16] Sir Horace Lamb. *Hydrodynamics*. Cambridge University Press, sixth edition, 1932.

- [17] J. Margason, S.O. Kjelgaard, W.L. Sellers, C.E.K. Morris, K.B. Walkey, and E.W. Shields. Subsonic panel methods – a comparison of several production codes. In *AIAA 23rd Aerospace Sciences Meeting*, Reno, Nevada, January 1985.
- [18] K.S. Min. *Numerical and Experimental Methods for the Prediction of Field Point Velocities around Propeller Blades*. Technical Report 78-12, M.I.T., Department of Ocean Engineering, June 1978.
- [19] L.R. Miranda. Application of computational aerodynamics to airplane design. *Journal of Aircraft*, 21:355–370, June 1984.
- [20] Luigi Morino and Ching-Chiang Kuo. Subsonic potential aerodynamic for complex configurations: a general theory. *AIAA J.*, 12(2):191–197, February 1974.
- [21] J.N. Newman. Distributions of sources and normal dipoles over a quadrilateral panel. *Journal of Engineering Mathematics*, 20:113–126, 1986.
- [22] D.A. Treadgold, A.F. Jones, and K.H. Wilson. *Pressure Distribution Measured in the RAE 8ft * 6 ft Transonic Wind Tunnel on RAE 'A' in Combination with an Axisymmetric Body at Mach Numbers of 0.4, 0.8 and 0.9*. Technical Report AR-138, AGARD, 1979.
- [23] Mo-Hwa Wang. *Hub Effects in Propeller Design and Analysis*. PhD thesis, M.I.T., Department of Ocean Engineering, May 1985.
- [24] H.H. Youngren, E.E. Bouchard, R.M. Coopersmith, and L.R. Miranda. Comparison of panel method formulations and its influence on the development of QUADPAN, an advanced low order method. In *AIAA Applied Aerodynamics Conference*, Danvers, Mass., July 1983.

Appendix A

Numerical formulation of the various panel methods for two-dimensional problems

To compare the characteristics of the various methods described in Chapter 2, each method is implemented as numerical code for the analysis of the two-dimensional flow around a hydrofoil. Since the Hess's source based method is widely used and its characteristics are relatively well known, four other methods are actually implemented.

A.1 Perturbation potential method

Two-dimensional form of Equation 2.9, for the field point p on the body surface, is

$$\begin{aligned} -\pi \phi(p) = & \int_{S_B} \left[\phi(q) \frac{\partial}{\partial n_q} \log R(p; q) - \frac{\partial \phi}{\partial n_q} \log R(p; q) \right] ds \\ & + \int_{S_W} \Delta \phi(q) \frac{\partial}{\partial n_q} \log R(p; q) ds. \end{aligned} \quad (\text{A.1})$$

Here the three-dimensional Green function, $-\frac{1}{4\pi} \frac{1}{R}$, is replaced by two-dimensional one, $\frac{1}{2\pi} \log R$, and the surface integral is replaced by a line integral along the body and wake surfaces.

The body geometry is replaced by an N-faced inscribed polygon, where N is the number of panels, as shown in Figure A.1. A logical choice for the panel arrangement is a *cosine* spacing, where mean line ordinate and thickness is first evaluated at the following points along the nose-tail line,

$$x_j = \frac{c}{2} \left(1 - \cos\left(\frac{2\pi(j-1)}{N}\right) \right), \quad j = 1, 2, \dots, N/2 + 1. \quad (\text{A.2})$$

The panel boundaries are then obtained by adding and subtracting the half thickness of the section at right angles to the mean line. This concentrates the elements at the leading and trailing edges, where greater resolution is required. The nodes are numbered in clockwise order, starting at the lower trailing edge, and j-th panel is one between nodes j and j+1.

Singularity strength distribution is assumed to be piecewise constant over the panels. The collocation point, where the discretized integral equation is satisfied, is selected as the midpoint of each panel. Then the discretized form of Equation A.1 is

$$\sum_{j=1}^N D_{ij} \phi_j + W_i (\Delta\phi)_{wake} = \sum_{j=1}^N S_{ij} \left(\frac{\partial\phi}{\partial n} \right)_j, \quad i = 1, 2, \dots, N, \quad (\text{A.3})$$

where

$$\begin{aligned} D_{ij} &= \int_{C_j} \frac{\partial}{\partial n_q} \log R(p_i, q) ds, \\ S_{ij} &= \int_{C_j} \log R(p_i, q) ds, \\ W_i &= \int_{S_w} \frac{\partial}{\partial n_q} \log R(p_i, q) ds. \end{aligned}$$

A numerical Kutta condition can be stated as the potential jump in the wake should be equal to the difference of total potential values, as explained in Chapter 3.

$$(\Delta\phi)_{wake} = \Phi^u - \Phi^l = \phi_N - \phi_1 + U_\infty \left(\cos \alpha (x_N - x_1) + \sin \alpha (y_N - y_1) \right), \quad (\text{A.4})$$

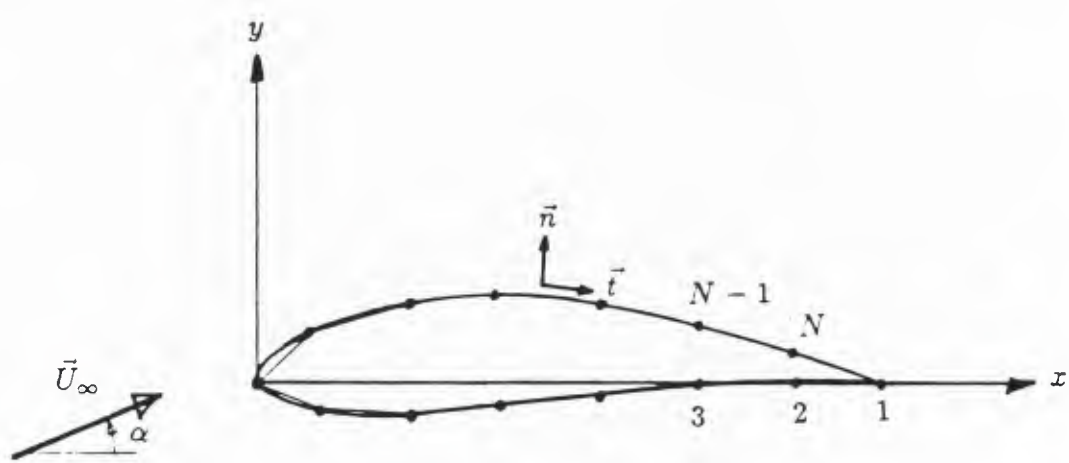


Figure A.1: Nomenclature of the potential methods for a two-dimensional foil

where $U_\infty \left(\cos \alpha(x_N - x_1) + \sin \alpha(y_N - y_1) \right)$ is the inflow potential difference between the control points of the two trailing edge panels.

This results in a system of linear equations for the unknown dipole strengths.

$$\sum_{j=1}^N A_{ij} \phi_j = \sum_{j=1}^N B_{ij} \left(\frac{\partial \phi}{\partial n} \right)_j - U_\infty \left(\cos \alpha(x_N - x_1) - \sin \alpha(y_N - y_1) \right), \quad i = 1, 2, \dots, N, \quad (\text{A.5})$$

where $A_{ij} = \pi$,if $i = j$,

$= D_{ij}$,if $i \neq j$,

and $A_{ij} = A_{ij} - W_i$,if $i = 1$,

$= A_{ij} + W_i$,if $i = N$.

Solution of Equation A.5 yields the values of potential on the panels, under the assumption that the potential is constant on each panel. Surface velocity is obtained by numerical differentiation of the potential. A quadratic polynomial to the values of potential at three panel midpoints is assumed, and the velocity at the panel midpoint is obtained by differentiating it with respect to the coordinate that is tangent to the panel. The arc-length between two control points is approximated as the sum of half panel lengths of the panels.

Once the velocity is known, the pressure is calculated from Bernoulli's equation, where the pressure coefficient is defined as

$$C_p = \frac{p - p_\infty}{\frac{1}{2} \rho U_\infty^2}.$$

Forces and moments are then obtained by summing the element forces and moments. An alternative lift coefficient, which is based on Kutta-Joukowsky's law, is calculated by

$$C_L = \frac{L}{\frac{1}{2} \rho U_\infty^2 c} = 2 \frac{(\Delta \phi)_{wake}}{U_\infty c},$$

and the drag coefficient should be zero.

A.2 Total potential method

Two-dimensional form of Equation 2.12, for the field point p on the body surface, is

$$\begin{aligned} -\pi \Phi(p) = & -2\pi \phi_\infty + \int_{S_B} \Phi(q) \frac{\partial}{\partial n_q} \log R(p; q) ds \\ & + \int_{S_W} \Delta \Phi(q) \frac{\partial}{\partial n_q} \log R(p; q) ds, \end{aligned} \quad (\text{A.6})$$

where $\phi_\infty = \vec{U}_\infty \cdot \vec{r} = U_\infty(x \cos \alpha + y \sin \alpha)$ for uniform inflow velocity with angle of attack α .

Discretizations of geometry and singularity strengths are identical to those for the perturbation potential method. Then the discretized form of Equation A.6 is

$$\sum_{j=1}^N D_{ij} \Phi_j + W_i (\Delta \Phi)_{wake} = 2U_\infty(x_i \cos \alpha + y_i \sin \alpha), \quad i = 1, 2, \dots, N. \quad (\text{A.7})$$

A Kutta condition can be stated as the potential jump in the wake should be equal to the difference of the total potential values.

$$(\Delta \Phi)_{wake} = \Phi_N - \Phi_1. \quad (\text{A.8})$$

This results in a system of linear equations for unknown dipole strengths.

$$\sum_{j=1}^N A_{ij} \Phi_j = 2U_\infty(x_i \cos \alpha + y_i \sin \alpha), \quad (\text{A.9})$$

$$\begin{aligned} \text{where } A_{ij} &= \pi & \text{if } i = j, \\ &= D_{ij} & \text{if } i \neq j, \end{aligned}$$

$$\begin{aligned} \text{and } A_{ij} &= A_{ij} - W_i & \text{if } i = 1, \\ &= A_{ij} + W_i & \text{if } i = N. \end{aligned}$$

Here left hand side of the matrix equation is identical to that of the perturbation potential method.

Calculation of the surface velocity follows the same scheme of the perturbation method, except that total velocity is calculated directly without summing the inflow velocity. The pressure and forces are calculated by the same scheme of the perturbation method.

A.3 Mixed source and vortex method

Two-dimensional form of Equation 2.15, for the field point p on the body surface, is

$$\begin{aligned} \pi \frac{\partial \phi}{\partial n_p} = & \int_{S_B} \frac{\partial \phi}{\partial n_q} \frac{\partial}{\partial n_p} \log R(p; q) ds - \int_{S_B} \phi \frac{\partial^2}{\partial n_p \partial n_q} \log R(p; q) ds - \\ & \int_{S_W} \Delta \phi \frac{\partial^2}{\partial n_p \partial n_q} \log R(p; q) ds. \end{aligned} \quad (\text{A.10})$$

An equivalent form from Equation 2.16 is

$$\pi \frac{\partial \phi}{\partial n_p} = \int_{S_B} \sigma(q) \frac{\partial}{\partial n_p} \log R(p; q) ds + \int_{S_B} \gamma(q) \frac{\partial}{\partial n_p} [-\Theta(p; q)] ds, \quad (\text{A.11})$$

where $\Theta(p; q) = \arctan(\frac{y-q}{x-\xi})$ is the two-dimensional vortex potential, $\sigma = \frac{\partial \phi}{\partial n}$, $\gamma = \frac{\partial \phi}{\partial t}$, and t is defined to be tangential to the body surface. Sign of the vorticity is defined to be positive for clockwise induced flow.

Equation A.11 can also be derived directly from Equation A.10 using the Cauchy-Riemann relations for the complex potential of $\log R + i\Theta$,

$$\begin{aligned} \frac{\partial}{\partial t} \log R &= \frac{\partial}{\partial n} \Theta, \\ \frac{\partial}{\partial n} \log R &= -\frac{\partial}{\partial t} \Theta. \end{aligned}$$

Since a normal dipole panel of constant strength is equivalent to a pair of point vortices at the panel edges, point vortices are distributed instead of the piecewise constant dipoles. Point sources are also distributed on the same locations of the vortices.

Locations of the singularities are determined by first evaluating mean line ordinates and thickness at the following points along the nose-tail line,

$$x_j^c = \frac{c}{2} \left(1 - \cos\left(\frac{\pi(2j-1)}{N}\right) \right), j = 1, 2, \dots, N/2,$$

then adding and subtracting the half thickness. Locations of control points are determined similarly, but x-coordinates of the points are

$$x_i^p = \frac{c}{2} \left(1 - \cos\left(\frac{2\pi(i-1)}{N}\right) \right), i = 1, 2, \dots, N/2 + 1.$$

In this way the control points are located on the exact foil surface instead of the panel midpoints which are chosen as the control points in the potential method.(see Figure A.2)

Since an explicit Kutta condition is needed for the velocity method, tangential velocity at the trailing edge control point is set equal to zero. Direction of the tangential velocity is defined to be normal to the bisector of the upper and lower surfaces at the trailing edge.

Discretization of Equation A.11 results in a system of linear equations for the unknown vortex strengths.

$$\sum_{j=1}^N G_{ij} \Gamma_j = \pi \left(\frac{\partial \phi}{\partial n} \right)_i - \sum_{j=1}^N S_{ij} \left(\frac{\partial \phi}{\partial n} \right)_j, \quad i = 1, 2, \dots, N, \quad (\text{A.12})$$

where G_{ij} = normal induced velocity at i-th control point

due to the j-th point vortex of unit strength,

S_{ij} = normal induced velocity at i-th control point

due to the j-th point source of unit strength.

Equation A.12 is enough to determine N unknown vortex strengths.

Surface perturbation velocity is calculated by dividing the obtained vortex strength by the arclength between the adjacent control points. The arclength is determined as an arclength of the circle which passes the vortex point and the two adjacent control

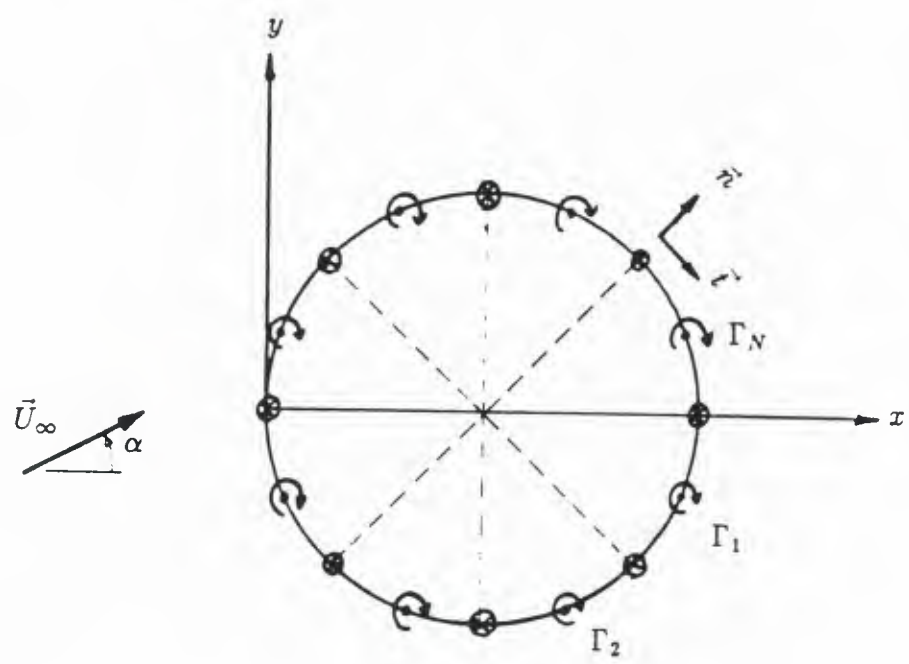


Figure A.2: Nomenclature of the velocity method for a two-dimensional foil.

points. Surface velocity is obtained by adding the inflow velocity to the calculated perturbation velocity. Calculation of the pressure follows the same scheme of the potential method.

A.4 Vortex method

Two-dimensional form of Equation 2.18, for the field point p on the body surface, is

$$2\pi \frac{\partial \phi}{\partial n_p} = \int_{S_B} \gamma(q) \frac{\partial}{\partial n_p} [-\Theta(p; q)] ds, \quad (\text{A.13})$$

where $\Theta(p; q) = \arctan(\frac{y-\eta}{x-\xi})$ is a two-dimensional vortex potential, $\gamma = \frac{\partial \Phi}{\partial t}$, and t is defined to be tangential to the body surface. Sign of the vorticity is defined to be positive for clockwise induced flow.

Discretization of the vortex method follows the same scheme of the source and vortex method. Instead of distributing both sources and vortices, only the vortices are distributed on the foil surface.

Discretization of Equation A.13 results in a system of linear equations for the unknown vortex strengths.

$$\sum_{j=1}^N G_{ij} \Gamma_j = 2\pi \left(\frac{\partial \phi}{\partial n} \right)_i, \quad i = 1, 2, \dots, N, \quad (\text{A.14})$$

where G_{ij} = normal induced velocity at i -th control point due to the j -th point vortex of unit strength.

Surface velocity at the node point is calculated by dividing the obtained vortex strength by the arclength between the adjacent control points. Calculated velocity here is the total surface velocity, hence the inflow velocity should not be added. Calculation of pressure follows the same scheme of the mixed source and vortex method.

Appendix B

Equivalence of dipole and vorticity distribution

Consider a surface S in space bounded by a closed curve C , with the unit normal vector \vec{n} . (see Figure B.1) The vector between the field point $p(x,y,z)$ and the source point $q(\xi,\eta,\varsigma)$ on S is denoted \vec{R} , and the length of this vector is denoted R .

$$\vec{R} = (x - \xi)\vec{i} + (y - \eta)\vec{j} + (z - \varsigma)\vec{k}.$$

Let the surface S be covered with a normal dipole distribution of strength μ , then there exists the following relation between the dipole and vorticity distribution.

THEOREM : The induced velocity at p due to the normal dipole distribution of strength μ on S is equal to the sum of the induced velocities due to a surface vorticity distribution on S and due to a line vortex along C . The strength of the line vortex is the local value of the dipole strength, $\Gamma = \mu$ (on C). The vorticity on S is a vector tangent to the curves of constant μ and has a magnitude equal to the surface gradient of μ on S , $\vec{\gamma} = \vec{n}_q \times \nabla_q^{2-D} \mu$. Specifically,

$$\begin{aligned} \iint_S \mu(q) \nabla_p \left[\frac{\partial}{\partial n_q} \left(\frac{-1}{R} \right) \right] ds &= \iint_S (\nabla_q^{2-D} \mu(q) \times \vec{n}_q) \times \nabla_p \left(\frac{-1}{R} \right) ds \\ &+ \oint_C \mu(q) \vec{t}_q \times \nabla_p \left(\frac{-1}{R} \right) dl, \end{aligned} \quad (B.1)$$

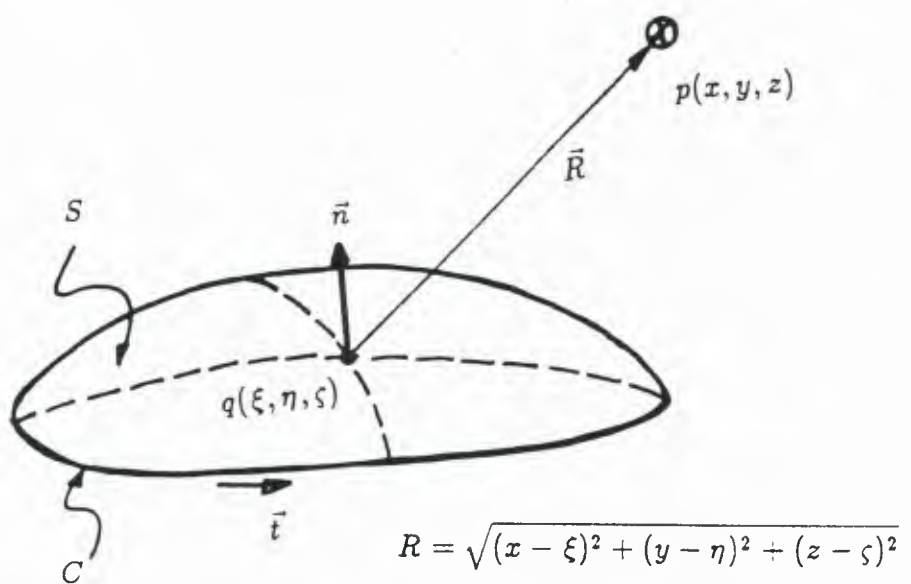


Figure B.1: Notation for a general surface.

where ∇_p is the gradient operator with respective to the point p, and ∇_q is the gradient operator with respective to the point q. PROOF : To convert the line integral in Equation B.1 into a surface integral, start with Stokes theorem,

$$\oint_C \vec{V} \cdot \vec{t} dl = \iint_S (\nabla \times \vec{V}) \cdot \vec{n} dS. \quad (B.2)$$

Put $\vec{V} = \vec{a} \times \vec{P}$, where \vec{a} is an arbitrary constant vector ($\vec{a} \neq 0$), then

$$(\vec{a} \times \vec{P}) \cdot \vec{t} = \vec{a} \cdot (\vec{P} \times \vec{t}),$$

and

$$\nabla \times (\vec{a} \times \vec{P}) \cdot \vec{n} = \vec{n} \times \nabla \cdot (\vec{a} \times \vec{P}) = -\vec{a} \cdot (\vec{n} \times \nabla) \times \vec{P}.$$

Equation B.2 becomes

$$\oint_C \vec{a} \cdot (\vec{P} \times \vec{t}) dl = - \iint_S \vec{a} \cdot (\vec{n} \times \nabla) \times \vec{P} dS.$$

Since \vec{a} is an arbitrary constant vector, the following transformation from a line integral to a surface integral is possible,

$$\oint_C \vec{t} \times \vec{P} dl = \iint_S (\vec{n} \times \nabla) \times \vec{P} dS. \quad (B.3)$$

If \vec{P} is set to be $\vec{P} = \mu(q) \nabla_p \left(\frac{-1}{R} \right)$ in Equation B.3, then

$$\oint_C \vec{t} \times \left(\mu(q) \nabla_p \left(\frac{-1}{R} \right) \right) dl = \iint_S (\vec{n}_q \times \nabla_q) \times \left(\mu(q) \nabla_p \left(\frac{-1}{R} \right) \right) dS. \quad (B.4)$$

The right hand side of Equation B.1 is transformed into a form which involves only surface integrals on S, using Equation B.4. The integrand of the resulting surface integral is

$$\begin{aligned} (\nabla_q \mu(q) \times \vec{n}_q) \times \nabla_p \left(\frac{-1}{R} \right) + (\vec{n}_q \times \nabla_q) \times \left(\mu(q) \nabla_p \left(\frac{-1}{R} \right) \right) = \\ \vec{n}_q \left(\nabla_q \mu \cdot \nabla_p \left(\frac{-1}{R} \right) \right) - \nabla_q \mu \left(\vec{n}_q \cdot \nabla_p \left(\frac{-1}{R} \right) \right) \\ + \nabla_q \left(\vec{n}_q \cdot \mu \nabla_p \left(\frac{-1}{R} \right) \right) - \vec{n}_q \left[\nabla_q \cdot \left(\mu \nabla_p \left(\frac{-1}{R} \right) \right) \right], \end{aligned} \quad (B.5)$$

where $\nabla_q \left(\underline{\vec{n}_q} \cdot \mu \nabla_p \left(\frac{-1}{R} \right) \right)$ means that ∇_q operates only on $\mu \nabla_p \left(\frac{-1}{R} \right)$, not on \vec{n}_q . The last two terms of the right hand side of Equation B.5 can be expressed as

$$\nabla_q \left(\mu \underline{\vec{n}_q} \cdot \nabla_p \left(\frac{-1}{R} \right) \right) = \nabla_q \mu \left(\vec{n}_q \cdot \nabla_p \left(\frac{-1}{R} \right) \right) + \mu \nabla_q \left(\underline{\vec{n}_q} \cdot \nabla_p \left(\frac{-1}{R} \right) \right),$$

and

$$\vec{n}_q \left[\nabla_q \cdot \left(\mu \nabla_p \left(\frac{-1}{R} \right) \right) \right] = \vec{n}_q \left[\nabla_q \mu \cdot \nabla_p \left(\frac{-1}{R} \right) \right] + \vec{n}_q \left[\mu \nabla_q \cdot \nabla_p \left(\frac{-1}{R} \right) \right],$$

where $\nabla_q \cdot \nabla_p \left(\frac{-1}{R} \right) = \nabla_q^2 \left(\frac{1}{R} \right) = 0$ for $p \notin S$. Due to the cancellations of terms, Equation B.5 becomes

$$\mu(q) \nabla_q \left(\underline{\vec{n}_q} \cdot \nabla_p \left(\frac{-1}{R} \right) \right) \quad (\text{B.6})$$

Equation B.6 can be proceeded using

$$\nabla_q \left(\underline{\vec{n}_q} \cdot \nabla_p \left(\frac{-1}{R} \right) \right) = \vec{n}_q \nabla_q \cdot \nabla_p \left(\frac{-1}{R} \right) + \vec{n}_q \times \left(\nabla_q \times \nabla_p \left(\frac{-1}{R} \right) \right), \quad (\text{B.7})$$

where the first term is zero. Thus the integrand of the resulting surface integral in the right hand side of Equation B.1 is

$$\mu(q) \vec{n}_q \times \left(\nabla_q \times \nabla_p \left(\frac{-1}{R} \right) \right) \quad (\text{B.8})$$

On the other hand, the integrand of the surface integral of the left hand side of Equation B.1 is

$$\mu(q) \nabla_p \left(\underline{\vec{n}_q} \cdot \nabla_q \left(\frac{-1}{R} \right) \right) = \mu(q) \vec{n}_q \nabla_p \cdot \nabla_q \left(\frac{-1}{R} \right) + \mu(q) \vec{n}_q \times \left(\nabla_p \times \nabla_q \left(\frac{-1}{R} \right) \right). \quad (\text{B.9})$$

We can show that Equation B.9 is equivalent to Equation B.8, using

$$\nabla_p \times \nabla_q \left(\frac{-1}{R} \right) = -\nabla_p \times \left(\frac{\vec{R}}{R^3} \right) = -\nabla_p \left(\frac{1}{R^3} \right) \times \vec{R} - \left(\frac{1}{R^3} \right) \nabla_p \times \vec{R},$$

and

$$\nabla_q \times \nabla_p \left(\frac{-1}{R} \right) = \nabla_q \times \left(\frac{\vec{R}}{R^3} \right) = \nabla_q \left(\frac{1}{R^3} \right) \times \vec{R} + \left(\frac{1}{R^3} \right) \nabla_q \times \vec{R},$$

where $-\nabla_p \left(\frac{1}{R^3} \right) = \nabla_q \left(\frac{1}{R^3} \right)$, and $-\nabla_p \times \vec{R} = \nabla_q \times \vec{R} = 0$.

Appendix C

Potential and velocities on the surface of an ellipsoid

Consider an ellipsoid with semi-lengths of its axes a , b and c in an uniform inflow velocity U_∞ parallel to x -axis. Equation of the ellipsoid is

$$\frac{x^2}{a^2} + \frac{y^2}{b^2} + \frac{z^2}{c^2} = 1. \quad (\text{C.1})$$

Expression for the perturbation potential on the ellipsoid surface is given by Lamb [16],

$$\phi(x, y, z) = U_\infty x K, \quad (\text{C.2})$$

where

$$\begin{aligned} K &= \frac{abc}{2-\alpha_o} D \\ D &= \int_0^\infty \frac{d\lambda}{(a^2+\lambda)^{3/2} (b^2+\lambda)^{1/2} (c^2+\lambda)^{1/2}} \\ \alpha_o &= abc D \end{aligned}$$

The quantity D is purely numerical and can be calculated by a numerical integration.

For brevity, set $U_\infty = 1$, $a = b = 1$, then Equation C.1 becomes

$$x^2 + y^2 + \frac{z^2}{c^2} = 1. \quad (\text{C.3})$$

U232711